Point Defects in 2D and 3D Nanomaterials: A Density Functional Theory Exploration

Cover: The charge density difference profile of a Schottky dimer defect inside a rock salt PbS crystal. Charge accumulation is indicated by the purple color with its cross section in yellow and red. Lead atoms are denoted in cyan and sulfur atoms in light ivory. This plot is generated using the VESTA[1] program.

Invitation Card: The spin density plot of a W_S antisite defect in a WS_2 monolayer, showing the magnetic moment localized at the defect site. The spin-up density is marked in cyan and spin-down density in magenta. The tungsten atoms are denoted in blue and sulfur atoms in red. This plot is generated using the VESTA[1] program.

PhD thesis, Utrecht University, the Netherlands, April 2017.
ISBN: 978-90-393-6777-3
Printed by Gildeprint.
A digital version of this thesis is available at http://www.colloid.nl

Point Defects in 2D and 3D Nanomaterials: A Density Functional Theory Exploration

---

Puntdefecten in 2D en 3D Nanomaterialen:
Een Dichtheidsfunctionaaltheoretische Verkenning
(met een samenvatting in het Nederlands)

Proefschrift

ter verkrijging van de graad van doctor aan de Universiteit Utrecht op gezag van de rector magnificus, prof. dr. G.J. van der Zwaan, ingevolge het besluit van het college voor promoties in het openbaar te verdedigen op maandag 8 mei 2017 des ochtends te 10.30 uur

door

Wun-Fan Li

geboren op 11 januari 1985 te Taoyuan City, Taiwan

Promotoren:	Prof. dr. M. Dijkstra
	Prof. dr. A. van Blaaderen
Copromotor:	Dr. ir. M.A. van Huis

Dit proefschrift werd (mede) mogelijk gemaakt met financiële steun van NWO (VIDI 723.012.006).

Contents

Chapter 1

Introduction

From introductory textbooks on solid-state physics[2], we know that unit cells are the smallest building blocks from which a crystal can be constructed. A unit cell is characterized by a set of lattice vectors $\{\boldsymbol{a}_i\}$ and contains one or a group of atoms. By periodically and infinitely repeating the unit cell in three dimensions, a *perfect* crystal will be formed. However in reality, various kinds of imperfections will always be present in crystals. These imperfections can be collectively called *defects*. Defects may exist in materials with a very dilute concentration as low as 1 part per million (ppm)[3,4]. This is the *principle of dilute concentration*[3] which states that the dilute concentration of defects makes the spacing between defect sites much larger than the spacing between atoms, therefore crystalline materials will retain their crystallinity and be prevented from forming the amorphous phase. However, as will be seen in the following paragraph, the existence of a trace amount of defects can already determine the physical and chemical properties of a material to a great extent. Therefore, it is of utmost importance to understand the properties of defects in materials. In fact, as stated by Cai and Nix; *the control of imperfections in crystalline materials lies at the heart of materials science*[3].

1.1 Examples of the impact of defects on materials

In bulk materials, defects are instrumental for the functionality of many materials that play an important role in everyday life. One example is the doping of semiconductors to tune their electronic properties, required to build transistors which are at the heart of any binary computer. Another example is microalloying in steels (doping with defect concentrations of typically 1 ppm) to tune mechanical properties such as strength and ductilty.

In nanomaterials, which we define as materials smaller than 100 nm in at least one spatial dimension, and with at least one physical property which varies with this nanoscale dimension[5], defects play an even more important role than in bulk materials. Their impacts on the nanomaterial can be vital, or fatal[6]. In semiconductor quantum dots, for example, vacancies are supposed to suppress the quantum yield for photoluminescence, as they act as recombination centers for electron-hole pairs[5]. Another example is the important cation exchange process used to create core/shell particles, and which is mediated by diffusion of point defects as was investigated in detail for the case of PbSe/CdSe heteronanocrystals (HNCs)[7,8]. Finally, even the magnetism observed in 3D and 2D nanomaterials is often attributed to (surface) defects[9,10].

All the aforementioned examples demonstrate the great potential of *defect engineering* - the design of novel physical and chemical properties of materials through control of defects for different technological applications. Defect engineering has been applied to 3D semiconductors at the nanoscale[11] and to 2D layered transition metal dichalcogenides (TMDs)[12].

1.2 Classification of defects

To have an overview of the different kinds of defects and to define the scope of this thesis, it is helpful to give a brief introduction of how defects are classified; defects in crystals can be classified by their dimensionality[3]:

Zero dimensional Defects of this kind are localized or confined to atomic dimensions in all three spatial dimensions of a crystal. Hence they are also called *point* defects.

One dimensional Defects of this kind are *line* defects, which include dislocations and disclinations.

Two dimensional This category includes free surfaces and various kinds of boundaries: grain boundary, phase boundary, stacking fault, an-

tiphase boundary*, and electric or magnetic domain boundary.

Three dimensional defects The 3D defects are more macroscopic, including porosity, cracks, and inclusions of other materials.

It is worth noting that point defects are distinct from the one, two, and three dimensional defects in two ways[13]. First, in contrast to other defects of higher dimensions, it is still difficult nowadays to directly investigate point defects using experimental instrumentation[4,14]. Often they can only be observed indirectly by their effect on the physical properties of the crystal. Second, because point defects can be placed in a crystal in a large number of possible configurations, the entropy of the system will be increased, and as a result the free energy will be minimized. Therefore point defects are more favourable than other higher-dimensional defects, and can exist in a crystal at an appreciable concentration. Depending on the source of point defects, they can be further categorized as intrinsic or extrinsic[15]:

Intrinsic (native) The intrinsic defects involve only atoms of the host materials.

1. *Vacancy* - atoms of the host crystal are missing at the lattice sites (Ex.: Pb vacancy, V_{Pb}, in PbS)
2. *Interstitial* - atoms of the host crystal are present at interstitial sites (Ex.: S interstitial, I_S, in PbS)
3. *Frenkel defects* - a neutral pair of vacancy and interstitial defects of the same atomic species (Ex.: V_{Pb} + I_{Pb} in PbS)
4. *Schottky defects* - a neutral pair of cation and anion vacancies (Ex.: V_{Pb} + V_S in PbS)
5. *Antisites* - atom of one species occupies the sublattice site of other species. (Ex.: one W atom occupying one lattice site of S atoms (W_S) in a 2D WS_2 nanosheet)

Extrinsic (substitutional) The extrinsic defects involve foreign atoms such as dopants or impurity atoms.

In addition to this category, point defects can be even further classified according to their charge states. However, the focus of this thesis is on the neutral and intrinsic point defects, and to study their properties in various kinds of 3D and 2D nanomaterials.

*A domain in a crystal where the atomic species are arranged in the lattice with an occupation opposite to that in the perfect lattice. An antiphase can be regarded as being composed of antisite point defects.

1.3 Density functional theory as a tool for defect study

As mentioned earlier, because point defects are difficult to observe directly by experimental methods, their characterization by means of theoretical modelling appears to be invaluable. In this context, Density Functional Theory (DFT) is a powerful theoretical tool to model the physical properties of materials. DFT has been widely used in a variety of fields in materials science, including the study of point defects in nanomaterials. Besides the great success in materials modelling, the research on the development of DFT itself is also very active. On the theoretical part, people are endeavoring to overcome challenges such as the correction to the artificial electrostatic interaction between defect sites, the capability to handle larger supercells to reach the dilute limit of defect concentration, and even an accurate prediction of the Fermi level as the reference energy of the electron reservoir for charged detects in insulators and semiconductors to provide a faithful defect formation energy[4,14,16,17].

1.4 The nanomaterials considered in this thesis

In this thesis, three different categories of nanomaterials were selected for the point defect study. They are the 3D lead chalcogenides (PbX, X=S, Se, Te), 2D tungsten disulfide (WS_2), and 2D transition metal oxides (TMOs, TM=Sc, Ti, V, Cr, Mn), respectively.

First, the PbX systems were selected as the starting point of this exploration on defects in nanomaterials. The perfect PbX systems are a representative of classical IV-VI semiconductors with a direct and narrow band gap. They crystallize in the rock salt (*rs*) structure and have an ionic bonding network. The PbX systems have been intensively studied both experimentally and theoretically in the last decades due to their outstanding optical, electronic, and thermal electric properties. Furthermore, the PbX systems have been used to synthesize heterogeneous nanocrystals (HNCs) together with other metal chalcogenide families such as CdX[18–20] . The as-synthesized HNCs possess tunable physical properties which are desirable for novel applications. One good example is the preparation of quantum dots (QDs). Experimentally, it has been hypothesized that QDs are synthesized via the cation exchange (CE) process[5,7,19,21–26], where an exchange of the cations from two different metal chalcogenides takes place at the interface. It has also been proposed that the CE process was triggered by cation vacancies[7,19]. However, no direct experimental observation can be carried out to witness the proposed pivoting role that cation vacancies play during

the CE process. Therefore, a clearer understanding of the CE mechanism and the role that point defects play therein were the initial motivation of this project. A set of point defects were then selected for the DFT calculations. The project was soon extended from the energetics of these point defects to their structural and electronic properties, forming a panoramic database study on the behavior of point defects in PbX. Besides the CE process, this is of importance to accommodation of off-stoichiometry, and the photoluminescence of PbX systems.

The second material being studied are the 2D monolayered (ML) (WS_2) slabs. WS_2 is a member of the transition metal dichalcogenides (TMDs, or MX_2, where M=W, Mo; X=S, Se, Te) which belongs to the layered 2D van der Waals (vdW) materials. In the 2D vdW materials, atoms are bound by the intra-layer chemical bonding and the inter-layer vdW force. Theoretically, the most stable structure of TMDs consists of one layer of transition metal atoms sandwiched by two layers of chalcogen atoms with a prismatic coordination, forming the so-called 1H form[27]. Due to the weak inter-layer vdW interaction, TMDs can be exfoliated from bulk into the few-layer or ML forms. When reducing the number of layers from bulk to ML, the band gap of TMDs evolves from an indirect band gap to a direct band gap with an increased gap size due to quantum confinement[28,29]. The layer-dependent tunability of the electronic structure together with other distinct physical properties of ML TMDs make them promising candidates of applications in fields like electronics, optoelectronics, spintronics and valleytronics, sensing, and catalysis[30–33]. One of the many intriguing physical properties of ML TMDs is the significant spin-orbit coupling (SOC) effect due to the presence of the heavy transition metal atoms and the lack of space inversion symmetry. The main result of the SOC effect is the splitting of the energy bands of the *d* electrons. This SO splitting can be as large as 433 meV for pristine ML WS_2. The SOC effect is important for spintronics applications as the spin-up and spin-down electrons are now energetically separated and therefore the spin degree of freedom can be utilized for signaling. However, despite the fact that various point defects are also present in appreciable concentrations in ML TMDs, previously the study of the SOC effect has only been focused on defect-free ML TMD slabs. Therefore, we were motivated to study the SO splitting of the defect states introduced in to the band structure by energetically favourable point defects. The WS_2 system was selected instead of MoS_2 because the W atom is heavier than the Mo atom, hence a more significant SO splitting can be investigated.

The last group of materials included in this thesis are the 2D ML TMOs. For more than half a century, bulk TMOs have been the focus of extensive research due to the strongly correlated *d* electrons of the transition met-

als (TMs). These *d* electrons endow many bizarre physical properties to TMOs, among which the famous metal-insulator transition (MIT) taking place at a certain critical temperature. Furthermore, because the *d* shell of the transition metals can accommodate different amounts of electrons, the TMs can exist in multiple valence states and thus can be coordinated with different number of oxygen atoms, resulting in TMOs with various stoichiometries (for instance, vanadium oxides can exist at more than ten stoichiometries[34,35]). Another fascinating property of TMOs is the polymorphism: a certain TMO at certain stoichiometry can exist in different structures. One of the many examples is that MnO_2 can exist in six different structures[36]. The transition between these phases is also a topic of fundamental importance.

In contrast to bulk TMOs, the discovery of 2D TMOs is still at its infancy. Considering the booming progress of research being made on 2D materials after the successful synthesis of graphene, and the many novel physics being explored on various kinds of 2D materials, it is truly desirable to explore the possible 2D TMO phases. Therefore, a systematic study was performed on atomically-thin ML TMOs in four different phases. Their structural stability, electronic and magnetic properties were discussed in detail. Furthermore, the transition metal monovacancies (V_{TM}'s) in selected 2D TMO structures was also investigated as V_{TM}'s are expected to have a strong impact on the overall magnetic property of the host TMO slab. This final project is very interesting for the design of novel 2D nanomaterials for future applications.

In summary, this thesis includes the study of the structural, energetic, electronic and magnetic properties of relevant point defects in three different categories of nanomaterials – the 3D PbX systems, the 2D ML WS_2 slabs, and the 2D ML TMOs. Effort has been made to explore diverse and important topics related to point defects in each project by using DFT as the primary tool of investigation. It is worth mentioning that the calculations done in this thesis also demonstrate the capabilities and limitations of DFT and of the more advanced hybrid functional methods for materials science research.

1.5 Overview of this thesis

In Chapter 2, the theoretical foundation as well as the practical aspects of DFT will be discussed. Chapter 3 starts with the DFT exploration of point defects in PbX. The impact on photoluminescence, cation exchange, and off-stoichiometry of various kinds of point defects in PbX will be addressed. Chapter 4 discusses the SO splitting of defect states and the magnetism of point defects in ML WS_2. Finally, in Chapter 5, the study con-

tinues with the hitherto unknown atomically-thin 2D structures of TMOs. The structural, energetic, electronic, and magnetic properties of these 2D TMOs as well as transition metal monovacancies in the most stable 2D phases were examined. The main findings of this PhD study are summarized in Summary.

Chapter 2

Methods

Nano-sized materials often behave in a completely different way and possess novel physical properties in comparison to their bulk counterparts due to the quantum confinement effect. Meanwhile, point defects are omnipresent both in bulk crystals and in nanocrystals as a result of entropy, and play a crucial role in determining the chemical and physical properties of the host material. The defect effects can be either vital or fatal[6] depending on the purpose of a particular material. For instance, the sulfur monovacancy V_S will lower the carrier mobility of a MoS_2 monolayer[9,37,38] and is therefore unwanted; whereas vacancy-mediated doping of other transition metal can tune the magnetism of MoS_2, making it a magnetic semiconductor[39]. Therefore, it is highly desirable to study the behavior of point defects so that a better control over material properties can be obtained for technological applications. Parallel to the continuously growing knowledge of nanomaterials, the electronic structure theory based on quantum mechanics has also swiftly developed for more than fifty years. In particular, the rising up of the electronic density functional theory (DFT) in the mid 60's of last century has realized and popularized the theoretical study in materials science by virtue of its efficiency and accuracy to give reliable results which can help explain experimentally found phenomena, or predict new possibilities and guide directions for experiments.

Under the light of the aforementioned background, the DFT-based *ab initio* methods have been applied in this thesis to (1) investigate point defects in 2D and 3D nanocrystals, and (2) discover new monolayered (ML) 2D polymorphs of transition metal oxides.

As an introduction, the theoretical foundation as well as the practical implementation of DFT for solid-state calculations will first be addressed, followed by the basics of point defect calculations inside crystals.

2.1 Density functional theory

The intrinsic idea of DFT is to use the electron density, instead of the electronic wave function, as the only variable to calculate the energy of a many-body system. In other words, the energy can be expressed as a function of the electron density: $E = E(n)$. However, because the electron density n is also a function of the electron coordinates $\boldsymbol{r}$: $n = n(\boldsymbol{r})$, the energy is in turn a *functional* of the electron density: $E = E[n(\boldsymbol{r})]$. A functional is a function of another function, and the square brackets are introduced here to denote the functionals. The potential advantage of DFT over the most accurate wave function-based methods is that it requires only the electron density as the variable. For an N-electron system, this greatly reduces the number of degrees of freedom from $3N$ to 3 (the x, y, z spatial coordinates of the electron density).

The most rudimentary model and the precursor of modern DFT should be traced back to 1927 with two independent works done by Thomas[40] and Fermi[41]. This is the well-known Thomas-Fermi model, where the concept of using the electron density as the variable to find the total energy of a many-body system was first introduced. However, the model gave severe errors in practical calculations as it treats the electrons as non-interacting particles, neglecting the electron exchange and correlation, and takes the classical expression for the kinetic energy of the electrons. The establishment of the modern DFT started from two seminal papers published by Hohenberg and Kohn in 1964[42] which laid the theoretical foundation of DFT, and the other one published in 1965 by Kohn and Sham, introducing the Kohn-Sham Ansatz which validated DFT for real computational implementations[43]. Figures 2.1 and 2.2 show that DFT has a fast-growing and far-reaching impact in natural science - the number of DFT-related publications grows almost logarithmically per decade (Fig. 2.1), and it is applied in a wide range of scientific areas (Fig. 2.2). Even more, the Nobel Prize in chemistry in 1998 was given for computational chemistry, and half of the Prize was shared by Walter Kohn *"for his development of the density-functional theory"*[44]. The popularity of DFT is to a large extent owing to the usage of the single particle (non-interacting) Kohn-Sham equations[45], and the development of the hybrid functionals in the 1990s which largely refined the DFT accuracy to meet the *chemical accuracy* (which is 1 kcal/mol = 0.04336 eV/particle), such that DFT has been widely accepted in the computational chemistry community[45]. Nowadays, DFT is used as a standard and reliable theoretical tool to model materials properties[46].

The first part of the following text will present a concise picture of the theory part of DFT, together with its deficiencies and improvements related to this thesis. The second half of the this section will then focus on

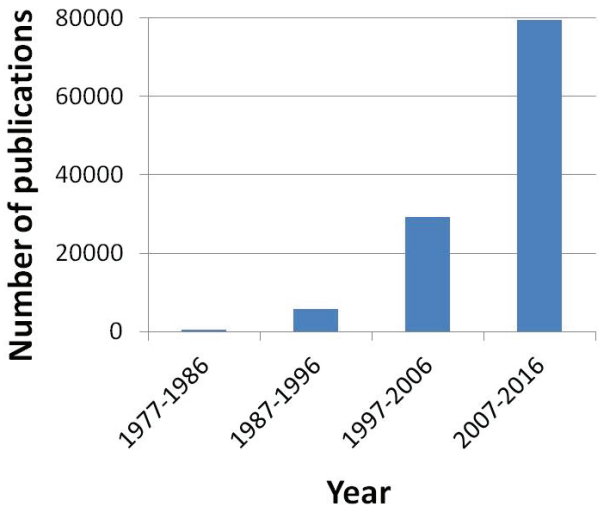

Figure 2.1: Number of DFT publications per decade. Data retrieved from Web of Science of Thomson Reuters.

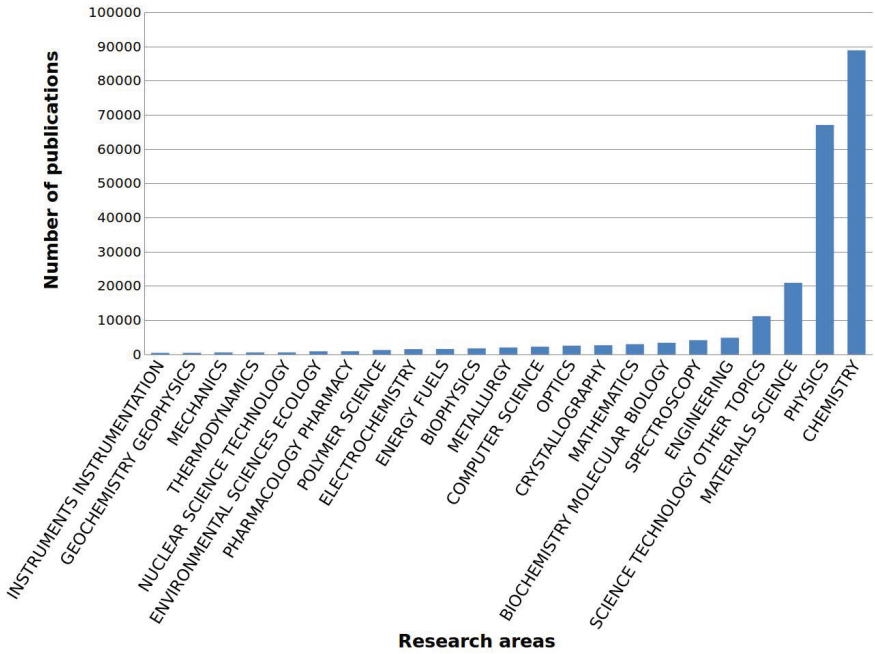

Figure 2.2: Top 25 research areas in which DFT is applied and the corresponding number of DFT publications. Data retrieved from Web of Science of Thomson Reuters.

DFT calculations for periodic systems.

2.1.1 The Hohenberg-Kohn theorems

The Schrödinger equation is the foundation of any electronic structure theory including DFT. The time-independent, non-relativistic Schrödinger equation of a any system containing a set of electrons and fixed nuclei in an external potential $V_{ext}(\boldsymbol{r})$ can be written in atomic units as

$$\hat{H}\Psi = E\Psi, \tag{2.1}$$

where the hamiltonian $\hat{H}$ reads

$$\hat{H} = -\frac{1}{2}\sum_i \nabla_i^2 + V_{ext}(\boldsymbol{r}) - \sum_{i\neq j} \frac{1}{|\boldsymbol{r_i} - \boldsymbol{r_j}|}. \tag{2.2}$$

Here the Born-Oppenheimer approximation has been made. That is, the atoms can be regarded as fixed with respect to the moving electrons, therefore the electronic part of the wave function can be decoupled from the nucleus part. The external potential V_{ext} (often also called the effective potential V_{eff}) can be any kind of potential applied on the electrons, but it stands specifically for the nuclei-electron interaction if no other fields are present;

$$V_{ext} = \sum_i \sum_I \frac{Z_I}{|\boldsymbol{r_i} - \boldsymbol{R_I}|}. \tag{2.3}$$

The first of the Hohenberg-Kohn (HK) theorem was described in the classic paper published in 1964[42], with the following statement:

Theorem 1 *The external potential $V_{ext}(\boldsymbol{r})$ exerted on a many-body system is uniquely determined by the ground state electron density $n_0(\boldsymbol{r})$ of that system.*

This means that the external potential is a functional of the electronic density: $V_{ext}(\boldsymbol{r}) = V_{ext}[n(\boldsymbol{r})]$. Once $V_{ext}(\boldsymbol{r})$ is determined, the whole Hamiltonian can be constructed by Eq. 2.2 , hence all the physical properties can be derived by solving the Schrödinger equation. Therefore Theorem 1 leads to the conclusion that *all* physical observables can be determined by the ground state electron density.

Theorem 2 *For any given external potential $V_{ext}(\boldsymbol{r})$, there exists a universal functional $E_{HK}[n]$ for energy in terms of electron density n. The global minimum of this functional is the ground state energy E_0, and the density which minimizes the functional is the ground state electron density $n_0(\boldsymbol{r})$.*

The second theorem is actually the density functional version of the variational principle, which states that

$$E[n] \geq E_0[n_0]. \tag{2.4}$$

The total energy under the HK theorem can be written as

$$E_{HK}[n] = T[n] + E_{ee}[n] + E_{ext}[n] + E_{II} \tag{2.5}$$

Here T represents the kinetic energy of the interacting electrons and E_{ee} the electron-electron interaction. $E_{ext} = \int d^3r V_{ext}(\boldsymbol{r})n(\boldsymbol{r})$ is the interaction between the external potential and the electrons, which could be the potential from the nuclei (E_{Ie}), or an external field such as an electric field or a magnetic field. E_{II} is the interaction between the nuclei. All these individual terms are functionals of the electron density. From Eq. 2.5 one could know that $E_{ext}[n]$ and E_{II} already have an explicit form, therefore we can define a universal functional G, where

$$G[n] = T[n] + E_{ee}[n] \tag{2.6}$$

is the collection of the kinetic and potential energies of the interacting electron system, and the mission of finding the expression for $E_{HK}[n]$ is reduced to searching for the expression of $G[n]$.

The HK theorem indicates that the electron density $n(\boldsymbol{r})$ can be used to construct a universal functional for energy. By minimizing this functional via the variational principle, both the ground state energy and ground state electron density can be found, and thereby all the physical properties of the system can be determined. However, the HK theorem by itself does not provide a way for actual calculations. Thus in 1965, Kohn and Sham proposed the ingenious Kohn-Sham (KS) Ansatz[43] which will be discussed in the next subsection.

2.1.2 The Kohn-Sham Ansatz

Ansatz is a German word meaning approach; the KS Ansatz is an *auxiliary* system of non-interacting particles which is chosen to have the same ground state density of the original system of interacting particles, and incorporates all the difficult many-body terms into an exchange-correlation functional of the density[47]. Although the concept of orbitals (wave function) is counter intuitively re-introduced in this density-based theory, this KS scheme simplifies the many-body problem into a set of single-particle Schrödinger equation, which can be exactly solved by numerical methods. The auxiliary system is a system of N^σnon-interacting electrons occupying a set of single-particle orbitals $\{\psi_i^\sigma(\boldsymbol{r})\}$, with σ indicating spin-up and

spin-down of the electrons, and the density is

$$n[\boldsymbol{r}] = \sum_{\sigma} \sum_{i=1}^{N^{\sigma}} \left|\psi_i^{\sigma}(\boldsymbol{r})\right|^2. \tag{2.7}$$

Kohn and Sham further re-classified the terms in Eq. 2.5 as following:

$$E_{KS}[n] = T_s[n] + E_{Hartree}[n] + E_{xc}[n] + E_{ext}[n] + E_{II}. \tag{2.8}$$

Here $T_s[n]$ is the kinetic energy of the non-interacting electrons given by

$$T_s = -\frac{1}{2} \sum_{\sigma} \sum_{i=1}^{N^{\sigma}} \left|\nabla\psi_i^{\sigma}(\boldsymbol{r})\right|^2. \tag{2.9}$$

$E_{Hartree}[n]$ is the classical Coulomb energy of the electron density interacting with itself:

$$E_{Hartree}[n] = \frac{1}{2} \int d^3\boldsymbol{r} d^3\boldsymbol{r}' \frac{n(\boldsymbol{r})n(\boldsymbol{r}')}{|\boldsymbol{r} - \boldsymbol{r}'|}. \tag{2.10}$$

Please note that $E_{Hartree}$ is a spurious self-interaction term which is exactly cancelled by the exchange energy in the framework of the Hartree-Fock (HF) theory, but only partially canceled by the exchange-correlation functional E_{xc} in DFT. All the non-classical many-body effects are implicitly absorbed in the collective term, the exchange-correlation functional E_{xc}. By equalizing Eq.2.5 and Eq.2.8, we can find the definition of E_{xc}:

$$E_{xc}[n] = (T[n] - T_s[n]) + (E_{ee} - E_{Hartree}). \tag{2.11}$$

One can find from Eq. 2.11 that $E_{ex}[n]$ is nothing else than the difference of (1) the kinetic energy and (2) the electron-electron interaction energy of the real system of interacting electrons from the non-interacting system where the electron-electron interaction is merely the Hartree energy.

Now, our goal is to find the ground state energy and the ground state electron density of the non-interacting system, and this can be done by minimizing E_{KS} with respect to the single-particle orbital $\psi_i(\boldsymbol{r})$. This minimization is a constrained optimization, where the constraint is that the the integral of the density over space should be equal to the total number of particles N. Therefore the Lagrange multiplier approach should be applied, and the result is a set of KS equations:

$$\hat{H}_{KS}\psi_i(\boldsymbol{r}) = \epsilon\psi_i(\boldsymbol{r}), \text{ with} \tag{2.12a}$$

$$\hat{H}_{KS} = -\frac{1}{2}\nabla^2 + V_{KS}(\boldsymbol{r}), \text{ and} \tag{2.12b}$$

$$\begin{aligned} V_{KS}(\boldsymbol{r}) &= V_{ext}(\boldsymbol{r}) + \frac{\delta E_{Hartree}}{\delta n(r)} + \frac{\delta E_{XC}}{\delta n(\boldsymbol{r})} \\ &= V_{ext}(\boldsymbol{r}) + V_{Hartree}(\boldsymbol{r}) + V_{XC}(\boldsymbol{r}). \end{aligned} \tag{2.12c}$$

Because now the Hamiltonian $\hat{H}_{KS}$ is dependent on the orbital $\psi_i(\boldsymbol{r})$ and on the density $n(\boldsymbol{r})$ via Eq. 2.7, the KS equations should be solved in a self-consistent manner.

2.1.3 Exchange-correlation functionals

It is obviously seen in Eq. 2.12 that the exchange-correlation functional E_{XC} is the only unknown term in the hamiltonian, and the KS scheme unfortunately cannot provide a specific expression for E_{XC}. The pursuit of a good formulation of E_{XC} thus becomes the major part of the development of the method. In addition, it is worth noting that DFT by itself is an exact theory, that is, no approximation has been made. However, when it comes to practical calculations, approximations are made for the E_{XC} term.

Local density approximation (LDA)

The advantage of the rearranged energy expression in Eq. 2.8 is that by separating out the independent-particle kinetic energy and the long-ranged Hartree energy, E_{XC} can be reasonably approximated as a nearly-local functional of the density. The local density approximation (LDA) is the most straightforward way of constructing E_{XC}, and can be regarded as the basis for other more sophisticated functionals. The LDA E_{XC} was already mentioned in the original paper of Kohn and Sham[43] where they proposed that for systems with a slowly-varying electron density, the density can be regarded as locally unchanged and can be approximated using the homogeneous electron gas model. The resulting E_{XC} takes the form

$$E_{XC}^{LDA}[n] = \int d^3 r n[\boldsymbol{r}\epsilon_{xc}(n(\boldsymbol{r}))], \tag{2.13}$$

with ϵ_{xc} being the exchange-correlation energy per particle of the homogeneous electron gas with density $n(\boldsymbol{r})$. Eq. 2.13 shows that the total exchange-correlation energy is just the integral of the exchange-correlation energy density over all space where the electron density is homogeneous.

As expected, LDA works well for systems such as metals where the electrons are nearly free and the electron density is close to homogeneous, but it falls short to describe systems which has an inhomogeneous electron density such as atoms. In general, LDA provides good structural, elastic and vibrational properties, whereas it performs poorly for energetics such as binding energy (overbinding), activation energies of chemical reactions, and the relative stability of different bulk phases. Lastly, in general it provides a reasonable physical interpretation of electronic properties, *except* of band gaps[48].

Generalized gradient approximation (GGA)

An intuitive further development upon LDA is the generalized gradient approximation (GGA), where not only the electron density, but its gradient is incorporated in the formulation of E_{XC}. Several widely-used GGA functionals are available which have different parameterizations and all successfully calculate accurate energies to meet the need of modeling chemical reactions, thus popularizing DFT in the chemistry community. The GGA E_{XC} takes the following generalized form[47,49]

$$E_{XC}^{GGA} = \int d^3 r n(\boldsymbol{r}) \epsilon_{xc}(n, |\boldsymbol{\nabla n}|). \tag{2.14}$$

The GGA E_{XC} functional used in this thesis is the PBE functional proposed by Perdew, Burke, and Ernzerhof[49,50]. The common feature of the various GGA functionals is the exchange-correlation enhancement factor F_{xc}, which can be seen as a Taylor series expanded in terms of the density gradient. The exchange part of F_{xc} is therefore always ≥ 1, leading to a lower (larger in magnitude) exchange energy E_X and a reduced binding energy. This is why GGA functionals improve the overbinding problem of LDA. In general, when compared to LDA, GGA gives a better description of energetic properties and is more applicable to chemical modeling, but it also overestimates the lattice constants and bond lengths[48]. In addition, just like LDA, GGA fails to describe *strongly correlated* systems such as transition metal oxides, where the *d* electrons are strongly correlated with each other via the Coulomb interaction. The famous example is that DFT predicts the CoO to be metallic while it is actually an antiferromagnetic insulator[51].

There are more advanced E_{XC} functionals which are beyond the scope of this thesis. However, it should be stressed that there is *no* functional which is accurate for predicting *all* the physical properties of a certain material. Therefore, the *Jacob's ladder*, which describes that the accuracy of a theory will be consistently improved as the level of theory goes higher (which is true for wave function-based theories), does not exist in the DFT framework. A given functional may be good at predicting the geometric parameters, yet fails to predict electronic properties of a system. Therefore, in DFT calculations, the name of the functional being used should always be clearly addressed, such that the results can be correctly interpreted and the possible errors generated from using an improper functional to study a specific property can also be avoided.

2.1.4 Hybrid functionals

As far as this thesis is concerned, DFT as described above has a major deficiency in that it systematically underestimates the materials band gaps due to the unphysical self-Coulomb repulsion. Approaches with hybrid functionals have been developed and to a great extent remedied this problem.

In hybrid functionals, the exact Hartree-Fock (HF) exchange energy is mixed with the DFT exchange and correlation energies by a linear combination with specific coefficients. The reason for doing so is that in the HF theory, the self-Coulomb term is exactly cancelled by the exchange term. Thus the self-Coulomb term in DFT is expected to be also largely cancelled by including the HF exchange term into the formulation of E_{XC}. There exists many different hybrid functionals, and the hybrid functional used in this thesis is the HSE hybrid functional proposed by Heyd, Scuseria and Ernzerhof (HSE)[52,53]. The HSE E_{XC} is given as

$$E_{XC}^{HSE} = \frac{1}{4}E_X^{HF-SR} + \frac{3}{4}E_X^{PBE-SR} + E_X^{PBE-LR} + E_C^{PBE}. \tag{2.15}$$

This HSE E_{XC} is a member of the *screened* hybrid functionals. In practice, introducing the full HF exchange (E_X^{HF}) will significantly increase the computation time, thus not feasible for most of the real systems. A workaround to this problem is to separate the denominator of E_X^{HF} into the short-range (SR) part and the long-range (LR) part, and only the SR part of E_X^{HF} will be taken into account, whereas the LR part will be replaced by the DFT counterpart. By this screening approach, the computational time can be remarkably reduced. Also important is that the original LR part of E_X^{HF} gives a tail at large $\boldsymbol{r}$, which will lead to overestimation of band gaps. By substituting $E_X^{HF,LR}$ with $E_X^{DFT,LR}$, this unwanted tail can be removed and as a result a better description of the band gaps can be expected[54].

In practical calculations, one usually needs to optimize the coefficient of E_X^{HF} from $\frac{1}{4}$ to a value that gives the most accurate band gap of the object material. In this thesis, the HSE E_{XC} functional was used to evaluate the magnitude of spin-orbit splitting within the defective WS_2 monolayers in Chap. 3, as well as in Chap. 4, to give a better description of the electronic properties of the transition metal oxides (TMOs).

2.1.5 DFT for periodic systems

Bloch's theorem and k-point sampling in the reciprocal space

Based on the discussion in the preceding subsections, we can now obtain the physical properties for a many-body system by solving a set of

single-particle KS equations (Eq 2.12). This holds for atoms and molecules where the number of electrons is still manageable by current computational power. However, when it comes to solids-state materials, the number of electrons can easily be in the scale of moles (10^{23}). If a crystal contains one mole of electrons, then there will be 10^{23} KS equations to be solved, which means that a $10^{23} \times 10^{23}$ matrix needs to be diagonalized! This is an astronomical size that one cannot afford. Fortunately, for periodic crystals there is translation symmetry. As discussed in the section on point defects, a crystal can be built up by repeatedly shifting the unit cell in three dimensions by the lattice vectors. The unit cell can be seen as the smallest building block of the whole crystal. By taking the translational symmetry of the lattice into account, we no longer need to consider all the electrons in a crystal, but only the electrons inside the unit cell, as the unit cell can represent the entire crystal via repetition. Next, we need to consider the periodicity of the electronic wave function.

The atoms inside a crystal are periodically placed on the lattice sites in this crystal. As a result, the potential (V_{ext} in Eq. 2.12) from these atoms applying on the electrons shares the same periodicity as the atoms. That is, $V_{ext}(\boldsymbol{r}) = V_{ext}(\boldsymbol{r} + \boldsymbol{T})$ in Eq. 2.12, with T the translational vector (lattice vector). Therefore, the electrons in a crystal experience a *periodic* external potential. The biggest difference of dealing with solids from atoms or molecules is this periodic potential. Together with the potential, the electron density possesses also the same periodicity. However, for the electron wave function, as it is complex, its magnitude is as periodic as the potential and the density, while its phase can be arbitrary. By expanding $V_{ext}(\boldsymbol{r})$ and $\psi(\boldsymbol{r})$ in the Schrödinger equation using Fourier series, the Bloch's theorem[55] proves that in a periodic potential, the wave function is also 'quasi-periodic':

$$\psi_k(\boldsymbol{r}) = e^{i\boldsymbol{k}\cdot\boldsymbol{r}} u_k \boldsymbol{r}, \tag{2.16}$$

where $u_k(\boldsymbol{r}) = u_k(\boldsymbol{r} + \boldsymbol{T})$ is the periodic part, and $e^{i\boldsymbol{k}\cdot\boldsymbol{r}}$ is an arbitrary phase factor. In other words, the translated wave function differs from the original one only by a phase factor:

$$\begin{aligned} \psi_k(\boldsymbol{r} + \boldsymbol{T}) &= e^{i\boldsymbol{k}\cdot(\boldsymbol{r}+\boldsymbol{T})} u_k(\boldsymbol{r} + \boldsymbol{T}) \\ &= e^{i\boldsymbol{k}\cdot\boldsymbol{T}} \psi_k(\boldsymbol{r}). \end{aligned} \tag{2.17}$$

Here the wave function is built in reciprocal space, which is spanned by the k vectors (Here k has an inversed unit with respect to r: $\frac{1}{length}$, therefore it is *reciprocal*). The unit cell in the reciprocal space is the first Brillouin zone (BZ). Just as in the case of real space, in reciprocal space only the BZ is needed to describe the physical properties of the entire crystal.

Similar to the wave function in atoms and molecules, the wave function in solids is also formed by the linear combination of basis sets. However, whereas the localized atomic orbital-like functions are the best choice of basis sets for atoms and molecules, they are not the best candidate of basis sets for extended systems because they do not reflect the periodicity of the lattice. Here, since $u_k(\boldsymbol{r})$ is periodic, it can be expanded by a Fourier series of plane waves

$$u_k(\boldsymbol{r}) = \sum_G C_{Gk} e^{i\boldsymbol{G}\cdot\boldsymbol{r}}. \tag{2.18}$$

Here C_{Gk}'s are the complex Fourier coefficients and G's are all the possible lattice vectors in reciprocal space. Each Fourier basis function $e^{i\boldsymbol{k}\cdot\boldsymbol{r}}$ represents a plane wave travelling in space with the direction perpendicular to G. Theoretically, the summation goes over infinitely many G's. But in reality the coefficient C_{Gk} becomes smaller and smaller when $|\boldsymbol{G}|^2$ increases. Therefore, we can truncate the summation by considering only $\boldsymbol{G}$'s smaller than a certain value. We define a cut-off energy $E_{cut} = \frac{\hbar^2}{2m}|\boldsymbol{G}|^2$, and include only the plane waves with energies lower than this cut-off. In practical calculations, the cut-off energy should be tested to be high enough to render reliable results. Typically, the convergence criterion is that the energy difference of two calculations with different E_{cut} should be less than 1 meV/atom.

The evaluation of many quantities, including the electron density, depends on the integration of the wave function over the entire reciprocal space. Ideally, we need to integrate all possible points in reciprocal space. However, since the wave function can be considered to be a continuous function of k, and varies slowly with k, we can replace the integral with a summation over discrete k-points. The electron density is an example:

$$\begin{aligned} n(\boldsymbol{r}) &= \int d^3\boldsymbol{k} \left|\psi_k(\boldsymbol{r})^2\right| \\ &\approx \sum_k \left|\psi_k(\boldsymbol{r})\right|^2. \end{aligned} \tag{2.19}$$

For an accurate evaluation of the total energy, the number of k-points and the type of k-point sampling must be adequate. By symmetry operations, the BZ can be further reduced to the irreducible Brillouin zone (IBZ). The selected k-points should also cover the whole IBZ to be representative for all the other k-points. There exists many methods of selecting a set of proper k-points but this introduction will not cover these details. In practice, the number of k-points should be tested to reach the criterion of 1 meV/atom. The convergence of the cut-off energy and the k-mesh is the uttermost important prerequisite for obtaining accurate and reliable results.

Pseudopotentials

The electrons around a nucleus can be classified into core electrons and valence electrons. The chemical and physical properties of a material are determined solely by the valence electrons as they are more distant from the nucleus and are more chemically/physically active. In contrast, the core electrons dwell around the vicinity of the nucleus and are very inert. Although the core electrons do not play an important role in determining chemical or physical properties of a material, much computational effort is required to describe these core states. The valence wave function oscillates rapidly near the vicinity of the nuclei because it is required to be orthogonal to the core states, and these oscillations can only be described by a large number of basis sets. In addition, while Bloch's theorem allows the wave function to be expanded by plane wave basis sets in periodic systems, those plane wave functions are even worse at describing the oscillating wave function than other types of basis sets. Therefore, even more plane waves are required for a proper account of the core states. As such, the idea of pseudopotential (PS) has arised to simplify the problem.

As shown in Fig. 2.3, the PSs replace the core potential with a smoother effective potential in the core region defined by the cut-off radius r_c, where no nodes (oscillations) are present. This replacement does not affect the calculation results much as only the core part is replaced, while it makes the calculation more efficient by reducing the number of basis sets needed. There have been numerous ways of designing the PSs. In 1994, the projector augmented wave[56,57] (PAW) method was proposed by Blöchl. The PAW method possesses both the all-electron accuracy and the PS efficiency. In the PAW framework, the valence part of the wave function is described by a smooth pseudo wave function, and the core part is expanded by a set of localized atomic-like basis functions. The region where the atomic basis functions should be expanded is defined by the augmentation sphere around each atom. In this thesis, the Vienna Ab initio Simulation Package[59–61] (VASP) has been used to perform all the calculations. VASP is a DFT code employing the plane wave basis set, and the PAW PSs were used at all the times. The crystal structure as well as the electronic densities are visualized using the VESTA program[1]. The detailed computational settings specific to each chapter will be given in the *computational details* section of the respective chapter.

2.2 Modeling point defects in nanomaterials

As will be discussed in great detail in the following chapters, point defects, including vacancies, interstitials, antisites, or defect complexes containing

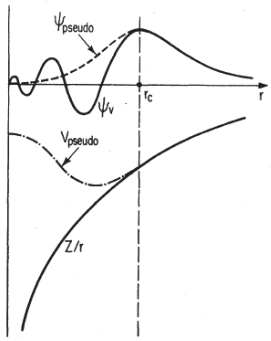

Figure 2.3: Schematic representation of the pseudopotential approach in general. The dashed line denotes the core potential V and ϕ the corresponding wave function. The pseudopotential V_{PS} modifies the wave function inside the core radius r_c to the much smoother pseudo wave function ϕ_{PS}. Figure reprinted with permission from Ref. 58: Payne, M., Teter, M. P., Allan, D. C., Arias, T. A. Joannopoulos, J. D. *Rev. Mod. Phys.* **64**, 1045 (1992). Copyright (1992) by the American Physical Society.

some of the above defect kinds, play a crucial role in determining the physical and chemical properties, and the applications, of a material. In this section the focus is on how to model point defects in nanomaterials.

2.2.1 The supercell approach

In the previous section it was shown that a crystal structure can be represented by its unit cell. An unit cell can be defined in different ways and it is the smallest repeating unit of the periodic crystal structure. Fig. 2.4 shows the unit cell of a 2D WS_2 monolayer and illustrates that the unit cell can be translated in the $x-y$ plane. One thing worth noting here is that if the model of interest is not a bulk material, but a surface or a 2D slab (monolayer or multilayers), a vacuum space needs to be placed to isolate the unit cells along the vertical axis. The size of the vacuum separation should be tested so that it is large enough and that the resulting energy difference is converged to 1meV/atom, thereby reducing the fictitious interaction between the unit cells. Normally it is sufficient to have a vacuum space larger than 15 Å. The use of unit cells makes the calculation as well as the data analysis a lot easier. However, when defects are present in the lattice, they break the translational symmetry and therefore a larger *supercell* should be used. Fig. 2.5 shows the supercell of a WS_2 monolayer containing a S monovacancy (V_S-WS_2). The supercell is needed in the case of defects as (1) it represents a new, and larger, smallest repeating unit to

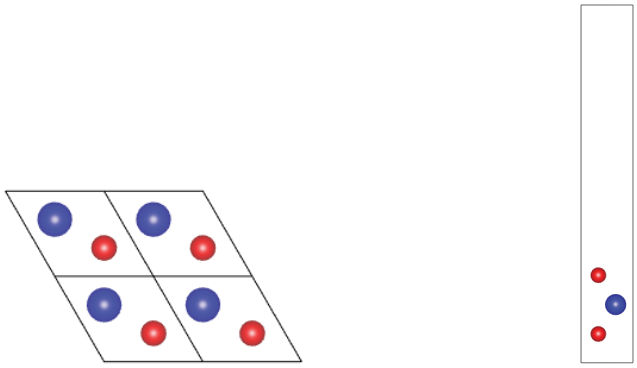

(a) Unitcell of WS_2 (top view) (b) Unitcell of WS_2 (side view)

Figure 2.4: The unit cell model of WS_2. The W atoms are shown in blue, and S atoms in red. The top-viewed unit cell is repeated 2×2 to show the crystallographic periodicity. The side-viewed unit cell is to show the large vacuum separation in along the vertical direction.

build up the defective crystal, and (2), more importantly, it reduces the artificial defect-defect interaction if one wants to study isolated defects. The supercell size also should pass the energy convergence crterion of 1 meV/atom. As shown in Fig. 2.5, a 6×6 supercell is needed for V_S@WS_2. The distance between two nearest-neighboring defect sites is around 19 Å. Although in this thesis only neutral defects are considered, it is worth mentioning that the defect isolation becomes even more crucial when the defects are charged as the electrostatic interaction between these defects decays slowly with the cell size, and an additional correction should be taken into account[62–65].

2.2.2 Defect formation energy

The formation energy of is the key quantity to understand the stability and predict the equilibrium concentration of the point defects. The basic idea is to compare the DFT-calculated energy difference of the defective supercell and the perfect supercell with respect to the certain reference states. Often the elemental phases of the constituent atoms of a compound are taken as these reference states. Thus the stability of a point defect is relative to the elemental phases of the constituent atoms.

The general formula of defect formation energy is[62,66]

$$E_f = E_{defect} - E_{perfect} - \sum_i \Delta n_i(\mu_i) + q\epsilon_F, \tag{2.20}$$

whereby E_f is the formation energy, E_{defect} the total energy of the defect

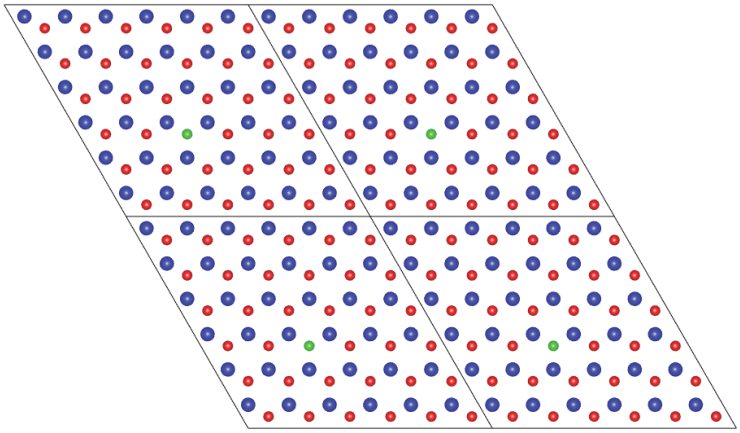

Figure 2.5: A 6×6 supercell model of the WS_2 monolayer with S vacancy V_S-WS_2. The S monovacancy site is marked in green. The supercell is repeated 2×2 to show the periodicity and the separation of the defect sites.

cell, $E_{perfect}$ the total energy of the perfect cell. The Δn_i's are the number of atoms added ($\Delta n_i > 0$) to or subtracted ($\Delta n_i < 0$) from the perfect cell and the μ_i's are the atomic chemical potentials for these atoms. q is the charge of the defect and ϵ_F is the Fermi energy, i.e. the electronic chemical potential. For instance, the formation energy of a neutral ($q = 0$) sulfur monovacancy in a 6×6 WS_2 supercell ($W_{36}S_{72}$) is

$$E_f(V_S) = E(W_{36}S_{71}) - E(W_{36}S_{72}) + \mu_S. \tag{2.21}$$

Since the charged defects are not considered in this thesis, $q = 0$ in Eq. 3.1 and the last term vanishes. The atomic chemical potentials μ can be regarded as the atomic reservoir with which the atoms are exchanged. The remaining work to fully define Eq. 2.21 is determining the boundaries of these atomic chemical potentials.

Once the range of defect formation energy is calculated using Eq. 2.21, the concentration and the temperature dependence of the concentration for a particular type of point defect can be subsequently evaluated using the following equation

$$f = \frac{F}{n} = x_d E_f + k_B T[x_d \ln x_d + (1 - x_d)\ln(1 - x_d)]. \tag{2.22}$$

This is the expression of free energy per atom f in terms of the equilibrium defect concentration x_d. F is the total free energy of the system, n is the total number of atoms, k_B is the Boltzmann constant and T is the temperature in K. From the minimum of $f(x_d)$, the equilibrium defect concentration x_d at different temperatures can be evaluated.

2.2.3 Derivation of the boundaries of chemical potentials

It would be clearest to use an example to illustrate the derivation of the boundaries of chemical potentials. We take the WS_2 monolayer for this purpose. In this case study, we will define the boundaries of the chemical potential of W atoms (μ_W) and S atoms (μ_S), respectively.

We start from the thermodynamical background of the formation energy, and recall that the Gibbs free energy is defined by

$$G = H - TS, \tag{2.23}$$

where H is the enthalpy of the system, T is temperature in Kelvin, and S is the entropy. The enthalpy is defined as

$$H = E + pV. \tag{2.24}$$

Here E is the total energy, p is pressure of the system, and V is the system volume. Another definition of G for homogeneous system is

$$G = \sum_i n_i \mu_i \tag{2.25}$$

By the definition of Eq. 2.25, chemical potentials and the Gibb's free energy are related. DFT calculates the electronic total energy of a system without any pressure and temperature (p=0 Pa and T = 0 K). This energy becomes the total energy in Eq. 2.24. Furthermore, when p = 0 Pa and T = 0 K, the Gibbs free energy and enthalpy directly become the total energy of the system, which can be regarded as the summation of the chemical potentials of all the constituent atoms:

$$G = H = E = \sum_i n_i \mu_i \tag{2.26}$$

Viewing Eq. 2.26 from another angle, we can find that the chemical potential μ_i is in fact simply the total energy per atom. This also corresponds to the original definition of the chemical potential, which is the partial derivative of the internal energy E with respect to the number of particles n: $\mu = \frac{\partial E}{\partial n}$. Chemical potentials appear when there is a net change in the number of particles in a system. In our case, this is creating defects in a crystal.

Based on the short introduction of the thermodynamical terms, we can now proceed with defining the chemical potentials. First, we imagine the formation of the ML WS_2 as a chemical reaction, in which the W atoms and S atoms are taken respectively from their bulk reservoirs to form a unit of WS_2:

$$W_{(bulk)} + 2S_{(bulk)} \rightarrow WS_{2(ML)} \tag{2.27}$$

By definition, the formation enthalpy (heat of formation) of a reaction is given by $\sum \mu_{product} - \sum \mu_{reactant}$. Thus for the reaction above we have

$$\Delta H_{WS_2} = \mu_{WS_2,ML} - \mu_{W,bulk} - 2\mu_{S,bulk}. \tag{2.28}$$

Please note that here $\mu_{W,bulk}$ and $\mu_{S,bulk}$ are the energy per atom of W bulk in the bcc structure, and S in bulk α-S, respectively, as we consider these two phases as the atomic reservoirs for WS_2. μ_{WS_2} is the energy per forming unit of WS_2.

Furthermore, under chemical equilibrium, the W and S atoms can 'flow' freely between the atomic reservoirs and WS_2 without losing any energy. This is described by the following reaction:

$$W + 2S \leftrightarrow WS_2. \tag{2.29}$$

The free exchange of atoms is achieved when

$$\mu_W + 2\mu_S = \mu_{WS_2} \tag{2.30}$$

Under realistic experimental conditions, there could be an excess amount of constituent atoms of a product compound in the surroundings depending on different synthesis routes. In order to take this factor into account, in DFT calculations the usual practice is to consider the *poor* and *rich* extremes of the amount of the constituent atoms. For instance, we can consider the W-rich (S-poor) and the W-poor (S-rich) conditions for ML WS_2. In the W-rich condition, there are extra W atoms in the surroundings of WS_2. With the help of Eqs. 2.28 and 2.30, we can now derive the boundaries for μ_W and μ_S in the two conditions mentioned above.

In the W-rich condition, it is required that

$$\mu_W = \mu_{W,bulk}. \tag{2.31}$$

Otherwise, if μ_W is larger than $\mu_{W,bulk}$, then the W atoms will leave WS_2 and start to precipitate as bulk W metal because atoms always move from a place with higher chemical potential to a place with a lower chemical potential. By combining Eqs. 2.28, 2.30 and 2.31, we can obtain the lower boundary for μ_S as

$$\mu_S = \mu_{S,bulk} + \frac{1}{2}\Delta H_{WS_2}. \tag{2.32}$$

In contrast, in the S-rich condition,

$$\mu_S = \mu_{S,bulk}. \tag{2.33}$$

Thus by Eqs. 2.28, 2.30 and 2.33, we have the lower limit of μ_W:

$$\mu_W = \mu_{W,bulk} + \Delta H_{WS_2} \tag{2.34}$$

One can then obtain the upper and lower limits for both μ_W and μ_S:

$$\mu_{W,bulk} + \Delta H_{WS_2} \leq \mu_W \leq \mu_{W,bulk}, \tag{2.35a}$$

$$\mu_{S,bulk} + \frac{1}{2}\Delta H_{WS_2} \leq \mu_S \leq \mu_{S,bulk}. \tag{2.35b}$$

However, in order to use Eq. 2.35 for DFT calculations, we need to replace the thermodynamical terms with energy terms. For this purpose, we see that $\mu_{WS_2,ML} = E_{WS_2,ML}$, $\mu_{W,bulk} = E_{W,bulk}$ and $\mu_{S,bulk} = E_{S,bulk}$. Eventually, we arrive at the final expressions of the boundaries of μ_W and μ_S which are used to calculate the defect formation energies in Chapter 2:

$$E_{WS_2} - 2E_S \leq \mu_W \leq E_W \tag{2.36a}$$

$$\frac{1}{2}(E_{WS_2} - E_W) \leq \mu_S \leq E_S. \tag{2.36b}$$

Chapter 3

The role of point defects in lead chalcogenides

The content of this chapter was published in J. Phys.: Condens. Matter **27**, *355801 (2015).*

Intrinsic defects are of central importance to many physical and chemical processes taking place in compound nanomaterials, such as photoluminescence, accommodation of off-stoichiometry, and cation exchange. Here, the role of intrinsic defects in the aforementioned processes inside rock salt (*rs*) lead chalcogenide systems PbS, PbSe, and PbTe (PbX, with X=S, Se, Te) were studied systematically using *first principles* density functional theory. Vacancy, interstitial, Schottky, and Frenkel defects were considered. Rock salt PbO was included for comparison. The studied physical properties include defect formation energy, local geometry relaxation, Bader charge analysis, and electronic structure. The defect formation energies indicate that monovacancy defects and Schottky defects are favored over interstitial and Frenkel defects. Schottky dimers, where the cation vacancy and anion vacancy are adjacent to each other, have the lowest defect formation energies at 1.27 eV, 1.29 eV, and 1.21 eV for PbS, PbSe, and PbTe, respectively. Our results indicated that the Pb monovacancy gives rise to a shallow acceptor state, while the X vacancy generates a deep donor state, whereas Schottky defects create donor-acceptor pairs inside the band gap. It is expected that off-stoichiometry is accommodated by X monovacancies rather than by Pb monovacancies due to the lower formation energies of V_X defects. The surprisingly low formation energy of Schottky dimers suggests that they may play an important role in cation exchange processes, in contrast to the current notion that only single point defects migrate during cation exchange.

3.1 Introduction

Lead chalcogenides (PbX, X=S, Se and Te), a family of narrow band gap IV-VI semiconductors, have been the subject of intensive research due to their applications in many fields such as thermoelectric energy converters[67,68], thermal photovoltaic devices[69], infrared lasers[70], and light-emiting diodes.[71] Together with the CdX chalcogenides family (CdS, CdSe, CdTe), the PbX systems are abundantly used in heterogeneous nanocrystals (HNCs) to create new materials with novel and tunable physical properties.[18–20]

By physical nature, defects inevitably exist in crystals, and play a pivoting role in the growth, synthesis and in many physical properties of HNCs and multicomponent quantum dots (QDs). First, point defects, depending on the position of their defect states with respect to the band gap, can determine whether the process of the electron-hole recombination in nanocrystals is radiative or non-radiative[72,73]. Thus point defects directly affect the quantum yield of nanocrystal (NC) QDs. Second, there is much unclarity in the literature about how the off-stoichiometry of the NCs[74,75], a typical product of wet chemical synthesis, affects the physical properties. In particular, it is at present unclear whether the excess or depletion of anions or cations is accomodated only at the surface, or also at the interior of the NCs. Third, the very important cation exchange (CE) process that is used to create core-shell type structures and synthesis of NCs in deviating crystal structures[5,7,19,21–26], requires the migration of cations, as shown in many experimental studies. In *rs* chalcogenides, this is assumed to be mediated by cation vacancies[7,19]. Groeneveld *et al.* proposed that ZnSe-CdSe colloidal quantum dots (QD) can be tailored via a CE mechanism mediated by Frenkel pairs of Zn interstitials Zn_i and Zn vacancies V_{Zn}.[5] Casavola *et al.* brought forth a plausible mechanism that the growth of PbSe/CdSe core/shell nanocrystal is mediated by CE, where the cation vacancies assist the migration of cations.[19] Yingzhuo *et al.* proposed that CdSe/ZnSe core/shell QD can be synthesized in aqueous environment through CE.[26] Finally, Yalcin *et al.* recently found that the CE in the solid-solid-vapor (SSV) growth of PbSe/CdSe core/shell HNCs is mediated by Cd vacancies at the PbSe-CdSe interface.[7] However, it is difficult, or even impossible to determine experimentally which types of defects are present in the material and what their role is in, e.g., CE progresses. It is only until recently, that more insight of CE was unveiled by *first principles* calculations of Ag ions in wurtzite CdSe[76]. To the best of our knowledge, our current work is the first DFT study discussing point defects in *rs* PbX in the context of the CE precess. Although in all the experimental literature given above, monovacancies are presumed to enable CE, we give an important finding

that vacancy comlexes, *i.e.*, Schottky defects, can not be excluded in CE because they possess significantly lower formation energies than monovacancies do. In all these phenomena, the presence of vacancies and other point defects is a crucial parameter. In this work, we identify and characterize the most important point defects in PbX chalcogenides, and discuss their role in the aforementioned processes.

In the current study, four kinds of point defects are considered. These are vacancy, interstitial, Schottky dimer/pair, and Frenkel pairs. These defects are schematically shown in Fig. 4.2. Vacancies and interstitials contain only one defect site, while Schottky and Frenkel defects include two defect sites. A Schottky defect consists of a cation-anion vacancy pair. Schottky dimer is defined as the cation vacancy and the anion vacancy sites being adjacent to each other, and in the Schottky pair configuration, the two defect sites are separated as far as possible within a supercell. A Frenkel defect is created when an atom moves from its original place to an interstitial site, whereby a vacancy site and an interstitial site are generated. In binary compounds such as PbX, both the cation Frenkel defect and the anion Frenkel defect need to be considered.

Defects in PbX have received much attention by scientists for decades. The related research has been carried out both experimentally[77–82] and theoretically.[78,83–93] Miller *et al.* found that the formation energy of a Frenkel defect is higher than a Schottky defect in PbTe, hence the diffusion is essentially controlled by a vacancy-type mechanism.[77] By using positron annihilation technique, Polity *et al.* established the relationship between V_{Pb} concentration and positron lifetime.[78] Yoneda *et al.* reported that Schottky defects will form in PbTe when the crystal is heated over 200 °C.[80] Via the measurements of step-scan Fourier-transform infrared photoreflectance (step-scan FTIR PR) on a PbTe thin film, the defect state of V_{Te} was found at 29.1 meV above the conduction band maximum (CBM), and another defect state at 18.1 meV below the valence band maximum (VBM) may be attributed to V_{Pb} or threading dislocations, whereas no states were found in the band gap.[81] Koumoulis performed NMR measurements on PbSe, and reported *p*-type shallow acceptor state and *n*-type deep state at midgap.[82]

Theoretical calculations were also performed on PbX systems. Berashevic carried out a detailed study on vacancy defects in α-PbO (litharge structure)[91], and found the charged defect states for V_{Pb}^{2-} at 0.1 eV below the VBM, and V_{O}^{+} at 1.03 eV above the VBM, which were stabilized by charge transfer. For PbS, Ding *et al.* studied the $(\bar{1}00)$ surface, and found the *p*-type V_{Pb} and *n*-type V_S defect states. They also found that the structural relaxation at the surface is opposite to the case of bulk PbS: around the defect site, the nearest-neighboring (NN) atoms of the defect

site will be repelled outwards, while the next-nearest-neighboring (NNN) atoms will move toward the defect site.[87] Walsh studied vacancy defects and Schottky defects in their neutral and charged states.[89] The Schottky defect was found to be preferred over vacancy defects as it has a lower formation energy. Donghun *et al.* found for PbS quantum dots (QD) that off stoichiometry will introduce new states which are highly localized on certain surface atoms.[93] For PbSe, Peng *et al.* performed a series of calculations for bulk PbSe doped with 26 substitutional impurities.[90] Wrasse *et al.* studied the electronic structure of both bulk and nanowire PbSe with group III substitutional impurities.[92] For PbTe, there are a series of theoretical studies concerning the defect states: Parada and Pratt made the first attempt to describe the electronic structure of defective PbTe using the Slater-Koster model,[83,84] and Lent *et al.* used a tight-binding method to give a qualitative description of the deep defect state in PbTe.[85] However the calculations in Refs. 838485 are non-self-consistent calculations. Recently, Ahmad and Hoang employed self-consistent DFT calculations for vacancies and substitutional impurities in both bulk[86,88] and thin-film[88] PbTe. Furthermore, there are several other theoretical investigations done on perfect PbX systems for structural and electronic properties[94–97], and thermodynamic properties.[98–100] All of these studies are limited to perfect PbX crystals, though, thus no defect was induced.

The formation energy of defects is key to verify which kind of defect(s) are more likely to be formed inside a crystal, and thus may determine the CE process. Using the *first principles* DFT approach, we firstly aim to compare the relative stability of the defect species inside PbX in terms of defect formation energy, so that we can identify which defects may be involved in the CE process. Second, we would like to provide a fundamental and panoramic view of the physical properties of the point defects inside PbX, which is indispensible for further study and applications of these materials. Besides defect formation energies, the physical properties including local geometry relaxation, charge transfer, and electronic structure, were analyzed. The typical point defects for these compounds are: vacancy, interstitial, Schottky, and Frenkel. Even though PbO occurs in the litharge structure rather than the rock salt (*rs*) phase[101], we include the calculations of *rs* PbO for comparison.

The content of this Chapter is organized as follows: the computational details are given in Sec. 3.2. The results and discussions are presented in Sec. 3.3 and 3.4, respectively; first we will compare the relative stability of all the defect types, after which we select the more stable ones for a more detailed study of physical properties. Finally, conclusions are given in Sec. 3.5.

3.2 Computational Details

3.2.1 Computational Settings

All the calculations were carried out using the *first principles* DFT code VASP[59–61] within the Projector-Augmented Wave (PAW) framework.[56] The Generalized Gradient Approximation (GGA) formulated by Perdew, Burke, and Ernzerhof (PBE)[49] was employed for the exchange and correlation energy terms. The cut-off energy of the wave functions was 500 eV. The cut-off energy of the augmentation functions was 700 eV. Due to computational limitations, we used only the embedded scalar relativistic effect in the VASP code, and the spin-orbit coupling (SOC) is not explicitly included in our calculations. For supercells, the sampling in the reciprocal space was done by using a $2 \times 2 \times 2$ k mesh with 4 or 6 irreducible k points depending on the symmetry of the systems. For the unit cell of PbX and elemental Pb, a $24 \times 24 \times 24$ k mesh containing 455 irreducible k points was used. And for elemental S, due to the large unit cell size, a $4 \times 4 \times 2$ k mesh was used with 18 irreducible k points. For elemental Se and Te, a $24 \times 24 \times 20$ mesh with 1103 irreducible k points was used. All the k meshes were Γ-centered in the reciprocal space.

In our study, we used $3a_0 \times 3a_0 \times 3a_0$ *rs* supercells containing 216 atoms for all the four PbX systems. Here a_0 is the lattice constant, and the optimized a_0 is 5.233 Å for PbO, 5.994 Å for PbS, 6.207 Å for PbSe, and 6.561 Å for PbTe. Also the band gaps of the relaxed PbX systems are calculated. These calculated values are compared with selected literature values in Table 3.1 for lattice constants and in Table 3.2 for band gaps. The calculated lattice parameters of PbX are slightly larger than the corresponding experimental values (1.0% ~1.5%). This is not unusual for the DFT-GGA approach[49].

For the comparison of band gaps, we included in Table 3.2 DFT results from the literature calculated both with and without SOC. The inclusion of SOC significantly reduces the band gaps of PbX by pushing up the X p state valence band maximum (VBM) while pushing down the Pb s state conduction band minimum (CBM) The negative band gap, as addressed in Ref. 97 is caused by the interchange of the cation p character and the anion p character in the VBM and CBM at the L point when SOC is included. This unphysical behavior is cured by the hybrid functional (HSE) calculation with SOC, as shown in Table 3.2.

The supercells were built using the optimized lattice constant from the corresponding unit cells. The structural models are shown in Fig. 4.2. The defect sites were put as far as possible from each other to avoid artificial interactions among them. In order to determine the defect formation energy, we need to calculate the energy of the constituent elements in each

compound was calculated to serve as reference energies. Elemental Pb was calculated using a 4-atom face-centered cubic (FCC) unit cell. For elemental anion phases, we employed molecular triplet O_2 for oxygen, 128-atom unit cell for α-sulfur, and a 3-atom trigonal unit cell for selenium and tellurium, respectively. The calculated energies are -3.572 eV/atom (Pb), -4.959 eV/atom (O), -4.126 eV/atom (S), -3.483 eV/atom (Se), and -3.142 eV/atom (Te).

Both the supercell shape and atomic positions were allowed to relax during geometry optimization. The optimization was considered as converged if the difference in energy between two subsequent electronic optimization steps was smaller than 1.9×10^{-4} eV, while the forces on the atoms were smaller than -0.02 eV/Å.

3.2.2 Definition of defect formation energies

In order to allow a comparison of the relative stability of these defects inside a crystal, we need to first define the formulas to calculate defect formation energies. This choice of definitions allows direct comparison with phase diagrams.[108–111] In the pseudo-binary phase diagrams, the stoichiometric configuration of these three compounds (with 50% atomic percent of the anions) are all very stable at high temperatures as the melting point of the three compounds at stoichiometric configuration is 1118 °C for PbS, 1079 °C for PbSe, and 924 °C for PbTe, respectively. Therefore the choice of stoichiometric perfect PbX, and elemental phases of Pb cation and the X anions as reference states for calculating the defect formation energy is reasonable. Here the number of atoms is always conserved, and all defects are neutral.

The general fomula of defect formation energy is[62,66],

$$E^f = E_{defect} - E_{perfect} - \sum_i \Delta n_i(\mu_i) + q\epsilon_F, \tag{3.1}$$

whereby E^f is the formation energy, E_{defect} the total energy of the defect cell, $E_{perfect}$ the total energy of the perfect cell. The Δn_i's are the number of atoms added ($\Delta n_i > 0$) to or subtracted ($\Delta n_i < 0$) from the perfect cell and the μ_i's are the atomic chemical potentials for these atoms. q is the charge of the defect and ϵ_F is the Fermi energy, i.e. the electronic chemical potential.

This expression simplifies for the calculations described in this paper; the possibility of charged defects has not been considered and therefore $q = 0$ in Eq. 3.1, so that the last term vanishes. The atomic chemical potentials μ can be regarded as the atomic reservoir with which the atoms are exchanged. For off-stoichiometric defects (vacancies and interstitials in our case), we set $\mu_{Pb} = E(Pb)$ and $\mu_X = E(X)$, where $E(Pb)$ and $E(X)$

Table 3.1: Calculated lattice constants a (Å) of the relaxed unit cell for PbX systems compared with previous theoretical and experimental[102] results. The methods of calculation are given by *basis set-xc functional*.

PbX	LAPW-PZ81[a]	PAW-PBE[b]	PAW-HSE03[b]	PAW-PBE[c]	PAW-PBEsol[d]	PAW-PBE[e]	This work (PAW-PBE)	Exp.[f] at 300 K
PbO	–	–	–	–	–	5.27	5.233	–
PbS	5.906	6.004	5.963	5.992	5.905	–	5.994	5.936
PbSe	6.098	6.214	6.170	6.200	6.104	–	6.207	6.124
PbTe	6.439	6.568	6.519	6.556	6.448	–	6.561	6.462

[a] Ref. 94. LAPW: Linearized Augmented Plane Wave. PZ81: The Perdew-Zunger functional[103]
[b] Ref. 97. HSE03: The hybrid functional developed by J. Heyd, G. E. Scuseria, and M. Ernzerhof.[52]
[c] Ref. 98
[d] Ref. 104. PBEsol: A new PBE intended for solid state and surface systems.[105]
[e] Ref. 101
[f] Ref. 102

Table 3.2: Calculated band gaps E_g (eV) of the relaxed unit cell for PbX systems compared with previous theoretical and experimental[102] results. The values with SOC included are in given in parentheses. The methods of calculation are given by *basis set-xc functional*.

PbX	LAPW-PZ81[a]	PAW-PBE[b]	PAW-HSE03[b]	PAW-PBE[c]	PAW-GW[d]	PAW-PBEsol[e]	This work (PAW-PBE)	Exp.[f] at 300 K
PbO	–	–	–	–	–	–	0.99	–
PbS	0.29	0.37 (-0.01)	0.67 (0.31)	0.44 (0.07)	0.20	0.31 (0.14)	0.47	0.37-0.40
PbSe	0.17	0.30 (-0.12)	0.58 (0.18)	0.31 (0.02)	0.18	0.21 (0.21)	0.43	0.26-0.29
PbTe	0.19	0.73 (-0.01)	0.98 (0.25)	0.81 (0.09)	0.29	0.65 (0.03)	0.83	0.29-0.32

[a] Ref. 94. SOC included. LAPW: Linearized Augmented Plane Wave. PZ81: The Perdew-Zunger functional.[103]
[b] Ref. 97. HSE03: The hybrid functional developed by J. Heyd, G. E. Scuseria, and M. Ernzerhof.[52]
[c] Ref. 98
[d] Ref. 106 SOC included.
[e] Ref. 104. PBEsol: A new PBE intended for solid state and surface systems.[105]
[f] Ref. 107

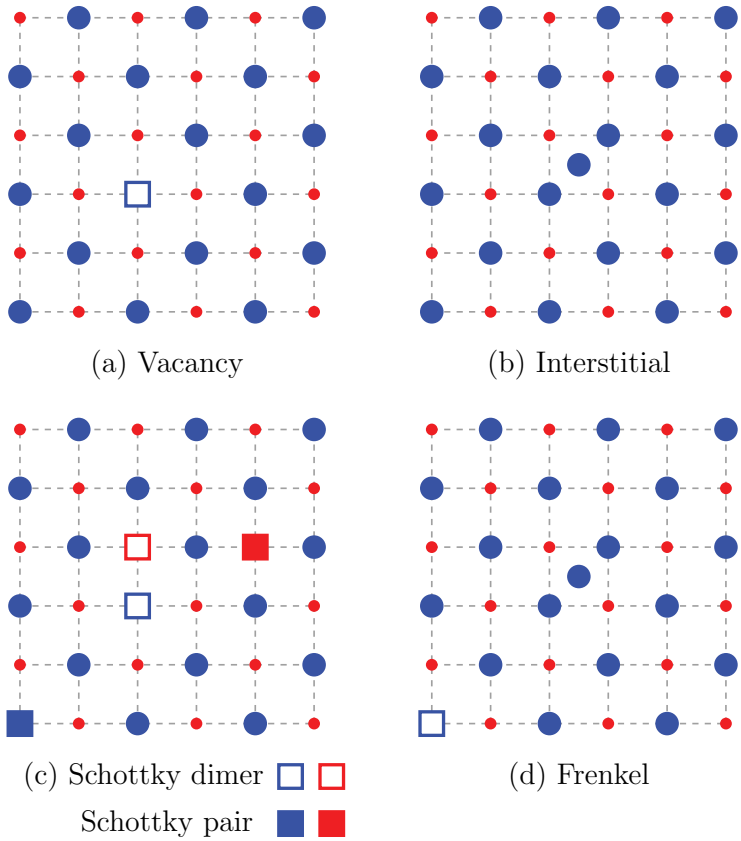

Figure 3.1: 2D Schematic of the supercell models used in this study. The models are $3 \times 3 \times 3$ PbX supercells with the *rs* structure. Pb atoms are depicted in red, and X atoms in blue. Vacancy and interstitial defects can be either at the Pb or X site. The interstitial atom is at the tetrahedral site formed by its counter atoms. (the interstitial Pb atom is surrounded by four Pb atoms and four X atoms, and vice versa.) Schottky dimer and Schottky pair are shown in the same supercell only for showing their configurations, in calculations they are introduced in two separate supercells. The Frenkel defect can be both for Pb atoms or for X atoms. Note that the inter-defect distance in the Schottky and Frenkel configuration is longer than in the 3D models.

are the energies of Pb metal and elemental phases of chalcogen atoms X, respectively. If we define $N = 108$ as the number of one atomic specie inside the PbX supercell, then $E_{perfect}$ becomes $E(Pb_N X_N)$, and the following equations can be obtained for vacancies and interstitials:

Vacancies:

$$E^f_{v,Pb} = E(Pb_{N-1}X_N) - E(Pb_N X_N) + E(Pb), \tag{3.2a}$$

$$E^f_{v,X} = E(Pb_N X_{N-1}) - E(Pb_N X_N) + E(X). \tag{3.2b}$$

Interstitials:

$$E^f_{i,Pb} = E(Pb_{N+1}X_N) - E(Pb_N X_N) - E(Pb), \tag{3.2c}$$

$$E^f_{i,X} = E(Pb_N X_{N+1}) - E(Pb_N X_N) - E(X). \tag{3.2d}$$

For stoichiometric defects, i.e. Schottky and Frenkel, the bulk PbX is regarded as the reference atomic reservoir, therefore $\mu_{Pb} + \mu_X = E(PbX)$, where $E(PbX)$ is the energy of bulk PbX per PbX Pair. The defect formation energies are then evaluated by the following equations:

Schottky defects:

$$E^f_{Schottky} = E(Pb_{N-1}X_{N-1}) - \frac{107}{108}E(Pb_N X_N). \tag{3.3a}$$

Frenkel defects:

$$E^f_{Frenkel} = E(Pb_N X_N)_{Frenkel} - E(Pb_N X_N). \tag{3.3b}$$

3.2.3 Analysis of charge density differences

The charge density difference can be used to describe the charge density changes caused by a defect inside a system. It is defined for the chosen defects as follows[112]:

$$\Delta\rho = \rho(defect) - [\rho(Pb\ sublattice) + \rho(X\ sublattice)], \tag{3.4}$$

which is the difference of charge density between the defective system and the sum of its cation and anion sublattices, keeping the positions of the atoms the same. We compare $\Delta\rho$ of the nearest-neighboring (NN) atoms around the defect site with $\Delta\rho$ of other atoms more distant from the defect site, then the influence on charge distribution from defect sites can be clearly seen. We also examined the influence of geometry relaxation on charge density difference by comparing the $\Delta\rho$ patterns calculated using the initial geometries and the relaxed final geometries. We found that the two $\Delta\rho$ patterns are almost identical, indicating that geometry relaxation has very little effect on charge density difference. In this work, the charge density difference was calculated using the relaxed structures.

3.3 Results

We separate the discussion of point defects (single defect site: vacancy and interstitial) and stoichiometric defects (double defect sites: Schottky and Frenkel) as these two groups have different defect configurations. We first compare the formation energy of these defects to determine their relative stability, and choose the more stable ones for further discussion of local relaxation, charge distribution and electronic structure.

3.3.1 Defect formation energy

The results of defect formation energies are shown in Fig. 3.2 and Table 3.3. For *rs* PbO, only the cation and anion vacancies are structurally stable. Interstitials, Schottky and Frenkel defects in *rs* PbO all led to litharge-like structures during the geometry relaxation. Therfore we only include vacancy formation energies for *rs* PbO here.

The defect formation energy exhibits certain trends along O → S → Se → Te. Along the direction of increasing atomic size of the chalcogen atom, the formation energy of V_{Pb}, V_X and anion Frenkel are increasing, but the formation energy of cation Frenkel defects, Schottky dimer and Schottky pair are decreasing. Only the formation energy of interstitials shows a dip for PbSe.

Comparing the magnitude of formation energy of these defects, it is clear that vacancies and Schottky defects are lower than those of interstitial and Frenkel defects (except that I_{Pb} is lower than V_X for PbSe) , as shown in Fig. 3.2 and Table 3.3 Although $E^{f}_{v,Pb}$ and $E^{f}_{v,X}$ can not be compared directly since they were calculated with different stoichiometries and different formulas, the current results indicate that vacancy-type defects are dominant, and therefore CE may be driven by the more easily formed cation vacancies.[7,113] Schottky defects are also energetically favored defects, but they were not seriously considered for the CE processes. Frenkel defects in PbX systems have a much higher formation energy than Schottky defects because the interstitial sites within the Frenkel configuration induce a considerable distortion due to local expansion of the lattice. For Schottky defects, the Schottky dimer is always more favored than the Schottky pair.

There are only a handful of defect formation calculations done by *ab – initio* DFT methods for PbX.[88,89,114] The results from literature and our calculations are collected in Table 3.3. Our calculated values of formation energies of neutral defects in PbS are higher than those from Walsh[89] by 0.67 eV and 0.72 eV for V_{Pb}, V_S, respectively. The formation energy of the Schottky defect can not be compared since we do not know whether a Schottky dimer or a Schottky pair was studied in Ref. 89. The systematic

Table 3.3: Defect formation energy (eV/defect) of the intrinstic defects selected in this study.

PbX	V_{Pb}		V_X		I_{Pb}		I_X	
	This work	Lit.	This work	Lit.	This work	Lit.	This work	Lit.
PbO	1.54	—	2.04	—	—	—	—	—
PbS	1.78	1.36[89]	2.08	1.77[89]	2.41	—	2.91	—
PbSe	1.83	—	2.15	—	2.03	—	2.65	—
PbTe	1.90	2.19[88]	2.13	2.14[88]	2.20	—	2.76	—

PbX	Schottky dimer		Schottky pair		Frenkel Pb		Frenkel X	
	This work	Lit.	This work	Lit.	This work	Lit.	This work	Lit.
PbS	1.27	—	1.77	2.08[88]	2.87	—	4.19	—
PbSe	1.29	1.47[114]	1.75	—	2.63	—	4.32	—
PbTe	1.21	—	1.68	—	2.27	—	4.58	—

discrepancy in defect formation energies may originate from the fact that the supercells were not fully relaxed, and due to the larger supercell size (512 atoms), and less k-point (Γ only) used in Ref. 89. Hoang *et al.*[88] calculated E^f of V_{Pb} and V_{Te} for PbTe using DFT-GGA, $2a_0 \times 2a_0 \times 2a_0$ supercells, and cut-off energy of 300 eV. Their reported values are 2.187 eV and 2.135 eV for V_{Pb} and V_{Te}, separately. These values are very close to our results of 1.896 eV (ΔE =0.291 eV) for V_{Pb} and 2.129 eV (ΔE =0.006 eV) for V_X. Chai *et al.* reported the Schottky dimer formation energy of PbSe to be 1.47 eV. They used a smaller supercell of $2a_0 \times 2a_0 \times 2a_0$, and 450 eV of cut-off energy. The difference between 1.47 eV and our value of 1.29 eV is thus expected and is due to the different computational settings.

The defect formation energy is caused by a sum of effects, being mainly, 1) ionic size, 2) Coulomb interactions, 3) swelling or shrinkage of the lattice, and 4) the local relaxations around the defect site, which may all play a role in determining the magnitude of the formation energy of defects. These effects will be addressed in the following sections.

3.3.2 Local geometry relaxation

The comparison of the local relaxation around the defect site is listed in Tables 3.4 , 3.5 and 3.6. In order to describe the pictures more clearly, we call the NN Pb atoms of a X vacancy as $Pb^{NN(V_X)}$, and the NN X atoms of a Pb vacancy site as $X^{NN(V_{Pb})}$. For V_{Pb}, the $X^{NN(V_{Pb})}$ expand outward, but the extent of the expansion becomes smaller with increasing atomic size of the X atoms. For V_X, there is not a simple trend found; the $Pb^{NN(V_X)}$ may shrink inward or expand outward. In the study of V_{Pb} and V_{Te} in PbTe[88], it was found that the NN Te atoms around V_{Pb} expand by $\sim$ 0.024 Å, and the NN Pb atoms of V_{Te} relax inward by $\sim$ 0.07 Å.

The interstitial defects result in a large structural distortion to the crys-

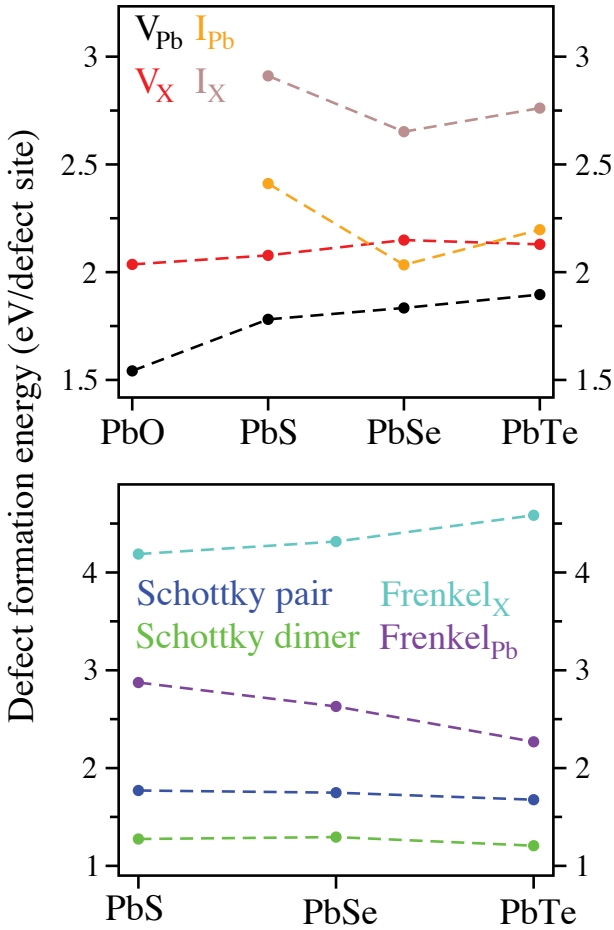

Figure 3.2: Formation energy of defects in PbX. Different defect types are labeled with different colors. Dotted lines are drawn to guide the eye.

tal, which may be the reason for the higher defect formation energy for interstitials.

For Schottky defects, both for the Schottky dimer and Schottky pair, the NN atoms of the cation and anion vacancy sites expand outward during relaxation. $Pb^{NN(V_X)}$ relax more outwards than $X^{NN(V_{Pb})}$. Along the direction of S→Se→Te, the degree of expansion is decreasing for the NNs of V_{Pb}, but increasing for the NNs of V_X. The reason for these trends is that the atomic size is growing along S→Se→Te (Table 3.8). With the larger atomic size, it is more difficult to displace the anion atoms, which results in the decreasing magnitude of expansion for $X^{NN(V_{Pb})}$. On the other hand, the expansion of the $Pb^{NN(V_X)}$ is a net result of the electrostatic interactions, which will be addressed in subsection 3.3.4. The $X^{NN(V_{Pb})}$ (ex-

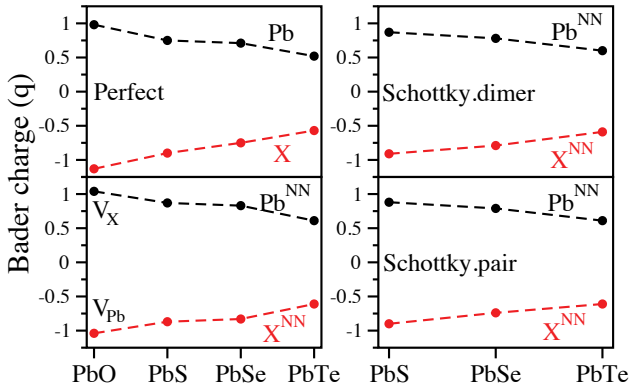

Figure 3.3: Bader charge of the defect sites. The black dots denote the results for the Pb atoms, and the red dots for the X atoms.

cept for PbS) and $Pb^{NN(V_X)}$ expand slightly more in Schottky pair than in Schottky dimer, which implies that the binding interaction within Schottky dimer attracts the NN atoms more. Here we discussed qualitatively how the relaxations affect atomic mobility. For a quantitative assessment, energy barriers would need to be calculated, which is beyond the scope of this work.

In Frenkel defects, all of the nearest neighbors of the defect sites underwent expansion. Especially at the interstitial sites, the huge expansion of their NN atoms could be the reason why the Frenkel defects are less stable.

3.3.3 Bader charge

The Bader charge for the NNs of each defect site is presented in Table 3.7 and in Fig. 3.3. We also listed the ionic radius and electronegativity of the anions in Table 3.8. As the atomic number increases, the ionic radius of the chalcogen ions increases, and their electronegativity decreases. Thus, one can expect that the extent of the ionic characteristics in the Pb-X bonding will also decrease with O → S → Se → Te, resulting in less charge transfer. This is clearly seen in Fig. 3.3. For both defect-free and defective PbX systems, the Bader charge of both Pb and X atoms decreases with O → S → Se → Te. It is noteworthy that the charge on either the cation or the anion is not greater than 1 *e*, which matches the previously calculated value of 0.85 *e* for Pb and -0.85 *e* for S in bulk PbS.[115] This suggests that the classical ionic model of $Pb^{2+}X^{2-}$ can be applied to PbX only for qualitative approximation, and the bonding within these systems is covalent in nature.[116]

Table 3.4: Relative displacement of the nearest neighbors of vacancy and interstitial sites. d_i denotes the initial distance, where d_{Pb-X} is the distance between Pb and the nearest X atom, and $d_{Pb-X,int}$ is the distance between an interstitial atom and its nearest neighbor. d_f is the final Pb-X distance in relaxed supercells. Δr is the distance displacement defined as $\Delta r = d_f - d_i$, and $\Delta r(\%)$ is Δr scaled with respect to d_i. The unit of length is Å.

	d_i		V_{Pb}			V_X			I_{Pb}			I_X		
	$d_{Pb\text{-}X}$	$d_{Pb\text{-}X,\,int}$	d_f	Δr	$\Delta r(\%)$	d_f	Δr	$\Delta r(\%)$	d_f	Δr	$\Delta r(\%)$	d_f	Δr	$\Delta r(\%)$
PbO	2.618	–	2.787	0.169	6.46	2.680	0.062	2.37	–	–	–	–	–	–
PbS	2.997	2.595	3.078	0.081	2.70	2.963	-0.034	-1.13	2.855	0.260	10.02	2.759	0.164	6.32
PbSe	3.103	2.668	3.156	0.053	1.71	3.155	0.052	1.68	2.948	0.280	10.49	2.946	0.278	10.42
PbTe	3.280	2.841	3.285	0.005	0.15	3.150	-0.130	-3.96	3.130	0.289	10.17	3.134	0.293	10.31

Table 3.5: Relative displacement of the nearest neighbors of Schottky defect sites

	d_i	Schottky dimer						Schottky pair					
	$d_{Pb\text{-}X}$	V_{Pb}			V_X			V_{Pb}			V_X		
		d_f	Δr	$\Delta r(\%)$	d_f	Δr	$\Delta r(\%)$	d_f	Δr	$\Delta r(\%)$	d_f	Δr	$\Delta r(\%)$
PbS	2.997	3.091	0.094	3.14	3.142	0.145	4.84	3.072	0.075	2.52	3.158	0.161	5.37
PbSe	3.103	3.153	0.050	1.61	3.273	0.170	5.48	3.156	0.053	1.71	3.313	0.210	6.77
PbTe	3.280	3.283	0.003	0.09	3.483	0.203	6.19	3.300	0.020	0.61	3.508	0.228	6.95

Table 3.6: Relative displacement of the nearest neighbors of Frenkel defect sites

	d_i		Frenkel$_{Pb}$						Frenkel$_X$					
			V_{Pb}			I_{Pb}			V_X			I_X		
	$d_{Pb\text{-}X}$	$d_{Pb\text{-}X,\,int}$	d_f	Δr	$\Delta r(\%)$	d_f	Δr	$\Delta r(\%)$	d_f	Δr	$\Delta r(\%)$	d_f	Δr	$\Delta r(\%)$
PbS	2.997	2.595	3.089	0.092	3.07	2.848	0.253	9.72	3.185	0.188	6.27	2.703	0.107	4.16
PbSe	3.103	2.668	3.163	0.060	1.93	2.941	0.273	10.23	3.308	0.205	6.61	2.852	0.184	6.90
PbTe	3.280	2.841	3.306	0.026	0.79	3.107	0.266	9.36	3.491	0.211	6.43	3.071	0.230	8.10

Table 3.7: Bader charge of the nearest neighboring (NN) atoms of vacancy, Schottky dimer and Schottky pair defects.

	perfect		V_{Pb}	V_X	Schottky dimer		Schottky pair	
	Pb	X	X^{NN}	Pb^{NN}	Pb^{NN}	X^{NN}	Pb^{NN}	X^{NN}
PbO	1.04	-1.04	-1.13	0.99	–	–	–	–
PbS	0.87	-0.87	-0.90	0.75	0.88	-0.91	0.88	-0.90
PbSe	0.83	-0.83	-0.73	0.71	0.78	-0.79	0.79	-0.74
PbTe	0.61	-0.61	-0.56	0.52	0.60	-0.59	0.58	-0.58

Table 3.8: Ionic radius r_{ion}, electronegativity χ and Bader charge (in perfect PbX supercell) of O, S, Se, and Te.

X	r_{ion} of X^{-2} (Å)[a]	χ (Pauling scale)	Bader charge (q)
O	1.26	3.44	-1.04
S	1.70	2.58	-0.87
Se	1.84	2.55	-0.83
Te	2.07	2.10	-0.61

[a] Ref. 117

3.3.4 Charge density difference at defects

The results for the charge density difference are shown in Fig. 3.4 as 2D intensity plots and in Fig. 3.5 as line profiles. We show only the V_{Pb}, V_X, and Schottky dimer defects in Fig. 3.4. The results of Schottky pair is included in Appendix A. In Fig. 3.4 (a)–(d), we also show $\Delta\rho$ for perfect PbX crystals obtained by Eq. 3.4. This is included for comparison with defective crystals.

V_{Pb} defects

Fig. 3.4 (e)–(h) show $\Delta\rho$ for V_{Pb} in PbX. After comparing with the perfect lattices, only the NN anions of the vacancy site have a clear change in $\Delta\rho$. This means that the perturbation of charge density introduced by the Pb vacancy inside the crystal is very localized. PbO behaves quite differently to the other PbX systems. The charge density is evenly distributed around the nucleus in an almost unperturbed way. This accumulation of charge density may be caused by the fact that the oxygen p orbitals are more tightly bound to the nuclei, so that the electron density is trapped at these orbitals.PbS, PbSe, and PbTe all exhibit similar $\Delta\rho$ patterns. In these three systems, the polarization of the electron density indicates that the NN anions possess two kinds of interactions: First, the NN anions mutually repel each other due to Coulomb interaction caused by the absence of the Pb atom at the vacant site. And second is the interaction with their

neighboring Pb cations: between the NN anions and their Pb neighbors, there is an accumulated charge density, and this charge density is polarized toward the Pb cations. The net results of these two interactions are the polarized charge density of the NN anions and the expanded relaxation of the Pb-X distance around V_{Pb}, as shown in Table 3.4. The extent of this polarization decreases with O → S → Se → Te, reflecting the fact that the ionicity of the chalcogen anions decreases along O → S → Se → Te.

V_X defects

The electron density is polarized in the case of V_X as well (Fig. 3.4 (i) –(l)). In the case of V_X, the NN Pb atoms relax toward the vacancy site (although the NN Pb atoms of V_X in PbO and PbSe shifted outwards from the vacancy site), accompanied by an asymmetric polarization of the NN Pb charge density toward the vacancy site. Even the NNN anion atoms donate some charge density to the vacancy center. This polarization results in a slight accumulation of charge density at the anion vacancy site, and resembles the notion of *electrides*. Electrides are crystals where electrons occupy anion vacant sites and act as anions.[118–121] In order to capture the accumulated electron density at the anion vacancy site, we also plotted the line profile for each V_X defect of PbX, as shown in Fig. 3.5. One can clearly see that, except for PbO, all the PbX have excess charge density at the anion vacancy site.

We also evaluated the amount of charge inside a sphere at the vacancy site. The chosen radii and integrated charges are shown in Table 3.9. The radii of the spheres are defined by checking the charge density of Pb and X ions in perfect PbX systems: the charge density minimum between Pb and X ions are set as boundary of the two ionic radii. The integrated charges are 0.53 e for PbS, 0.37 e for PbSe, and 0.57 e for PbTe. These values prove qualitatively that charges are attracted toward the anion vacancy site upon the presence of the anion vacancy, generating an electride inside the lattice.

Table 3.9: Charges integrated inside a sphere located at the anion vacnacy defect site in PbX systems.

PbX	r_{Pb} (Å)	r_X (Å)	Charge (e)
PbS	1.39	1.60	0.53
PbSe	1.46	1.66	0.37
PbTe	1.48	1.79	0.57

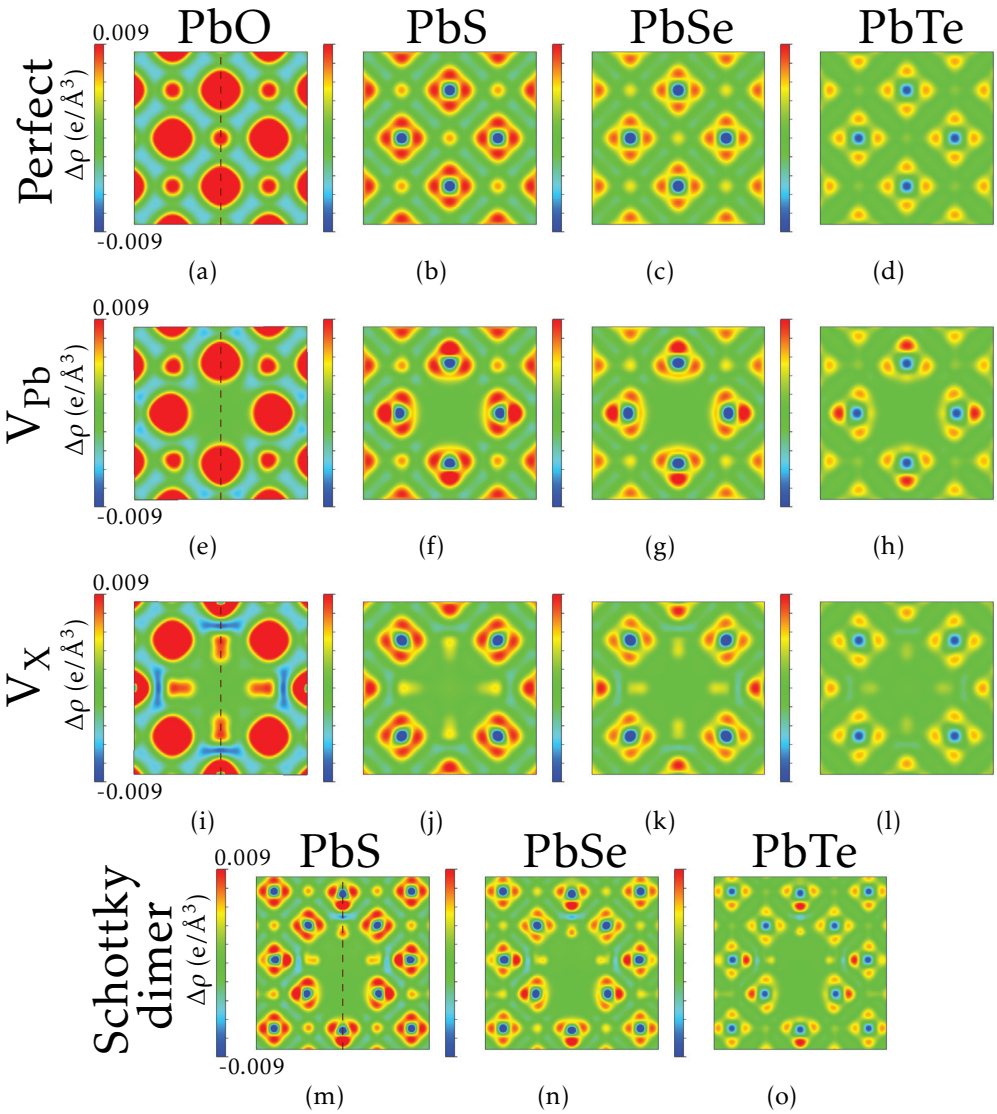

Figure 3.4: Charge density difference for perfect PbX systems, and PbX systems containing a V_{Pb}, V_X or a Schottky dimer. Color red denotes charge accumulation, and color blue for charge depletion. The cross-section is the (100) plane for perfect and V_{Pb}-containing systems, and is (001) for V_X containing systems. Dashed lines indicate the direction of the line profiles shown in Fig. 3.5

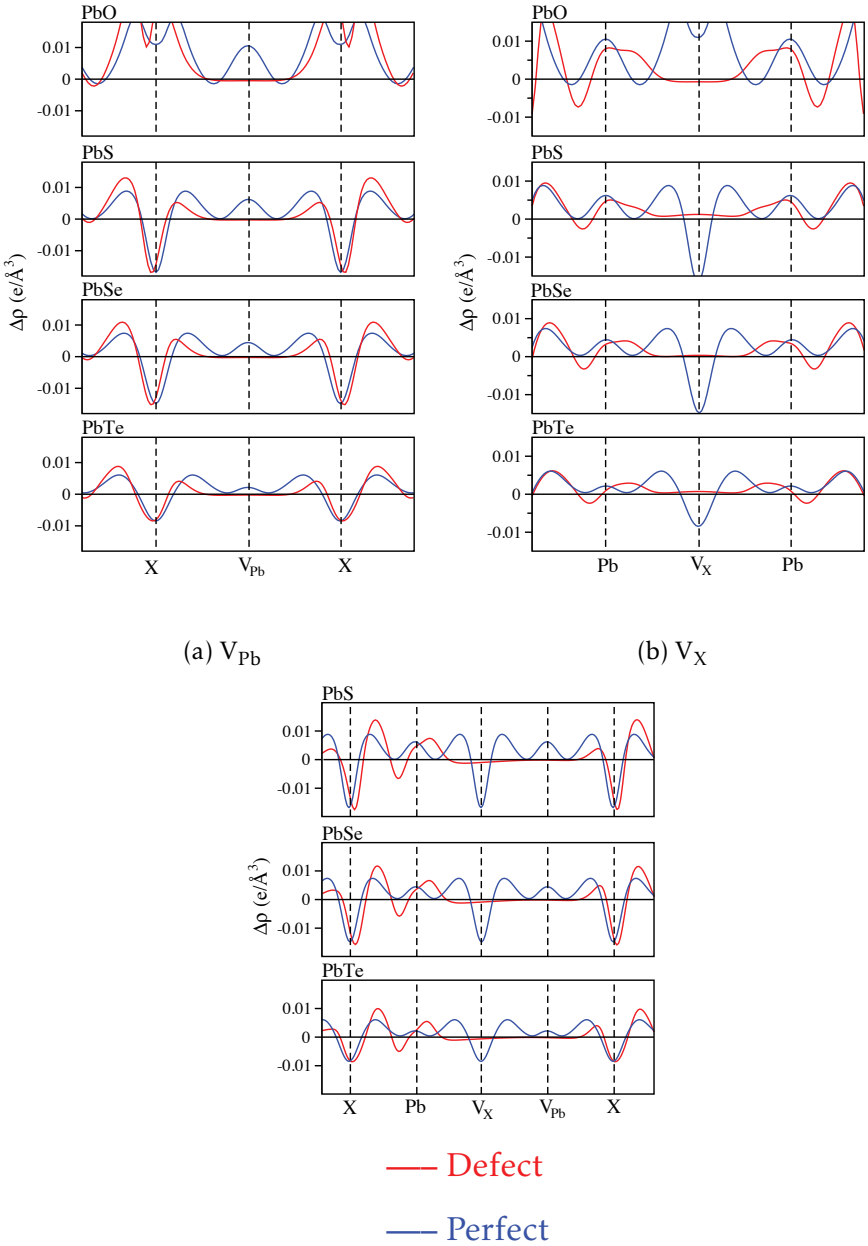

(a) V_{Pb}

(b) V_X

(c) Schottky dimer

Figure 3.5: Line profiles of $\Delta\rho$ for PbX systems containing a V_{Pb}, V_X or Schottky dimer. The lines are drawn along the dashed lines shown in Fig. 3.4 for different defect types.

Schottky dimer

The charge density difference of Schottky dimer is shown in Fig. 3.4 (m)–(o). The pattern of $\Delta\rho$ for V_{Pb} and V_X in the Schottky dimer is very similar to the case where they exist individually (*cf.* (e)–(l) of Fig. 3.4), however in this case the Pb atom is absent at the V_{Pb} site, therefore the charge density of its NN X atoms is more polarized towards the V_X site.

The charge density difference plots can also explain why the NN Pb atoms of the V_X site expand more along S → Se → Te in Schottky configurations, which is described in subsection 3.3.2. As shown in Fig. 3.4, the charge density of $Pb^{NN(V_X)}$ are polarized toward the V_X site as they do in the V_X case, but the extent of polarization decreases drastically along S → Se → Te. On the other hand, these $Pb^{NN(V_X)}$ also undergo an attraction from the neighboring X atoms through the polarized charge density between the two sides, and this attraction remains significant along S → Se → Te. Therefore, the net result is that the $Pb^{NN(V_X)}$ will be attracted more toward their neighboring X atoms along S → Se → Te.

3.3.5 Electronic structure

Band structure and density of states (DOS) calculations have been done for V_{Pb}, V_X, Schottky dimer and Schottky pair defect configurations, and the details are included in Appendix A. Since the smallest band gap occurs at the L point in the first Brillouin zone, we summarized all the positions of the defect states at the L point into Fig. 3.6. As one can see, along the direction of O → S → Se → Te, the V_X position shifts toward CBM, forming a deep defect state lying in the band gap. On the other hand, the V_{Pb} state generates a shallow state near the VBM margin, and the position of this state does not vary along O → S → Se → Te. For Schottky dimer (SD) and Schottky pair (SP) defects, we see that both the V_{Pb} and V_X states appear at the position similar to their single vacancy counterpart. But the V_X states do shift upward toward the CBM with decreasing inter-defect distance, *i.e.*, the distance of the V_X defect state to CBM is $V_X > SP > SD$. Therefore, the closer the two vacancy sites are, the closer the V_X state is to the CBM.

3.4 Discussions

3.4.1 Equilibrium defect concentration as a function of temperature

For the four kinds of stable defect chosen in this paper, we would give an estimate of their equilibrium concentration in bulk. The expression of free

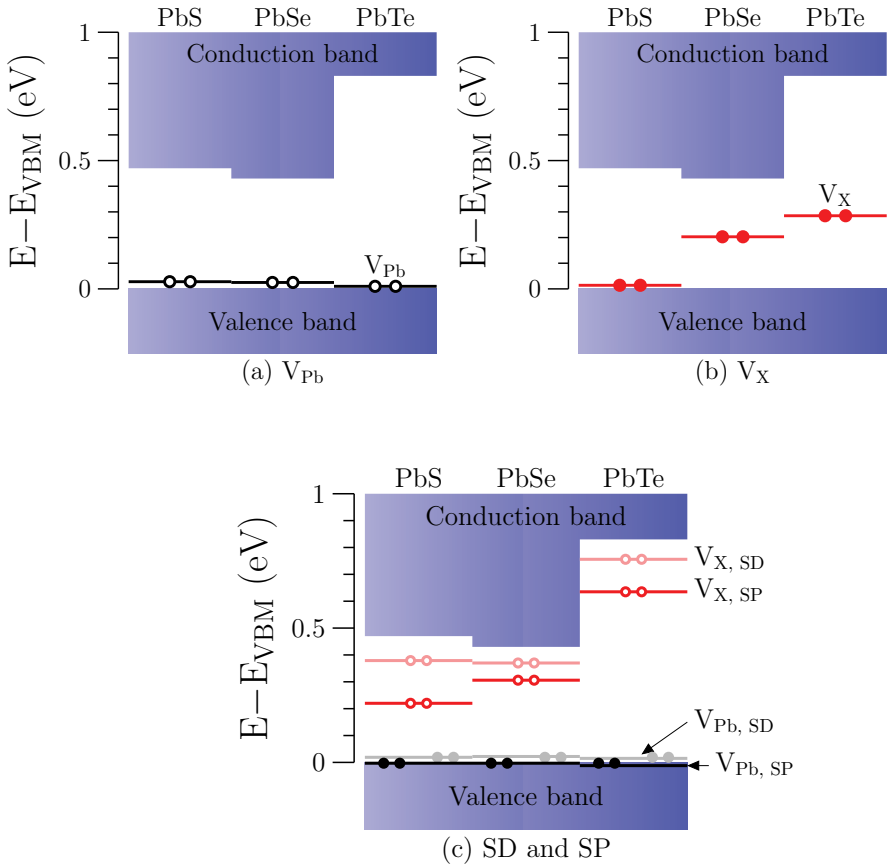

Figure 3.6: Schematic of the single-particle Kohn-Sham defect states of (a) V_{Pb}, (b) V_X, and (c) Schottky dimer (SD) and Schottky pair (SP) in PbX systems at the L point of the first Brillouin zone. Energy of VBM is set at zero energy.

energy per atom f in terms of the equilibrium defect concentration x_d can be used for this purpose: (the readers are referred to Appendix A and Ref. 122 for the derivation):

$$f = \frac{F}{n} = x_d E_f + k_B T[x_d \ln x_d + (1 - x_d)\ln(1 - x_d)], \tag{3.5}$$

where F is the total free energy of the system, n is the total number of atoms, k_B is the Boltzmann constant and T is the temperature in K. From the minimum of $f(x_d)$, we can determine the equilibrium defect concentration x_d at different temperatures. Temperatures of 298 K, 500 K, 750 K and 1000 K were selected, and the results are shown both in Fig. 3.7 and Table 3.10. At first glance, the temperature dependence of x_d can be clearly

seen, and the defect concentration increases with increasing temperature in an asymptotic manner. But overall speaking, the defect concentrations are very low: for PbS, for instance, the defect concentration at 500 K is 1.11×10^{-18} for V_{Pb}, 1.14×10^{-21} for V_S, 1.46×10^{-13} for the Schottky dimer, and 1.43×10^{-18} for the Schottky pair (here the defect concentration is expressed per Schottky pair, not per defect site). These low concentrations imply that in nanocrystals which contain only tens of thousands of atoms, there will be not a single defect present in the PbX nanocrystals. The defect formation energy might be different on surfaces and in the bulk. As indicated by Hoang *et al.*, E^f for V_{Pb} at surface is 0.181 eV lower than that in the bulk, and the formation energy for V_{Te} is lowered by 0.207 eV. In future work, it would be useful to calculate defect formation energies also for surfaces and interfaces, to obtain a more complete understanding of defect energetics in PbX crystals. In addition, compound nanocrystals are in general not stoichiometric[74,75], so that excess or depletion of one atomic species has to be accommodated either at the surface or in the interior of the nanocrystal.

The phase diagrams of PbX indicate that the stoichiometric configuration is very stable even at temperatures over 1000 K, implying that it is difficult for defects to be formed inside PbX lattices. This corresponds well to the low concentrations calculated here.

Table 3.10: Equilibrium concentration of V_{Pb}, V_X, Schottky dimer and Schottky pair defects in PbX systems predicted by Eq. A.4

	V_{Pb}			V_X		
	298 K	500 K	1000 K	298 K	500 K	1000 K
PbS	7.47×10^{-31}	1.11×10^{-18}	1.05×10^{-9}	7.24×10^{-36}	1.14×10^{-21}	3.37×10^{-11}
PbSe	9.74×10^{-32}	3.29×10^{-19}	5.74×10^{-10}	4.47×10^{-37}	2.17×10^{-22}	1.47×10^{-11}
PbTe	8.74×10^{-33}	7.82×10^{-20}	2.80×10^{-10}	9.79×10^{-37}	3.45×10^{-22}	1.86×10^{-11}

	Schottky dimer			Schottky pair		
	298 K	500 K	1000 K	298 K	500 K	1000 K
PbS	2.90×10^{-22}	1.46×10^{-13}	3.82×10^{-7}	1.14×10^{-30}	1.43×10^{-18}	1.20×10^{-9}
PbSe	1.30×10^{-22}	9.03×10^{-14}	3.00×10^{-7}	2.70×10^{-30}	2.38×10^{-18}	7.66×10^{-9}
PbTe	3.96×10^{-21}	6.92×10^{-13}	8.32×10^{-7}	4.49×10^{-29}	1.27×10^{-17}	3.57×10^{-9}

3.4.2 Coulomb model for Schottky defects

Since the inter-defect distance is a parameter that influences the physical properties in stoichiometric defects, we attempt to explain its effect by a simple Coulomb model. The Schottky configurations are chosen for this purpose because they are more stable than the Frenkel defect. We also took two more Schottky configurations named S2 and S3, with an inter-

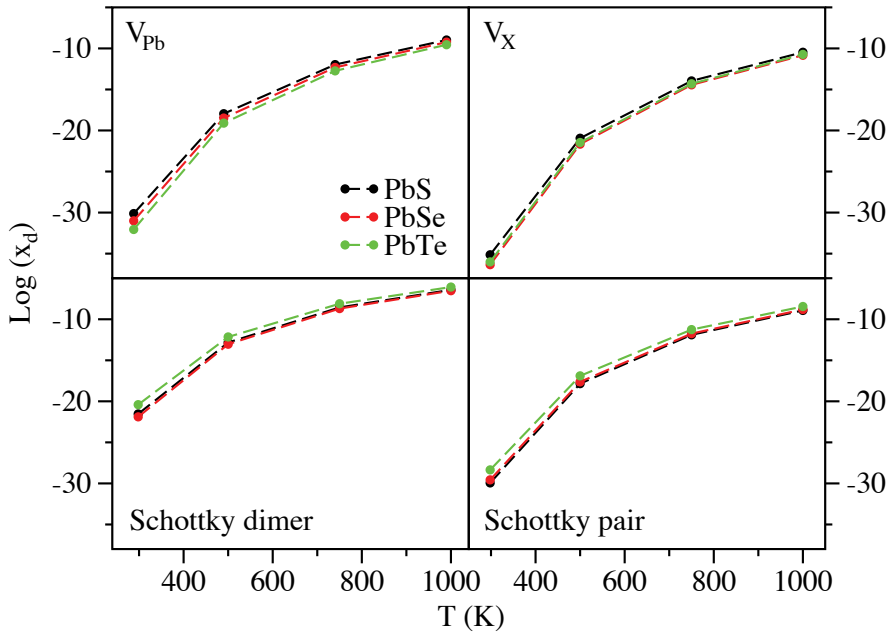

Figure 3.7: The equilibrium defect concentration x_d of the defective PbX systems at T =298 K, 500 K, 700 K and 1000 K. x_d is plotted on a logarithmic scale, and dashed lines are drawn to guide the eye.

vacancy distance between Schottky dimer and Schottky pair, and the V_X site located on or near the body diagonal of the supercell, to obtain enough data points. The relationship between defect formation energy and inter-vacancy distance for the four Schottky defects are shown in Fig. 3.8. It is clear that E^f converges apace with increasing inter-vacancy distance, which indicates that the interaction between V_{Pb} and V_X is short-ranged. The formula used to calculate the Coulomb potential is

$$U = \frac{1}{4\pi\epsilon_0\epsilon}\sum_j \frac{q_v q_j^{NN}}{r}. \tag{3.6}$$

This expression gives a Coulomb potential experienced by an vacancy site from its NNs , where $\frac{1}{4\pi\epsilon_0}$ is the Coulomb constant, ϵ is the dielectric constant of PbX systems (169, 204 and 414 at 300 K for PbS, PbSe, and PbTe, respectively[79]), q_v is the effective charge located on the V_X site, q_j^{NN} is the effective charge of the jth NN of the selected V_X, and r is the inter-defect distance in angstrom. The important parameter to be determined in Eq.

Table 3.11: Effective charge (q) of V_{Pb} and V_X in different Schottky configurations

PbX	Schottky dimer		Schottky.2		Schottky.3		Schottky pair	
	V_{Pb}	V_X	V_{Pb}	V_X	V_{Pb}	V_X	V_{Pb}	V_X
PbS	-0.74	0.71	-0.68	0.64	-0.74	0.84	-0.76	0.71
PbSe	-1.08	0.98	-1.60	1.32	-1.40	0.98	-1.46	0.95
PbTe	-0.82	0.60	-0.82	0.57	-0.85	0.67	-0.92	0.77

3.6 is the effective charges. The effective charge is defined as the charge difference on a certain atomic site before and after that atom is removed. For the effective charge located at the vacancy site, it is calculated by the following equation:

$$q_v = \Delta q_v - \sum_j \Delta q_j^{NN}, \tag{3.7}$$

with $\Delta q_v = q_{atom} - q_{vac}$ the charge difference at the vacancy site, and Δq_j^{NN} the charge difference of the NNs of the vacancy. Thus, the formula takes into account both the contributions from the vacancy site itself and its NNs. q_{atom} is the Bader charge of the atoms in perfect PbX systems, and q_{vac} is integrated within a sphere at the vacancy site using the radii determined in Table 3.9. The results of q_v are listed in Table 3.11. But the Coulomb potential calculated using these effective charges are really low (ranging from 0.015 eV to 0.004 eV for different Schottky configurations and PbX systems) in comparison to the differences in E^f (in the range of 0.5 to 1.0 eV). Therefore, variation in E^f as a function of separation cannot be explained by Coulomb models. Likely, lattice relaxation energies are dominating over electrostatic energies.

3.5 Conclusion

In this paper, we systematically studied the physical properties of a variety of defects in the PbX (X=S, Se, Te) systems by examining their defect formation energy, local geometry relaxation, charge transfer, and electronic structure. The studied defect types are vacancy, interstitial, Schottky dimer and Schottky pair, and Frenkel defect. We draw the following conclusions that are of importance for the physical properties of PbX NCs.

(i) Photoluminescence

The relationship between the PL of PbX systems and their point defects is shown in Fig. 3.6 for the three most stable types of defects; V_{Pb}, V_X, and Schottky defects. More details are included in Appendix A. The defect states of V_{Pb} are very shallow above the VBM with zero occupancy,

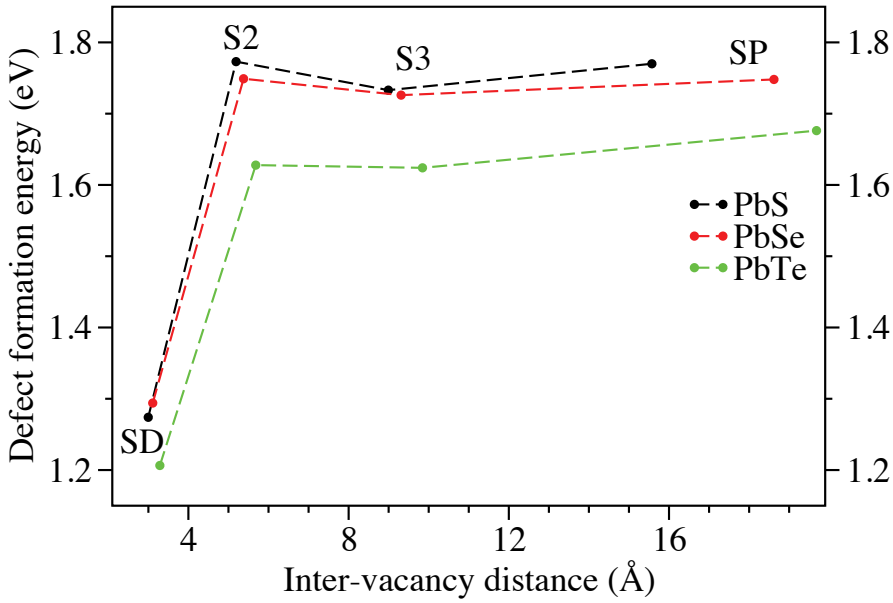

Figure 3.8: Defect formation energy versus inter-vacancy distance for the four different Schottky configurations. Dashed lines are drawn to guide the eye.

thus they are acceptor like and are likely to participate in a radiative recombination when these states are ocupied at finite temperature.[72] In contrast, the V_X defect states lie deeply in the band gap and are occupied by two electrons. Therefore, these states are expected to trap the conducting holes in *p*-type PbX material, and thus reduce the PL quantum yield.[72] For the Schottky defects SP and SD, the constituent V_{Pb} and V_X form donor-acceptor pairs (DAP), wherein the electrons (holes) originally residing at the V_X (V_{Pb}) states are transferred to the V_{Pb} (V_X) states. These DAP's will act as the recombination center for the excited electrons and holes, and give rise to a PL emission with energy smaller than that of the material band gap[123]. It is noteworthy that the PL emission energy is related to the distance between V_{Pb} and V_X pair; larger inter-vacancy distance will result PL peaks with smaller energy. Although in the present study we only consider point defects in bulk, defects at surfaces, interfaces and defects therein may also play a role in the recombination process of PL in PbX[124,125].

(ii) Off-stoichiometry

We have also investigated the energetics of off-stoichiometry for PbX bulk crystals. Table 3.3 indicates that the formation energy of V_{Pb} is smaller than V_X for all PbX systems, so an excess of anions is more easily accomodated than an excess of cations. Interstitials are unfavorable for both species. However, the defect energies are all quite high, so that off-stoichiometry is unfavorable. Phase separation may be hampered by nucleation barrier for the formation of pure Pb and X phases. For the case of NCs, part of the off-stoichiometry can be accomodated at the surface, also depending on the type of ligands used[74,75]. The effects would be interesting to investigate in future studies.

(iii) Cation exchange

Considering all the defect formation energies, Schottky defects, SP and SD, are significantly lower in formation energy than the cation and anion vacancies. Therefore, it becomes clear that Schottky defects may play a much more important role in the CE process than is currently presumed. This surprising result should be investigated into more detail in future studies, such as DFT simulations on migration energies, and MD simulations of CE.

(iv) Local geometry relaxation and charge distribution at defects

Because of huge displacements of NN atoms around interstitial-type defects, anion and cation interstitial defects and Frenkel defects are less favored. The result of local relaxations showed that the expansion or contraction of the NNs of a defect site is a net result of the electrostatic interaction among the atoms in that local environment. Bader charge analysis revealed that the degree of charge transfer decreases with O → S → Se → Te, in accordance with the trend of their electronegativity. Charge density difference plots indicated that charge density is locally polarized around the defect site, and electride type behavior with trapped charge is found at the anion vacancy site. In summary, we see a rich variety of physical properties introduced by defects in the PbX semiconductor family, with direct implications for synthesis and performance of PbX-containing HNCs.

In future work, this study could be extended to charged defects, and to the calculation of energy barriers for migration of vacancy-type defects.

Chapter 4

Spin-orbit splitting of point defect states in monolayer WS_2

*The content of this chapter was published in Phys. Rev. B **94**, 195425 (2016).*

The spin-orbit coupling (SOC) effect has been known to be profound in monolayer pristine transition metal dichalcogenides (TMDs). Here we show that point defects, which are omnipresent in the TMD membranes, exhibit even stronger SOC effects and change the physics of the host materials drastically. In this article we chose the representative monolayer WS_2 slabs from the TMD family together with seven typical types of point defects including monovacancies, interstitials, and antisites. We calculated the formation energies of these defects, and studied the effect of spin-orbit coupling (SOC) on the corresponding defect states. We found that the S monovacancy (V_S) and S interstitial (adatom) have the lowest formation energies. In the case of V_S and both of the W_S and W_{S2} antisites, the defect states exhibit strong splitting up to 296 meV when SOC is considered. Depending on the relative position of the defect state with respect to the conduction band minimum (CBM), the hybrid functional HSE will either increase the splitting by up to 60 meV (far from CBM), or decrease the splitting by up to 57 meV (close to CBM). Furthermore, we found that both the W_S and W_{S2} antisites possess a magnetic moment of 2 μ_B localized at the antisite W atom and the neighboring W atoms. The dependence of SOC on the orientation of the magnetic moment for the W_S and W_{S2} antisites is discussed. All these findings provide insights in the defect behavior under SOC and point to possibilities for spintronics applications for TMDs.

4.1 Introduction

The transition metal dichalcogenides (TMDs) are a member of the layered 2D van der Waals (vdW) materials, in which the atoms are bound by intra-layer chemical bonding and inter-layer vdW bonding. Among many other TMDs, the molybdenum dichalcogenides and tungsten dichalcogenides (MX_2, M=Mo or W, and X= S, Se, or Te) are the group 6 branch of the whole TMD family and have attracted much scientific attention. Theoretically, the most stable structure of MX_2 consists of one layer of transition metal atoms sandwiched by two layers of chalcogen atoms with a prismatic coordination, forming the so-called 1H form[27]. Due to the weak inter-layer vdW interaction, TMDs can be exfoliated from bulk into the few-layer or monolayer (ML) forms. When reducing the number of layers from bulk to ML, the band gap of TMDs evolves from an indirect band gap to a direct band gap with an increased gap size due to quantum confinement[28,29]. The layer-dependent tunability of the electronic structure together with other distinct physical properties of ML TMDs make them promising candidates of applications in fields like electronics, optoelectronics, spintronics and valleytronics, sensing, and catalysis[30–33].

There are two effects governing the band structure (BS) of MX_2, namely crystal field (CF) splitting and spin-orbit (SO) splitting (Δ_{SO}). These two effects strongly affect the electronic properties of MX_2 and influence in particular the d bands of the transition metal.

According to crystal field theory, the five formerly degenerate d bands of the transition metal will split in energy if the transition metal is bonded to other ligands (the chalcogen atoms in our case), and the pattern of the energy splitting is dependent on the metal-ligand coordination geometries. For ML MX_2 in the 1H phase, the transition metal is surrounded by six chalcogen atoms in a trigonal prismatic coordination (Fig. 4.1). Consequently, the d bands split according to their orientations — the more they are along the direction of the M-X bond, the higher in energy they will be due to the electron-electron repulsion with the X orbitals. As shown in Fig. 4.1, the d_{z^2} orbital is the lowest in energy, and the $d_{x^2-y^2}$ and d_{xy} orbitals are higher in energy. The d_{xz} and d_{yz} orbitals are the highest in energy[126,127]. In Appendix B* the decomposed band structures are shown for both bulk and ML WS_2 which illustrate the CF splitting of the d bands (Figures S3 and S4). The order of increasing energy is $d_{z^2} < d_{x^2-y^2} = d_{xy} < d_{xz} = d_{yz}$ for both bulk and ML WS_2, as expected.

The spin-orbit coupling (SOC) effect has been discovered for bulk

*See Appendix B for the limitation of vdW and SOC in the VASP code, density of states plots for all the ML WS_2 slabs, orbital decomposed charge densities of the band structures of perfect bulk and ML WS_2 unit cells, and orbital decomposed band structures of perfect and defective ML WS_2 supercells.

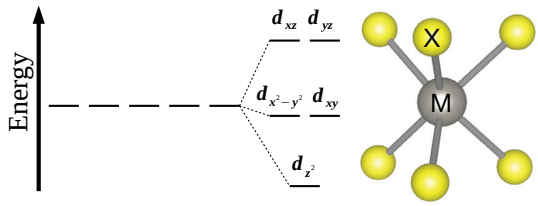

Figure 4.1: (Color Online) Schematic of the energy splitting of the transition metal d bands under the crystal field. The coordination is trigonal prismatic.

MX_2 materials in the last few decades[128,129], and for ML MX_2 in recent years[130–133]. In bulk MX_2, the system possesses both the space inversion symmetry ($E_\downarrow(\vec{k}) = E_\downarrow(-\vec{k})$) and time inversion symmetry ($E_\downarrow(\vec{k}) = E_\uparrow(-\vec{k})$). The net result is spin degeneracy in reciprocal space when no external magnetic field is present: $E_\downarrow(\vec{k}) = E_\uparrow(\vec{k})$. However, in the case of ML MX_2, because of the lack of space inversion symmetry, the spin states are expected to split under SOC. Especially, the band splitting can be as large as 463 meV for the valence band maximum (VBM) of ML WSe_2 at the K point in the first Brillouin zone[133]. For pristine ML WS_2, the band splitting is also large at 433 meV[133]. Based on symmetry arguments[130,133], for ML MX_2 only the orbitals with magnetic quantum number $m_l \neq 0$ will participate SO splitting. Furthermore, because the X atoms are rather light, their p orbitals are not affected by the SOC effect. Lastly, as indicated in the BSs of ML WS_2 in Appendix B (Fig. S4), the VBM and conduction band minimum (CBM) are dominated by the d_{z^2} ($m_l = 0$), d_{xy} ($m_l = -2$) and $d_{x^2-y^2}$ ($m_l = 2$) orbitals. As a result, only the d_{xy} and $d_{x^2-y^2}$ orbitals will have the SO splitting.

Besides the novel physical properties of pristine TMDs, atomic point defects are omnipresent in the materials. Furthermore, adatom adsorption and doping on ML MX_2 is especially achievable by virtue of their 2D surface nature. Both the naturally occurring and chemically or physically introduced point defects in MX_2 will extensively modulate the physical properties such as charge transport, magnetism, optical absorption, and absorbability[38,39,94,134–147], thus control the applicability of the material. The crucial role of point defects has triggered many studies to investigate their behavior in ML MX_2. Liu *et al.* identified the atomic defects and visualized their migrations on ML MoS_2[148]. Komsa *et al.* found that electron beam irradiation generates sulfur monovacancies (V_S) and also cause these defects to migrate and aggregate[37,149]. Zhou and *et al.* carried out a joint experiment and theory study and investigated several types of defects and their influence on the electronic structure of ML MoS_2 synthe-

sized by chemical-vapor-deposition (CVD)[150]. Among the single vacancy, vacancy complexes and antisite complexes, they found that the V_S is the predominant point defect. First principles calculations confirmed that V_S has the lowest formation energy among all the defect kinds. Hong *et al.* performed a systematic study which shows the route-dependency of predominant point defect types[9]. In ML MoS_2 synthesized by CVD and mechanical exfoliation (ME), V_S is the only dominating point defect, whereas in ML MoS_2 fabricated by physical vapor deposition (PVD), the antisites Mo_{S2} and Mo_S are the dominant point defects. They also found that the Mo_S antisite possesses a local magnetic moment around the Mo defect site. From the theoretical perspective, several exhausive works have been done to study the point defects systematically by virtue of the density functional theory (DFT)[151–153]. Their results predict that in ML MX_2, the V_S and sulfur interstitial S_i have the lowest formation energy.

Despite the significance of SOC and point defects for ML MX_2 systems, to the best of our knowledge thus far no study has been conducted on the SOC effect on the electronic structure of defective ML MX_2. Therefore, here we investigate how the SOC effect will change the band structure (BS) of ML MX_2 when different types of point defects are present. We chose systematically three categories of point defects: monovacancies (V_S and V_W), interstitials (S_i and W_i), and antisites (S_W, W_S, and W_{S2}). For conciseness, the ML WS_2 slabs containing these defects are abbreviated as: V_S@WS_2, V_W@WS_2, S_i@WS_2, W_i@WS_2, S_W@WS_2, W_S@WS_2, and W_{S2}@WS_2, respectively. The relaxed structure of each point defect is shown in Figure 4.2. We chose WS_2 as a representative of the MX_2 family as the physical and chemical properties of all the MX_2 members are very similar, and thus the results of WS_2 are expected to be applicable to other MX_2 systems.

Defect-induced magnetic moments on 2D materials are important for spintronics applications as exemplified by graphene[154,155], phosphorene[156], and ML germanane[157]. The orientation of the magnetic moments can be tuned as a degree of freedom by gating, doping, or functionalization, making the host 2D materials candidates for high-Curie-temperature materials with diluted magnetism strongly desired for high magnetic information storage density[155]. As such, we were motivated to also study the magnetic moments found in W_S@WS_2 and W_{S2}@WS_2 in the context of spintronics applications of dilute magnetic moments.

After describing the computational settings, we will first discuss the formation energies of the selected defect species. We then chose V_S, S_i, W_S, and W_{S2} for further investigation of the SO defect state splitting. We found that SOC causes strong defect state splitting in the cases of V_S and W_{S2}, with the magnitude of the band splitting up to 194 meV for V_S and 167 meV for W_{S2}, respectively. In addition, we also found that both W_S and W_{S2} antisites possess a magnetic moment around the antisite W atom,

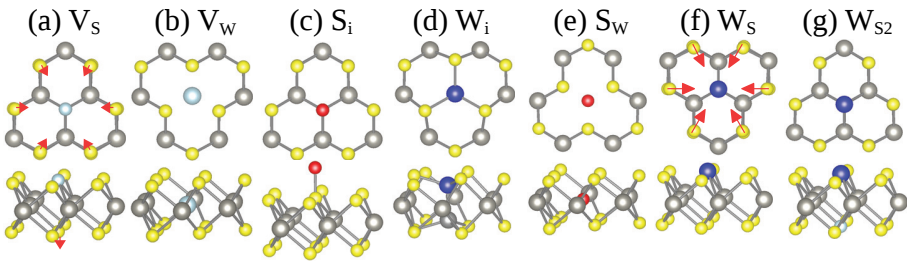

Figure 4.2: The relaxed structures of all the defective ML WS_2 supercells. The vacancies are denoted by light blue circles. The defect sulfur atoms are marked in red, and defect tungsten atoms in blue. The arrows indicate the directions and magnitudes of the relaxations.

which is contrary to the previous study of MoS_2[9]. The findings in this work provide a deeper insight in the point defect physics of MX_2 and will help developing potential applications of MX_2 in electronics and spintronics.

4.2 Computational details

All calculations were performed using the DFT code VASP[59–61] within the projector-augmented wave (PAW) framework[56]. The exchange and correlation energies were described using the generalized gradient approximation (GGA) formulated by Perdew, Burke, and Ernzerhof (PBE)[49,50]. We mention here that studying magnetism and spin-splitting in combination with SOC should ideally be treated on the basis of current density functional theory (CDFT)[158,159], where appropriate functionals are presently being developed[119,160]. The VASP code that was used in the present work treats the problem an approximate way, by incorporating relativistic effects by a scalar relativistic Hamiltonian with SOC in a perturbation treatment[161,162]. The GGA-PBE functional has been widely used for spin-splitting calculations, and it was shown that the magnitude of spin splitting in bulk WS_2 predicted by using the GGA-PBE functional matched perfectly with the result from experiment[163]. In addition, concerning the calculation of magnetic anisotropy energy (MAE), the results from GGA-PBE agreed well with the values calculated using the local density approximation (LDA) and with experimental values[162].

The cut-off energy of the wave functions and the augmentation functions were 400 eV and 550 eV, respectively. The van der Waals correction with the optB88-vdW density functional[164] was used as at the beginning of this study the bulk WS_2 was also included[†]. The supercell size of the

[†]Please refer to Appendix B for more details

ML WS_2 was 6×6 in the $x-y$ plane, and the vacuum along the z direction was larger than 16 Å. These dimensions of the supercell were sufficiently large to avoid the artificial defect-defect interaction. A Γ-centered $2\times2\times1$ k-mesh was used. The thresholds of energy convergence and force convergence were 10^{-4} eV and 10^{-2} eV/Å, respectively. We examined the SOC effect and found that it does not affect the structure but only influences the electronic properties of WS_2, therefore we only included SOC after geometry relaxation to obtain the band structure (BS) and DOS for the systems. We first performed the geometry relaxation and total energy calculation with only vdW correction included (without SOC). Then we turn on SOC, and exclude vdW correction for calculating the electronic properties (BS and DOS) of the relaxed geometry. Spin polarized (SP) calculations were performed for every point defect species, and only the W_S and W_{S2} antisites were found to be magnetic due to their unpaired electrons. The magnetism of W_S@WS_2 and W_{S2}@WS_2 was further investigated by non-collinear calculations.

The initial geometry of each point defect configuration was chosen based on previous theoretical studies[152,153]. The stringent setting described above guarantees a good convergence of defect formation energy within 0.01 eV.

In addition to standard DFT calculations, we also performed the more advanced hybrid functional (HSE06)[52] calculations for the defective ML WS_2 which shows defect state splitting under SOC (the V_S@WS_2, W_S@WS_2, and W_{S2}@WS_2). The goal of these HSE+SOC calculations is to investigate how HSE will affect the defect state splitting. The HSE calculations were performed on the DFT-relaxed geometries and we found that HSE relaxation gave almost identical geometries compared to traditional DFT. We set the fraction of Hartree-Fock exchange functional to 0.168 by fitting the calculated band gap of ML WS_2 to the experimental value. This fraction gives us a band gap of 2.04 eV, which is very close to the experimental value of 2.05 eV[165]. In the HSE+SOC calculations only the Γ point was included as we did a test for V_S@WS_2 and W_S@WS_2 and found that a $2\times2\times2$ k-mesh only improves the band gap for 7 meV for V_S@WS_2, and for 13 meV for W_S@WS_2. Therefore we believe that Γ is sufficient in our case. Our SO splitting of the top valence bands of perfect ML WS_2 calculated by DFT is 430 meV, which is perfectly matching the previous DFT-PBE result of 433 meV[133]. The HSE increases this splitting considerably to 517 meV.

Table 4.1: Formation energies (in eV) of the defects selected in this study

	W-rich	S-rich
V_S	1.689	2.897
V_W	6.345	3.928
S_i	2.419	1.211
W_i	5.317	7.733
S_W	8.219	4.594
W_S	5.380	9.005
W_{S2}	6.838	11.671

4.3 Results and discussion

Defect formation energy

The formation energy E_f of a neutral defect is defined as[166]

$$E_f = E_{defect} - E_{perfect} + \sum_i n_i \mu_i. \tag{4.1}$$

In Eq. 4.1, E_{defect} is the total energy of the defective system, $E_{perfect}$ is the total energy of the perfect system, n_i is the number of atoms being added (plus) or removed (minus) from the perfect system, and μ_i is the chemical potential of the added or removed atom. The added/removed atom is imagined to be taken from/put to an atomic reservoir, and the chemical potentials μ_i are needed to reflect the chemical environment surrounding the system. μ_i's are not fixed, but they are variables with the following boundaries[151–153,‡]:

$$E_{WS_2} - 2E_S \leq \mu_W \leq E_W \tag{4.2a}$$

$$\frac{1}{2}(E_{WS_2} - E_W) \leq \mu_S \leq E_S. \tag{4.2b}$$

The calculated defect formation energies are listed in Table 4.1 dependent on W-rich or S-rich chemical potentials.

The next step is to choose relevant defect types for further study of the effect of SOC on electronic properties of the defective ML WS_2 slabs. Table 4.1 provides a simple criterion in terms of defect formation energy: V_S and S_i possess the lowest formation energies in both the W-rich and S-rich conditions, thus it is sensible to select them for more detailed study. Although the W_S and W_{S2} antisites have a higher formation energy, it has been reported that the Mo_S and Mo_{S2} antisites are the predominant point defects in MoS_2 synthesized by physical vapor deposition (PVD). Therefore, the W_S and W_{S2} antisites are also included in the present study[9].

‡Please refer to Section 2.2.3 for the derivation.

Defect state splitings under SOC

As seen in Ref. 167 and Fig. S4 in Appendix B, the valence bands of MX_2 are composed of the p_x and p_y orbitals of the X atoms (here: S atoms), and the d_{xy}, $d_{x^2-y^2}$ and d_{z^2} orbitals of the M atoms (here: W atoms). The d_{xz}, d_{yz} orbitals are far from the band gap region. Furthermore, Fig. 4.4 (a) indicates that the top valence bands and the bottom conduction bands consist mainly of the d orbitals of W atoms. The only p orbital present is the p_z orbital from the S atoms, and it does not split under SOC. The calculated BSs with and without SOC are shown in Fig. 4.3. We can see from Figs. 4.3 and 4.4 – 4.6 that irrespective of the type of point defects, the VBM of WS_2 always splits into two bands under SOC.

V_S

As discussed in the Introduction, only the W d_{xy} and $d_{x^2-y^2}$ orbitals will undergo SO splitting. This is the case for V_S. The defect states are composed of the the linear combinations of W d_{xy} and $d_{x^2-y^2}$ orbitals, which are formerly degenerate are now split into two bands. The magnitude of the SO splitting for V_S is 194 meV. The HSE+SOC calculation gave a SO splitting of 252 meV, which is 58 meV larger than the DFT+SOC value. This substantial energy difference shows the necessity of hybrid functionals in calculating the SO splitting of the defect states.

S_i

In the case of S_i, the only defect state is composed of the p_x and p_y orbitals of the interstitial S atom, which do not split under SOC. This defect state is hidden in the top valence bands.

W_S

For W_S, the defect states are also composed of W d_{xy} and $d_{x^2-y^2}$, but they do not split when SOC is included in the calculations. Further eigenstate analysis shows that the reason for the defect states to be kept degenerate is that the spin projections of these states in the SOC BS are all on the m_x-m_y plane (m_x, m_y and m_z are the magnetization axes), in contrast to the defect states of the other three defect kinds where the spin projections are either mostly on along the m_z axis (in the case of W_{S2}, $+m_z$ for spin-up and $-m_z$ for spin-down). As a result, the spin states are not split even when SOC is present. We performed a second calculation in which the magnetization was constrained along the m_z axis and thus the defect states indeed split. This allows us to examine the effect of the orientation of magnetization on the defect state splitting. We also found that the m_z-constrained magnetic configuration is 38.9 meV higher in energy (for HSE, the value is 58.4 meV) than the m_x-m_y-relaxed magnetic ground state. This finding suggests that

the W_S@WS_2 is a magnetically anisotropic material and that the easy axis lies on the $m_x - m_y$ plane.

In Figs. 4.3 and 4.5 we show the BS and the band energies at Γ of the m_z-constrained W_S@WS_2. There are six defect states for W_S@WS_2 as shown in Fig. 4.5 (d). Three of these states are spin-up, and the other three are spin-down. For each spin species, the two degenerate states with a lower energy are composed of d_{xy} and $d_{x^2-y^2}$ of the antisite W atom, and the state higher in energy originates from the d_{z^2} orbital. It is worth mentioning that the spin-up d_{xy} and $d_{x^2-y^2}$ orbitals are occupied by two unpaired electrons which are the source of the magnetic moment of W_S@WS_2 as will be discussed in next section. Under SOC, the d_{xy} and $d_{x^2-y^2}$ orbitals split into two bands and each of these bands is a linear combination of d_{xy} and $d_{x^-y^2}$. For spin-up, this splitting is 296 meV, which is the highest Δ_{SO} among all the WS_2 defects studied in this paper. For spin-down, the splitting is 87 meV. The smaller Δ_{SO} for spin-down may be related to the fact that the spin-down defect states are much higher in energy than the spin-up states, thus they are closer to the CBM which are the d_{z^2} orbitals that do not exhibit SO splitting. The consequence is that the spin-down defect states are hybridized with the d_{z^2} conduction bands and thus their Δ_{SO} is reduced. This argument is supported by the wave function analysis, which shows that both the d_{xy} and $d_{x^2-y^2}$ orbitals approximately have a $\frac{1}{3}$ d_{z^2} character.

The Δ_{SO} from HSE+SOC are 356 meV and 62 meV for spin-up and spin-down, respectively. With HSE, the SO splitting of the spin-up defect states ubcreases significantly (60 meV) similar to the case of V_S@WS_2. However, for the spin-down defect states, with HSE the SO splitting decreases by 25 meV. The reason for the decreased Δ_{SO} for spin-down defect states is that HSE pushes these states further into the conduction band region, thereby enhancing the mixing with the d_{z^2} orbitals.

W_{S2}

W_{S2} is the most complicated case among the chosen defects. It involves ten defect states - five are spin-up and five are spin-down. As indicated in Fig. 4.6, without SOC, the five defect states for each spin type can be categorized into three groups: two groups of doubly degenerate states which are lower in energy, and a single d_{z^2} orbital higher in energy. The mixing of the conduction d_{z^2} band with the spin-down d_{xy} and $d_{x^2-y^2}$ defect bands is even worse in the case of W_{S2}@WS_2 as the spin-down defect d_{z^2} state is already in the conduction band region. The two sets of doubly degenerate states are composed of the linear combinations of the d_{xy} and $d_{x^2-y^2}$ orbitals of the antisite W atom, and will split into four states if SOC is present. Thus, for W_{S2}@WS_2, there are four sets of SO splittings. The Δ_{SO} of each split set is 121 meV, 105 meV, 167 meV, and 138 meV, respectively, with ascending energy.

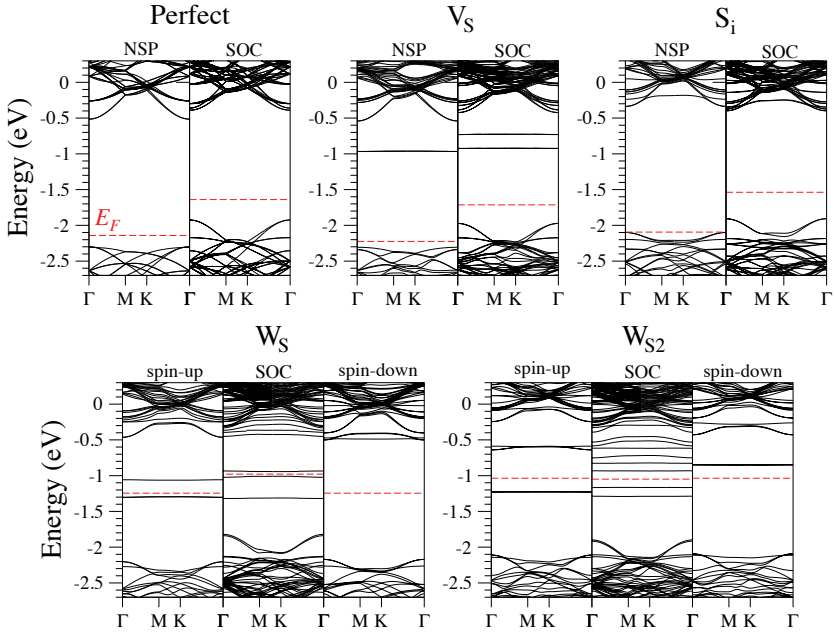

Figure 4.3: The band structures calculated with or without SOC for the selected WS_2 slabs. NSP stands for non-spin-polarized non-SOC calculations, and spin-up and spin-down stand for the spin-polarized calculations, respectively. Here the Fermi level is marked in red. The defect state splitting can be clearly seen in the case of V_S and WS_2. However, the splitting is supressed for S_i.

In contrast to the DFT case, the HSE calculation for W_{S2}@WS_2 relaxed the magnetization onto the $m_x - m_y$ plane. Therefore we again constrained the magnetization along the m_z axis. The constrained configuration is less stable than the relaxed one by 23.5 meV. For the magnetically constrained W_{S2}@WS_2, HSE again enhances the splittings which are not close to CBM (the first three splittings in Fig. 4.4 4.6). The increments are 46 meV, 38 meV, 33 meV, respectively. In contrast, for the fourth splitting HSE decreases Δ_{SO} by 57 meV. One noteworhty feature is that the spin-up splittings are always larger than the spin-down splittings.

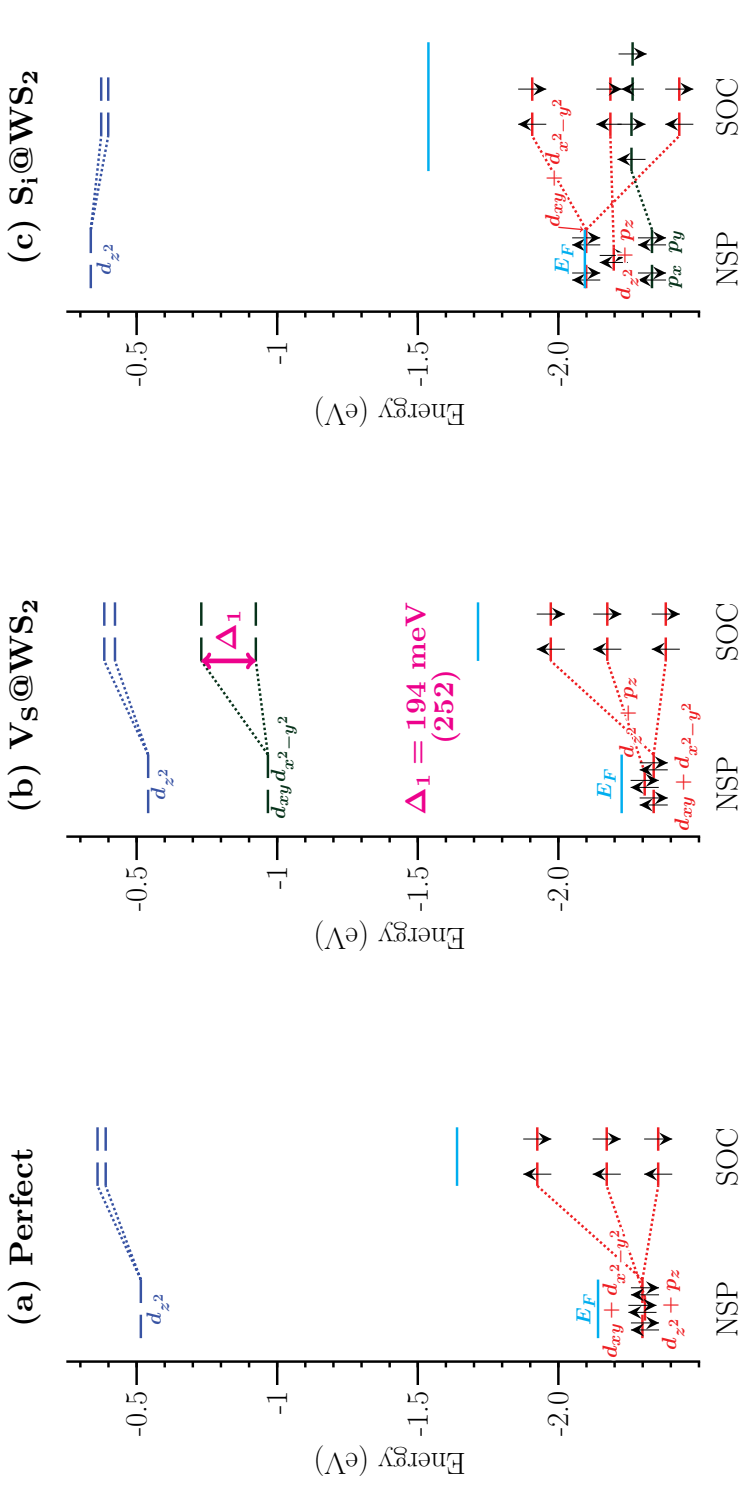

Figure 4.4: The energy level diagram of the WS_2 systems at the Γ point for the perfect WS_2 system (a), V_S@WS_2 (b) and S_i@WS_2 (c). The valence bands are colored in red, defect states in green, and conduction bands in blue. The Fermi level, E_F, is marked in cyan. The electrons which contribute to magnetism for W_S and W_{S2} antisites are labeled in light green. The major orbital components of each band are indicated, where the orbitals in bold are the most predominant ones. The dotted lines show the SO splittings of the energy bands. The amount of the SO splitting (Δ) is also shown in magenta, the values for Δin parentheses were calculated by HSE+SOC.

Magnetic moments of the W_S and W_{S2} antisites

We found that both W_S and W_{S2} defects possess a magnetic moment of 2 μ_B. This is different from the result of Ref. 9, which indicated that for MoS_2, only Mo_S-MoS_2 has a magnetic moment but not Mo_{S2}-MoS_2. These magnetic moments are generated by the unpaired spin-up electrons residing on the d_{xy} and $d_{x^2-y^2}$ defect states, as indicated by Figs. 4.5 and 4.6. These states split under SOC. We defined the spin density as the difference between the spin-up charge density and the spin-down charge density: $\rho = \rho_\uparrow - \rho_\downarrow$ to visualize the magnetic moment distribution around the defect site. The resulting spin density plots are presented for both antisite defects in Fig. 4.7. At first glance, the magnetic moment seems to be fully localized on the antisite W atom, however for both W_S and W_{S2}, the d orbitals of the neighboring W atoms contribute to the magnetic moment as well, and to a lesser extent also the next-nearest-neighboring (NNN) W atoms. are involved. For W_{S2}, the magnetic moment spreads to both the nearest-neighboring (NN) and NNN W atoms.

We compared the ratio between the magnetic moment at the defect W atom and the total magnetic moment ($\mu_r = \frac{\mu(W_{def})}{\mu(all)}$) to give a semi-quantitative description of the distribution of the magnetic moment. We used the VASP default atomic radii for W (1.455 Å) and S (1.164 Å) to perform the spherical integration of the spin density. We calculated μ_r using DFT (spin-polarized), DFT+SOC, and HSE+SOC methods. For W_S, μ_r(DFT)= 88.4%, μ_r(DFT+SOC)= 88.0%, and μ_r(HSE+SOC)= 98%, respectively. For W_{S2}, the corresponding values were lower at 53.1%, 53.5%, and 66.6%, respectively. In addition, we also found that the magnetic moment distribution shown in Fig. 4.7 has a triangular shape with a side length of around 6.4 Å in both cases. Therefore these two antisite defects could also be named magnetic 'superatoms'[9].

Therefore one can conclude that, first, for W_S the magnetic moment is almost solely localized on the defect W atom, yet for W_{S2} the magnetic moment is centered at the defect W atom, but half of it spreads to the NN and NNN W atoms. Second, with the HSE hybrid functional, the magnetic moment is more localized on the dedect atom, yielding a higher μ_r.

In order to trace back the origin of these magnetic moments, we compared the total energy and the density of states (DOS) of both the non-spin-polarized (NSP) and spin-polarized (SP) solutions of W_S@WS_2 and W_{S2}@WS_2. It was found that the NSP solutions are significantly higher in energy than the SP counterparts. The energy difference E(SP) - E(NSP) is 402 meV for W_S@WS_2 and 151 meV for W_{S2}@WS_2. Therefore both antisite configurations are indeed spin-polarized and are magnetic. The DOS plots of both the NSP and SP solutions for W_S@WS_2 and W_{S2}@WS_2 in Fig. 4.8 show clearly the magnetism. By combining Fig. 4.8, Figs. 4.4-4.6

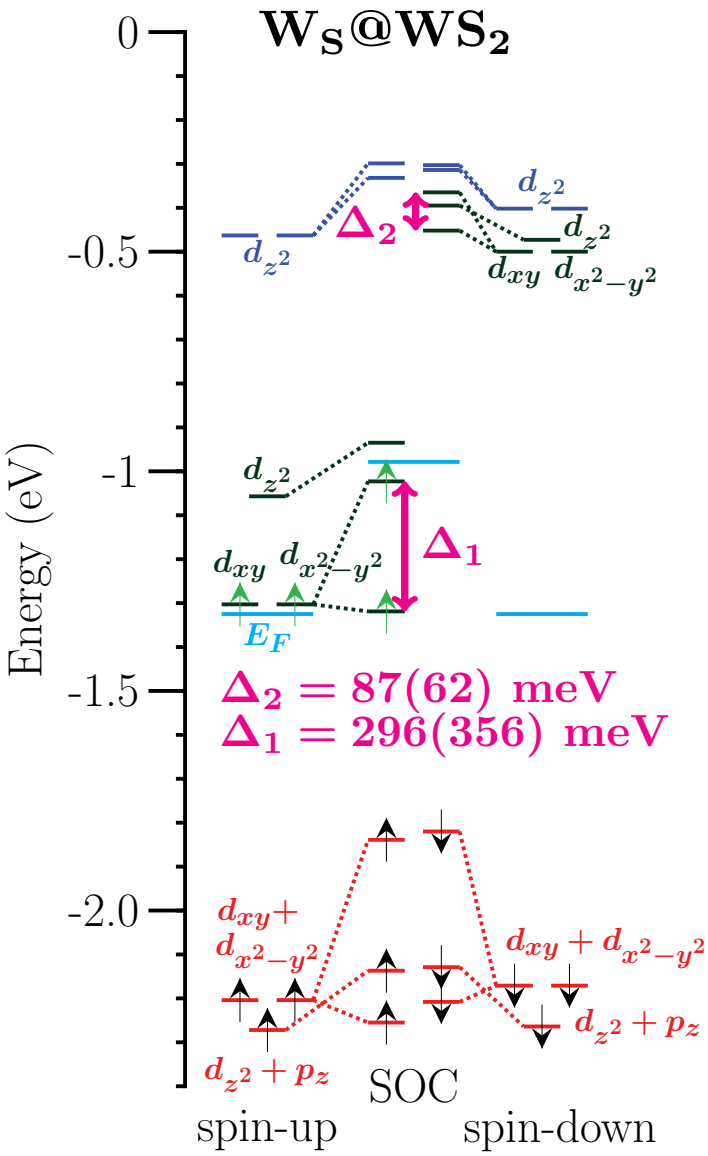

Figure 4.5: Energy level diagram of $W_S@WS_2$. See the caption of Fig. 4.4 for explanation of symbols.

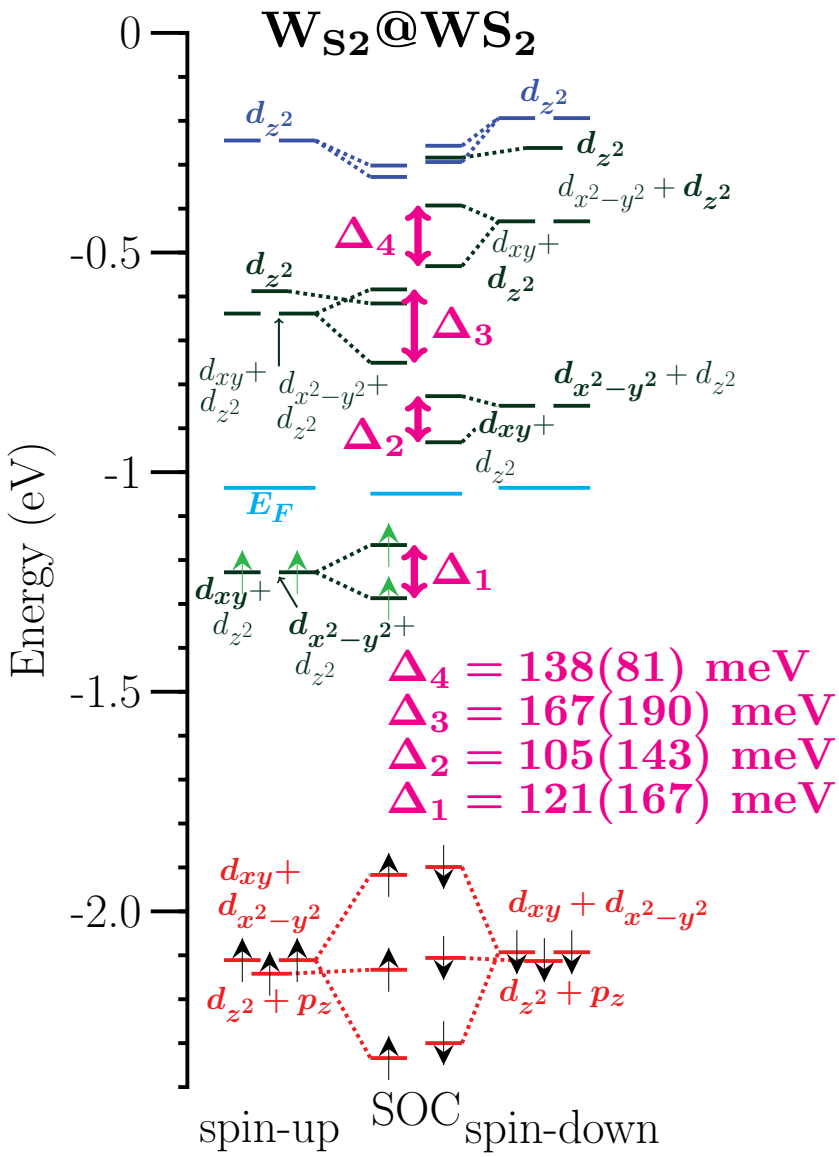

Figure 4.6: Energy level diagram of W_{S2}@WS_2. See the caption of Fig. 4.4 for explanation of symbols.

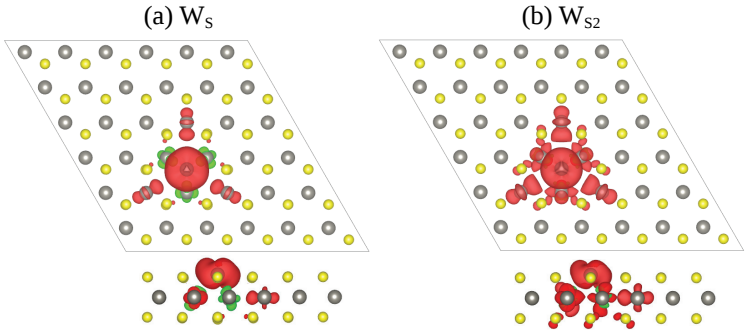

Figure 4.7: Spin density plots of (a) W_S and (b) W_{S2} antisites calculated by DFT. The spin-up charge density is marked in red and the spin-down density in green. The isosurface level is 0.002 $e/Å^3$.

and the projected DOSs (PDOSs) (Fig. S2 in Appendix B), we performed a thorough eigencharacter analysis of the defect states, revealing that these states are composed of the d orbitals of the antisite W atom which are numbered for each antisite in Fig. 4.8. For W_S@WS_2, group 1 is composed of the d_{xy} and $d_{x^2-y^2}$ orbitals and group 2 is characterized by the d_{z^2} orbital. For W_{S2}@WS_2 there are three groups of defect states. Group 1 and 2 are both composed of the d_{xy} and $d_{x^2-y^2}$ orbitals. However, they are now mixed with the d_{z^2} orbital to different extents. Group 2 is more heavily mixed with the d_{z^2} orbital than group 1. Group 3 is simply the d_{z^2} orbital. Furthermore, for both antisite defects, only the spin-up part of peak 1 is under the Fermi level and is occupied by two electrons from the d_{xy} and $d_{x^-y^2}$ orbitals of the antisite W atom. Therefore the magnetism and its origin is confirmed.

4.4 Conclusion

In this study we calculated the formation energies of seven different configurations of point defects including monovacancies, interstitials and antisites. We found that among the point defects, V_S and S_i possess the lowest formation energies; $E_f(V_S)$ =1.689 eV in a W-rich chemical environment, and $E_f(S_i)$ = 1.211 eV under a S-rich chemical environment. We selected the V_S, S_i, W_S and W_{S2} defects to investigate the SOC band splitting of the defect states. We have shown that the SO splitting depends on both the orbital constitution and the orientation of magnetization of the defect states. The states having the d_{xy} and $d_{x^2-y^2}$ character will undergo significant SO splitting when the magnetization is oriented along the m_z magnetization axis. The as-generated SO splittings are 194 meV for V_S,

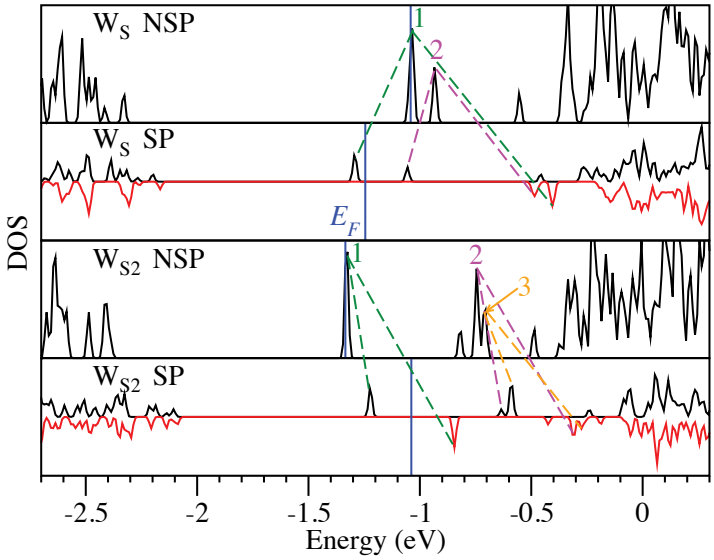

Figure 4.8: TDOS plots for both the non-spin-polarized (NSP) and spin-polarized (SP) W_S and W_{S2} antisites. The vertical blue solid lines indicate the Fermi level. The colored dotted lines map the NSP → SP splitting of the defect bands

296 meV and 87 meV for W_S, and 121 meV, 105 meV, 171 meV, and 138 meV for W_{S2}. The hybrid functional HSE enhances the SO splitting up to 60 meV if the defect state is not close to CBM. However, it decreases the SO splitting up to 57 meV if the defect state is close to CBM. For S_i no SO splitting was found as the defect state is composed solely by the d_{z^2} and p_z orbitals. We also found that not only W_S, but also the W_{S2} defect possesses a local magnetic moment of 2 μ_B around the antisite W atom due to the two unpaired spin-up electrons occupying the d_{xy} and $d_{x^2+y^2}$ defect states. The antisite W atom together with its NN and NNN W atoms thus form the so-called superatom.

4.5 Outlook

The results presented in this chapter provides insights into the SOC behavior of the ML WS_2 containing the most common point defects. These results are expected to be extendable to other ML MX_2 systems. In particular, the controllability of these SO split states are worth further investigation as they are highly promising in spintronics applications. It would be interesting to examine whether the spins can flip when an electric field is applied. Also, considering the frequent occurrence of the M_{X2} antisites

generated during the PVD synthesis of the ML MX_2 membranes[9], it will be interesting to increase the concentration of M_{X2} antisite defects and examine the interaction of the magnetic moments and their arrangement over space. Further development of this topic is beyond the scope of the present paper and will be addressed in future works.

4.6 Acknowledgements

This project is financially supported by the Dutch science foundation NWO via a VIDI grant (grant number 723.012.006). W.F. Li acknowledges Torbjörn Björkman and Hugo Aramberri for their discussion on the SOC calculations, and Jyh-Pin Chou for his practical instruction on VASP settings and insight of interpreting the SOC band structures.

Chapter 5

First principles exploration of the 2D monolayered transition metal oxides (TMOs; TM=Sc, Ti, V, Cr, Mn)

Transition metal oxides (TMOs) can exist in many polymorphs due to the electronic behaviour of their *d* electrons and the multivalence states of the TM atoms. However, in comparison to their 3D counterparts, which have been extensively studied for more than five decades, 2D monolayers of TMOs have been synthesized only in recent years and await further exploration.

In this context, we want to predict and study novel 2D TMOs by means of electronic density functional theory (DFT). We choose the early 3*d* TMs: Sc, Ti, V, Cr, and V. We consider four different 2D geometries in atomically flat monolayers, namely, hexagonal-MO (*h*-MO), rocksalt MO (*rs*-MO), cubic MO_2 (*c*-MO_2), and hexagonal M_2O_3 (*h*-M_2O_3). The different stoichiometries correspond to different valence states of the TM atoms. For these model systems, we calculate their (1) ground state geometry, (2) ground state magnetic ordering, (3) relative stability with respect to each other and to the elemental phases (bulk TM and oxygen molecule), (4) charge distribution by Bader analysis, and (5) electronic structure in terms of band structure. The magnetic arrangements considered in this study are non-magnetic (NM), ferromagnetic (FM), ferrimagnetic (FiM), and several antiferromagnetic (AFM) orderings. The hybrid functional approach is

also used to give a better description of the electronic and magnetic properties of these strongly correlated systems.

We have found that; (1) all these compounds are more stable than the elemental phases and may be realized experimentally with or without substrate, and (2) these 2D materials possess rich magnetic and electronic properties ranging from semiconducting, semi-metallic to half-metallic. This makes them suitable for applications in many fields such as electronics and spintronics.

Besides the perfect 2D TMOs, we have also studied the behavior of transition metal monovacancies (V_{TM}'s) in the most stable 2D TMO phase, h-M_2O_3. It was found that except V_{Sc}, all the V_{TM}'s possess a reasonably low formation energy in the O-poor condition, and may even stabilize the whole system in the O-rich condition as indicated by the negative formation energy. The V_{TM}'s will either create a magnetic moment around the vacant site(V_{Sc}@h-Sc_2O_3), or will significantly reduce the magnetic moments of the next-neighboring (NN) TM atoms.

5.1 Introduction

The research on 2D nanomaterials has been boosted up ever since the successful isolation of stable graphene nanosheets in 2004[168]. Graphene has been found to have many exceptional physical properties stemming from its unique geometry and electronic structure, making the material of great interest for both fundamental science technological applications ranging from electronics, optics, catalysis, biosensing, to sustainable energy. Inspired by graphene, scientists have started to synthesize and investigate other 2D materials consisting of elements other than carbon. Therefore, a wide spectrum of *beyond-graphene* 2D nanomaterials were soon discovered and extensively studied[169,170]. These materials include h-BN, monoelemental 2D semiconductors (silicene, phosphorene, and germanene), Mxenes (transition metal carbides, nitrides, or carbonitrides), and transition metal dichalcogenides (TMDs, such as MoS_2). In addition to the aforementioned branches of the family of 2D materials, 2D transition metal oxides (TMOs) have also been realized experimentally and are actively investigated. Before discussing the 2D TMOs, we would like to give a brief introduction of bulk TMOs, so that a connection between the 2D TMOs and bulk TMOs can be seen established more easily later in the discussion.

The bulk phase TMOs have been a fascinating yet challenging topic to both experimental and theoretical scientists for more than half a century. The uniqueness of TMOs is attributed to the d electrons of the transition metals (TMs). These TM d electrons experience a strong Coulomb repulsion from one another, thus the name *strongly correlated* electrons. This strong correlation leads to the unprecedented physical phenomenon

of the metal-insulator transition (MIT)[51,171], where, upon tuning parameters such as temperature, pressure or chemical composition, the electronic structure of the system will undergo a metal-insulator transition. However, because the transition involves the subtle interplay of the energy, geometry, electronic and magnetic properties of the TMOs, the MIT is often accompanied with a both structural and magnetic phase transition. One of many good examples of the MIT is vanadium monoxide (VO). VO is a non-magnetic (NM) insulator in the monoclinic structure (M1 phase) below the Curie temperature (T_C = 340 K), and becomes a paramagnetic (PM) metal in the rutile structure (R phase) when the temperature rises above T_C.[172] Furthermore, VO will undergo a secondary phase transition to another insulating monoclinic phase (M2) upon an applied strain.[173] A further complication is that the real ground state of VO at finite temperature is predicted by hybrid DFT calculations[172,174], and suggested by experiments[174], to be the ferromagnetic (FM) metallic M0 phase.

In addition to the MIT, electrons can either fully or partially occupy the TM d orbitals, giving multi-valence states to the TMs. Because the TMs can exist in different valence states, it can be coordinated with different number of oxygen nearest neighbors, forming different stable TMOs. For instance, with increasing valency, the vanadium oxides can exist in the following four principal phases VO (+1), V_2O_3 (+1.5), VO_2 (+2), V_2O_5 (+2.5). These structural and electronic degrees of freedom lead to more than ten intermediate phases with the general formula V_nO_{2n+1} ($1 \leq n \leq 3$, the Wadsley phases)[34], and V_nO_{2n-1} ($3 \leq n \leq 9$, the Magnéli phases).[35]

Besides MIT, TMOs of a certain stoichiometry may also exist in multiple stable phases, *i.e.*, Mn polymorphs. A good example thereof is, among many others, MnO_2. MnO has been found to exist in six phases, namely, the α (hollandite), β (pyrolusite), δ (layered), γ (intergrowth), λ (spinel), and R (ramsdellite) phases[36], and the transition between the layered δ phase and other 3D-interlinked phases with different tunnels (α, β, γ, R) can take place with an energy barrier as low as 0.2 to 0.3 eV.[175] All the diverse TMO phases make them versatile in a wide range of applications, including energy storage, molecular sieve, catalysis, functional magnetic and optical materials, and biosensors.

From the theoretical point of view, traditional density functional theory (DFT) fails to describe the localized d electrons in the strongly correlated TMOs. One famous failure is that DFT falsely predicted CoO to be metallic while it is actually an antiferromagnetic insulator[51]. It remains a challenge for band theories to correctly and consistently evaluate the relative stability of the TMO polymorphs, or to calculate the real structural and magnetic ground state of a certain TMO structure.

With the popularity of 2D materials and the unique properties of bulk TMOs in mind, it is intuitive to consider the possibility of 2D TMOs.

Comparing to the long history of intensive research on their bulk counterparts, the exploration on 2D TMOs has just started within a decade, and is rapidly progressing. Experimentally, the approaches of synthesizing 2D nanomaterials can be categorized into two groups: top-down and bottom-up[170]. The top-down approach essentially consists of the various exfoliation methods trying to isolate one layer, or few layers, of a material from the layered bulk structure. This approach is suitable for layered materials such as graphene, *h*-BN, or MoS_2, where the inter-layer interaction is the weak vdW force, making it feasible to exfoliate the material layer by layer. On the other hand, the bottom-up approach involves depositions of molecules on substrates. This approach is suitable for materials which do not have an equivalent bulk phase. *

There have been numerous experiments which successfully synthesized 2D TMOs thin films. An exhaustive review is beyond the scope of this study, and here we just name a few works which are directly related to our topic of investigation: the early 3*d* transition metals (Sc, Ti, V, Cr, Mn). Rutile TiO_2 thin films were prepared on the α-Al_2O_3 surface[139]. Makarevich *et al.* grew the epitaxial rutile and monoclinic VO_2 films on the *r*-Al_2O_3 surface via chemical vapor deposition[177]. In 2000, monolayered (ML) V_2O_3 thin films have been synthesized on the Pd(111) surface as substrate[178,179], and was later characterized by DFT simulation[97]. The structure was identified to be hexagonal (*cf*. Fig. 5.1 2b, the only difference is that the synthesized V_2O_3 is slightly buckled with the vertical V-O separation of 0.7 Å). The important finding therein is that metal substrate stabilizes thin films which have no equivalent bulk phases. Sun *et al.* developed a generalized approach to prepare 2D nanosheets of TiO_2, ZnO, Co_3O_4, and WO_3. The strategy was to use organic surfactants as templates, and help the nanosheet precursors to self-assemble into lamellar structures. The oligomers can be further crystalized into nanosheets and the surfactants can be removed in the end[157]. The as-synthesized TiO_2 nanosheet is 3.3 nm in theckness and contains 4-5 MLs of anatase TiO_2. Recently, Xiao *et al.* synthesized several 2D TMOs nanosheets, including cubic (*rs*) MnO, of 1 nm in thickness on temporary salt substrates[131].

On the computational side, both Ataca *et al.*[180] and Filip *et al.*[181] used DFT and more advanced methods including the quasiparticle *GW* approach to carry out a comprehensive study on TMDs and TMOs in the 1-T and 2-H structures. They found that for TMOs with TM= Sc, Ti, V, Cr, Mn, they are stable in both the 1-T and 2-H structures in terms of heat of formation. However, the single-atomically thin 2D structures were not considered in these two studies. ML MnO_2 nanosheet in the 1-H phase as MoS_2, was exfoliated from layered MnO_2 in 2003,[182] and was further

*To clarify the terminology, we use thin *film* for 2D materials grown on a substrate, and *nanosheet* for a substrate-free, free standing 2D layer.[176]

identified by DFT+U and HSE calculations to be an intrinsic ferromagnetic 2D material[183]. Nam *et al.* prepared bulk wurtzite (*wz*) MnO on a carbon template[184], and Kan *et al.* further predicted, by means of DFT+U, that the graphitic-like, hexagonal MnO layers (*cf*. Fig. 5.1 (a)) are more stable than the corresponding *wz*-MnO (0001) surface when the number of layers is less than 4[185]. Along this line, Wang *et al.* performed DFT calculations and suggested that WZ semiconductors can be transformed into the planar hexagonal structure upon a planar stretching force[186].

Despite the knowledge gained for bulk TMOs, and the successful synthesis and investigation of some 2D TMOs, to the best of our knowledge, hitherto a systematic and rational prediction of novel 2D structures of TMOs has not yet been conducted. Therefore we are stimulated to disclose the relative stability, novel electronic and magnetic properties of the 2D, single-atomic thick TMOs by DFT and hybrid functional calculations. We focus on the first five of the 3*d* transition metals: Sc, Ti, V, Cr, Mn. These five TMs are also grouped as the early transition metals. According to the different valence states of the TMs, we designed four different 2D TMOs, as shown in Fig. 5.1. They are hexagonal MO (*h*-MO, V=+1), rock-salt MO (*rs*-MO, V=+1), hexagonal M_2O_3 (*h*-M_2O_3), and cubic MO_2 (*c*-MO_2), respectively. For each structure, we also considered the possible collinear magnetic configurations, including non-magnetic (NM), ferromagnetic (FM), anti-ferromagnetic(AFM) , and ferrimagnetic (FiM) of the TMs, as shown in Fig. 5.2. We make the following remarks concerning these structures:

1. *h*-V_2O_3 has been experimentally realized on a substrate in a buckled form[97,178,179]; *h*-MnO has been predicted to be stable[185]. All other structures are at this moment undiscovered.

2. The 2D *h*-MO and the *rs*-MO phases have *wz*-MO and *rs*-MO as their equivalent bulk phase, respectively. However, there is no direct 2D-bulk connection for *h*-M_2O_3 and *c*-MO.

3. The *c*-MO structure is closely related to *rs*-MO; the TMs in *c*-MO have also four nearest neighboring (NN) oxygen atoms as they do in *rs*-MO. The only difference is that each oxygen atom has two less NN TM atoms compared to *rs*-MO.

The remaining content of this Chapter is organized as following: in Sec. 5.2, the theory used for simulation, the geometrical and magnetic models of the ML TMOs, and the definition of the formation energies will be given. In Sec. 5.3, the stability, geometry, and electronic and magnetic properties of these TMOs will be discussed in detail, together with the comparison of their 3D counterparts having the same stoichiometry. In addition, the properties of transition metal monovacancy (V_{TM}) in the most

stable 2D TMO phase, h-M_2O_3, will also be presented. The current findings are expected to advance the understanding of 2D TMOs and guide future synthesis of these novel 2D materials.

5.2 Computational Details

All calculations were performed using the DFT code VASP[59–61] within the Projector-Augmented Wave (PAW) framework[56]. The exchange and correlation energies were described using the Generalized Gradient Approximation (GGA) formulated by Perdew, Burke and Ernzerhof (PBE)[49,50]. The cut-off energy of the wave functions and the augmentation functions were 500 eV and 750 eV, respectively. For all the NM and FM phases and the h-M_2O_3 AFM phase, the unit cells containing the forming unit were used for all the four 2D TMOs. 2×2 supercells were employed for the h-MO AFM, rs-MO AFM1, c-MO_2 AFM1 and AFM2 phases to incorporate the magnetic orderings. Similarly, a 3×3 supercell was used for the h-MO FiM phase. For all the models, a vacuum space larger than 20 Åwas included to avoid spurious interaction between the slabs. A 16×16×1 Γ-centered k-mesh was used to sample the reciprocal space for the unit cells. The k-mesh of the supercells was modified in proportion to the change of the lattice size. The cut-off energy, k-mesh, and the size of the vacuum space were all tested to converge the total energy within the threshold of 1 meV/atom. For the magnetic models, initial magnetic moments of 4 μ_B and 0 μ_B were assigned to the TM and the oxygen atoms, respectively. To obtain the ground state geometries and magnetic arrangements, the lattice constants and atomic positions, as well as the magnetic moments were allowed to be relaxed. Only the cell volume was fixed to avoid collapsing the vacuum separation between the model slabs. The criteria for energy convergence and force convergence were 10^{-6} eV and 10^{-2} eV/Å, respectively.

In addition to standard DFT calculations, we also performed the more advanced hybrid functional (HSE06)[52] calculations on top of the PBE-relaxed structures, to obtain a more accurate description of the electronic structure of these strongly correlated 2D TMOs. The screen factor $\alpha = 0.25$ was set for all the HSE calculations, featuring a $\frac{1}{4} : \frac{3}{4}$ hybridization of the Hartree-Fock exchange energy and the PBE exchange energy. The enormous amount of calculation involved in this study prevented us from relaxing the structures also using the hybrid functional. However, it was found that the HSE functional gives very similar results for geometry relaxation and relative stability[36,130,187–190], indicating that the nonlocal HF exchange has less effect on the structure and total energy of a strongly correlated system, but mainly affects the electronic structure (the d states) of the system. In particular, HSE gives almost identical geometries as PBE does for 2D materials such as graphene[191] and MoS_2.[167,192] Therefore, the

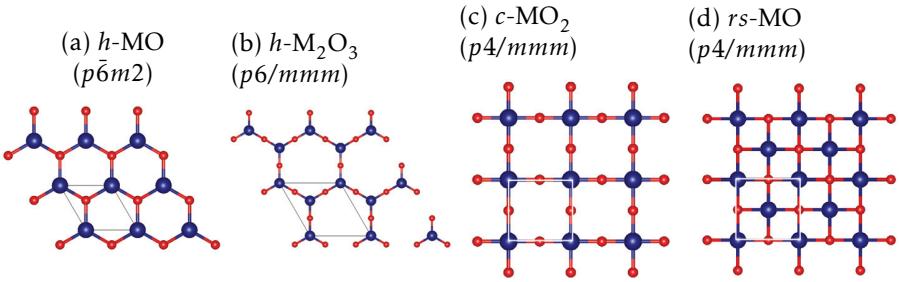

Figure 5.1: Models of the four types of 2D ML TMOs considered in this study. The TM atoms are marked in blue, and oxygen atoms in red. The white lines indicate the unit cell. The space group of each model is also given.

methodology of using HSE to calculate the electronic structure of a PBE-relaxed geometry is validated.

The popular DFT+U method was not considered in this study as we were treating a wide range of elements, and calculating various physical properties from energy, geometry, to electronic and magnetic properties. DFT+U, being intrinsically a theory depending on the Hubburd U parameter which differs for different elements and different properties, may lead to unwanted inconsistency in our results.[188] An obvious example is that DFT+U gave a deviation of lattice parameter for γ-$Fe_{23}C_6$ as large as 12%[193].

As mentioned in the Section 5.1, we have chosen four 2D geometries with different valence states for five transition metals to form the TMOs, and for each geometry, all the possible collinear magnetic configurations were taken into account. Here, the non-collinear magnetism (the spin-orbit coupling effect as well) was not considered because of limitations of computational power. It is worth noting that the FiM configuration for h-MO was the arrangement in which the total number of spin-up and spin-down electrons are not equal. The FiM configuration was included because it is the ground state magnetic ordering of half-hydrated graphene (graphone).[194]

5.3 Results and Discussion

5.3.1 Stability and Geometry

Relative stability among the 2D TMO phases

It is essential to confirm the stability of these 2D TMOs discussing their electronic and magnetic properties. We will first assess the relative sta-

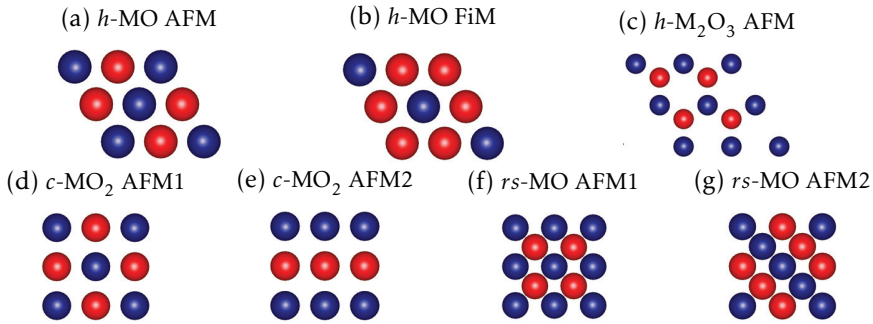

Figure 5.2: Magnetic orderings considered in this study for the four types of 2D ML TMOs. Only the TM atoms are shown for clarity. Different colors of the atoms denote for spin-up or spin-down magnetic moments.

bility among these 2D TMOs. For this purpose, we define their formation energy per atom with respect to the elemental transition metal bulk phases TM and the paramagnetic oxygen molecule O_2:

$$E_f = \frac{1}{1+x}[E(MO_x) - E(TM) - \frac{x}{2}E(O_2)], \tag{5.1}$$

where $E(MO_{1+x})$ is the calculated total energy of the TMOs with x=1, 1.5, or 2. $E(TM)$ is the energy per atom of the TMs in their elemental phase, and $E(O_2)$ is the energy of an O_2 molecule in its paramagnetic ground state.

The formation energies calculated using Eq. 5.1 are listed in Table 5.1. In addition, the energy of the most stable 2D TMO phases at their ground state magnetic configurations is plotted along the increasing stoichiometry in Figure 5.3 as the concave-hull plot. The important information being conveyed by concave-hull plots is that any point that lies below the straight line connecting two data points is stable; the system will be unstable and decomposed into the two nearest compositions if its energy lies above the connecting line[97]. Figure 5.3 indicates that although the h-M_2O_3 phase has the lowest formation energy per atom compared to other 2D TMO phases, the energy of every 2D phase is actually located below the straight line connecting the two adjacent energies on its both sides, suggesting that *all these 2D TMO phases are stable at the respective stoichiometries*. In Figure 5.3, it is also shown that except Mn, all the rs-MO phases are always more favorable over h-MO for 100 to 230 meV/atom. Even for Mn, rs-MnO is only slightly less stable than h-MnO for 40 meV/atom. This relative stability of rs-MO over h-MO may be attributed to the fact that the bonding network in the rs-MO phase, where each TM atom is coordinated

with four oxygen atoms, resembles their 3D *rs* counterpart, which has a very strong ionic nature. The ionicity of the TM-O bonds in *rs*-MOs is evidenced by the larger Bader charge on the TM atoms in the *rs*-MOs than the same TMs in the *h*-MOs as listed in Table 5.6. The TM atoms in the *rs*-MO phase has more Bader charge of 0.2 q than they do in the *h*-MO phase. In the case of Mn, the Bader charge on the Mn atoms is similar in size in both *rs*-MO and *h*-MO phases. In line with the successful synthesis of 2D *rs*-MnO nanosheets of 1 nm thickness[131], our finding here suggests that all these 2D *rs*-MO phases are energetically stable and can be synthesized to be promising candidates of 2D nanomaterials for future applications.

In the current study, we did not perform phonon calculations to confirm the dynamic stability of these 2D TMOs, nor did we perform molecular dynamics to confirm their stability at elevated temperature. However, the deviation in the static energy relative to room temperature is expected not to exceed 30 meV[34,195]. In addition, due to the fact that many 2D materials are actually in a meta-stable state and can be stabilized by adsorption on substrates[196–198], we expect that the current discussion in terms of formation energy is sufficient to give a qualitative indication of the likelihood of the existence of these 2D TMOs. Furthermore, it has been shown that the substrate stabilization can be as large as 8.84 kJ/mol-atom (91.6 meV/atom)[197]. Considering this considerable and sizable stabilizing energy, we are convinced that the these 2D TMOs can be experimentally realized upon choosing a suitable substrate. Furthermore, ideally substrate can be chosen which interacts with the synthesized thin film only via a weak van der Waals (vdW) force, hence the film can be stabilized without much interference with its electronic structure[198].

Inspired by the experimentally synthesized buckled structure of *h*-V_2O_3[199,200], we also examined the stability of the buckled 2D TMO phases by relaxing the buckled initial geometry where the O-sublayer was shifted 0.25 Åaway from the TM-sublayer. Table 5.2 presents the final vertical displacements together with other lattice parameters for all the most stable 2D TMOs. The Table shows that for *h*-ScO, *h*-TiO, *h*-VO, *rs*-CrO, and *h*-Ti_2O_3, the buckled structure us preferred and the vertical separation can be as large as 0.7 Å. *h*-CrO has only a negligible buckling of 0.03 Å. All the other buckled 2D TMO phases were relaxed to the planar geometry. The reason of the stability of these buckled 2D phases may be the pseudo-Jahn-Teller effect (PJTE)[201] which states that if the excited state geometry of a polyatomic system is very close in energy (nearly degenerate) to its ground state geometry, then these two states will be mixed via vibronic coupling, resulting in a symmetry-breaking distortion which stabilizes the system. The PJTE has been found in other 2D systems such as group-IV[202,203] and group-V[204] nanosheets. Indeed, for the buckled structures obtained in this study, the common characteristic of their electronic structure is that the

Table 5.1: Formation energy (eV/atom) calculated using Eq. 5.2. The magnetic ground states are included in parentheses. The *intalicized* energy values indicate the buckled structure, and the **bold** energy values are of the system at its structural and magnetic ground state. Fields with — indicate that the specific magnetic configuration was relaxed to NM.

a. *h*-MO

	NM	FM	AFM	FiM
ScO	*-2.350*	*-2.359*	***-2.367***	*-2.359*
TiO	***-1.753***	-1.734	-1.714	-1.742
VO	-1.084	***-1.261***	-1.212	-1.196
CrO	-0.567	-0.929	**-1.019**	-1.001
MnO	-0.434	-1.016	**-1.137**	-1.130

b. *rs*-MO

	NM	FM	AFM1	AFM2
ScO	**-2.470**	—	—	—
TiO	-1.884	-1.891	**-1.942**	-1.908
VO	-1.200	-1.331	**-1.430**	-1.332
CrO	-0.660	-1.103	***-1.250***	-1.248
MnO	-0.476	-1.087	**-1.098**	-1.055

c. *h*-M_2O_3

	NM	FM	AFM
Sc_2O_3	**-2.713**	—	—
Ti_2O_3	*-2.239*	*-2.307*	***-2.315***
V_2O_3	-1.590	**-1.821**	-1.711
Cr_2O_3	*-1.135*	**-1.394**	-1.359
Mn_2O_3	-0.973	*-1.222*	**-1.225**

d. *c*-MO_2

	NM	FM	AFM1	AFM2
ScO_2	-1.935	**-1.980**	—	-1.948
TiO_2	**-1.811**	—	—	—
VO_2	-1.600	**-1.681**	-1.680	-1.678
CrO_2	-1.173	**-1.378**	-1.338	-1.372
MnO_2	-0.925	-1.036	**-1.114**	-1.091

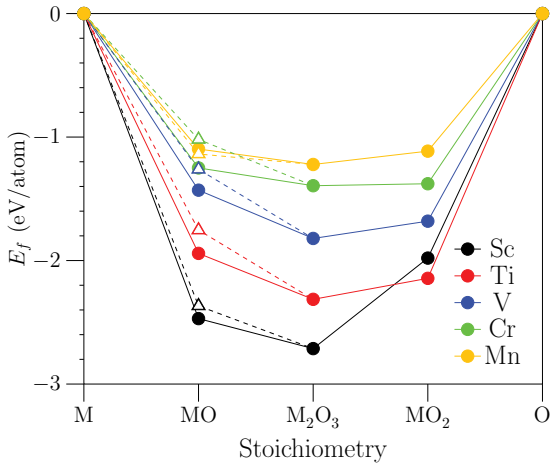

Figure 5.3: Concave-hull curves for the 2D TMOs. The triangle markers stand for the *h*-MOs. The circle markers stand for the most stable 2D TMO phases as listed in Table 5.5.

Table 5.2: Lattice parameters of the most stable 2D TMOs: Lattice constant a (Å), vertical displacement of the O-sublayer d (Å) with respect to the M-sublayer, and the angle between lattice constants θ (°)

TM	*h*-MO			*rs*-MO			*h*-M_2O_3			*c*-MO_2		
	a	d	θ	a	d	θ	a	d	θ	a	d	θ
Sc	3.774	0.522	60.4	2.985	0.000	90.0	6.650	0.000	60.0	4.008	0.000	90.0
Ti	3.092	0.710	60.0	2.855	0.000	90.0	6.301	0.153	60.0	3.746	0.000	90.0
V	3.236	0.385	60.0	2.809	0.000	90.0	6.181	0.000	60.0	3.647	0.000	90.0
Cr	3.282	0.029	58.3	2.794	0.220	90.0	6.137	0.000	60.0	3.580	0.000	90.0
Mn	3.282	0.000	64.2	2.870	0.000	90.0	6.159	0.000	60.0	3.556	0.000	90.0

conduction band minimum (CBM) is very close to, or even overlaps with, the valence band maximum (VBM), making the vibronic coupling more possible. We take the NM *h*-TiO, which has the largest buckling d = 0.71 Å, as the representative of all the other buckled 2D TMO phases for analyzing the difference of the electronic structure between the buckled and the planar geometries. In Fig. 5.4, the band structure (BS) of planar *h*-TiO is shown in gray, and the BS for buckled *h*-TiO in black. It is obvious that the geometry buckling opens up a band gap along the $\bar{K}\Gamma$ path in the reciprocal space. Fig. 5.5 presents the orbital-resolved BS's to give an insight on the consequence of PJTE on orbitals. From this Figure, it is clear that in the planar geometry, the Ti d orbitals can be categorized into three groups as the result of crystal field splitting: the d_{xz} and d_{yz} orbitals are degenerate, and the d_{xy} and $d_{x^2-y^2}$ orbitals are also degenerate. Only d_{z^2} orbital is distinct from other d orbitals in energy. The group of d_{xz} and d_{yz} contributes to the CBM and VBM crossing in the planar geometry. When the geometry is buckled, the two degeneracies of the Ti d orbitals are broken. The breaking of orbital degeneracy by buckling is especially significant for the d_{xz} and d_{yz} pair where the orbitals have a vertical z component. This can be seen by the opening of the band gap for buckled *h*-TiO; the CBM of the planar geometry at the K point, which is composed of the d_{xz} and d_{yz} orbitals, is pushed up in energy when the structure is buckled, so that the CBM is moved to the $K\Gamma$ path, and the band gap was created. The geometry buckling together with the tuning of the electronic structure of these 2D systems can be very useful in tailoring the material properties to broaden their applications[203].

It should be emphasized that regardless whether the buckled structure is more stable than the planar geometry or not, their energy difference is small. For example, $E(buckled) - E(planar)$ is 62 meV/f.u. for *h*-ScO (d=0.522 Å), 78 meV/f.u. for *h*-TiO (d=0.710 Å), and 94 meV/f.u. for *h*-VO (0.385 Å), respectively. For systems with smaller buckling, such as *h*-Ti_2O_3, the energy difference is even as small as 3 meV/f.u.. This small energy difference implies that the 2D TMO phases studied in the present work have a shallow potential energy surface (PES) where the planar and buckled geometries are two nearby local minima. In reality, the structural buckling can be affected by temperature, the slab thickness, or the strain from the substrate[204]. Interestingly, the buckling also shortens the TM-O bond length. In the case of *h*-TiO, the Ti-O bond length is shortened by 0.2 Å. Another related finding is that the O atom in the *h*-ScO, *h*-TiO and *h*-MnO unit cells moves toward one of the three NN TMs, lowering the local C_{3v} symmetry to C_s.

Figure 5.4: Comparison of band structures of the planar (gray) and buckled (black) forms of NM *h*-TiO.

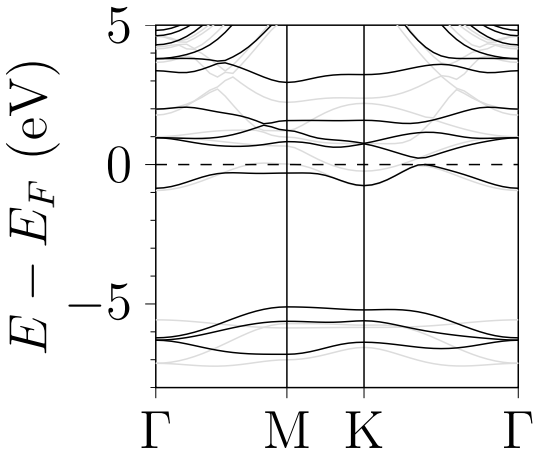

Relative stability between 2D and bulk TMOs

In addition to evaluating the relative stability among the 2D TMOs, it is informative to assess the relative stability of these 2D TMOs with respect to the bulk phases.

Concerning the bulk TMOs, the phases that were selected are listed in Table 5.3. When choosing these phases, two principles were followed to make these bulk structures as relevant to our theoretically predicted 2D phases as possible: (1) In addition to the same stoichiometry as the 2D phases, the bulk structures can be built up directly by the 2D counterparts. This is the case for *rs*– MO, and for *wz*-MnO with *h*-MnO. (2) Bulk structures were chosen that are relatively stable at low temperatures. This is to avoid possible structural/magnetic phase transitions at higher temperatures, and makes it more sensible to compare these structures with the 2D phases which were calculated at 0 K.

Due to the close similarity of 2D *h*-MOs and their 3D *wz*-MO counterparts, we also investigated the relative stability of the seven different magnetic orderings of the bulk *wz*-MOs, and the results are listed in Table 5.4. It is clearthat the energy differences are mostly very slight. Many of the magnetic phases relaxed to a NM state. The energies of the most stable structures can now be compared with the 2D *wz*-MOs.

The relative stability of the 2D TMOs with respect to the 3D counterparts is evaluated by comparing their total energies per atom directly:

$$\Delta E = E(2D) - E(3D). \tag{5.2}$$

This simple formula has been used to evaluate the stability of cadmium

Figure 5.5: Orbital-resolved band structure for the planar and buckled *h*-TiO NM phase.

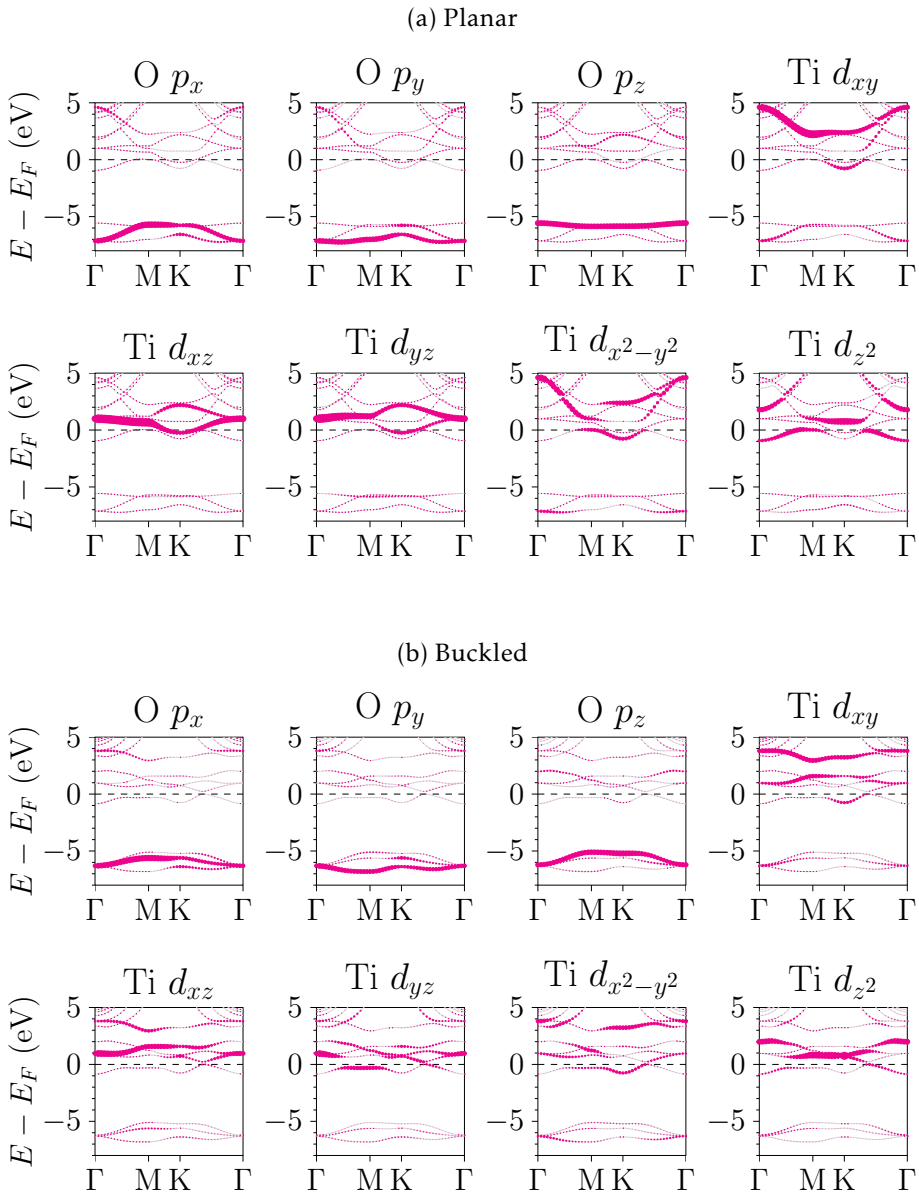

Table 5.3: Bulk TMO phases in different stoichiometries chosen from literature for the DFT and HSE calculations in this study.

Compound	Phase	Space group	Magnetism	Conductivity
	a. MO (rs, wz and other phases)			
ScO	RS[a]	$Fm3m$		
TiO	ϵ-TiO[130,205]	$P\bar{6}2M$	NM	metal
VO	distorted RS[130]	$R\bar{3}M$	AFM	metal
CrO	RS[206]	$Fm3m$	AFM or FM[a]	metal
MnO	RS[b, 184,188,189,207]	$Fm3m$	AFM-II	semiconductor
	WZ[184,185,189,208]	$P6_3mc$	AFM-III	semiconductor
	b. h-M_2O_3			
Sc_2O_3	bixbyite[209]	$Ia\bar{3}$	NM[c]	insulator
Ti_2O_3	corundum[145,210–212]	$R3c$	AFM1 (+ − −+)	semiconductor
V_2O_3	monoclinic[213,214]	$I2/a$	AFM	semiconductor
Cr_2O_3	corundum[210,215,216]	$R3c$	AFM(+ − +−, G-type)	semiconductor
Mn_2O_3	bixbyite[188,207,217]	$Ia\bar{3}$	AFM	metal
	c. c-MO_2			
ScO_2	Not found in literature[d]			
TiO_2	anatase[90,218]	$I4_1/amd$	NM	semiconductor
VO_2	M0[172](distorted rutile)[e]	$P21/c$	FM	metal
CrO_2	rutile[219,220]	$P4_2/mnm$	FM	half-metal
MnO_2	rutile[36,207]	$P4_2/mnm$	Non-collinear (NC) AFM[f]	semiconductor

[a] Bulk phase not found in literature. The RS structure was considered with 7 magnetic orderings as described in Ref. 189.

[b] MnO is in the RS structure and is paramagnetic with $T > T_N$=118 K; below the Néels temperature, MnO is AF2 with a rhombohedrally distorted structure (α=90.62°) determined by neutron scattering[221]. In 2006, it was found by refined neutron scattering that the rhombohedral MnO is in fact monoclinic[222]. However, DFT calculations mostly omit this slight deviation[189].

[c] Not found in literatiure; NM was considered here.

[d] Only another 2D phase (the 1-T phase) was theoretically predicted stable[180].

[e] Other references discussing VO_2[131,223,224].

[f] The spiral NC-AFM is the real magnetic ground state. However, we considered only the collinear (CL) AFM solution due to limited computational power. The moderate difference between the two magnetic states was given[207]: $\Delta E(NC - CL) = -47$ meV/f.u..

chalcogenide MLs[196] and other 2D materials[225] the likelihood for the 2D TMOs to grow into a 3D island or a 2D surface during the synthesis process. The results are presented in Table 5.5. One interesting finding is that 2D *rs*-TiO, *rs*-CrO, *rs*-MnO are more stable than their 3D *rs* counterparts. This suggests the possibility of forming 2D *rs*-MOs from 2D *rs*-MOs by exfoliation. However, the strong bonding network in the bulk *rs* structure should also be considered. To further analyze the underlying reason of the three 2D *rs*-MO being more stable than the corresponding bulk *rs* phases, the comparison of the orbital-resolved density-of-states (DOS) plots are given in Figure 5.8 for *rs*-MnO and in Appendix C for others. This comparison shows that the in 2D phases, $d_{x^2-y^2}$, d_{xz} and d_{yz} orbitals form the CBM of *rs*-TiO, d_{yz} and d_x form both the CBM and VBM of *rs*-CrO. The and d_{z^2} orbital for both the CBM and VBM of the *rs*-MnO plays an important role; probably these *d* bands participated in stabilizing the 3D material. The detailed orbital-resolved band structures are also included in Appendix C.

Except for the three aforementioned 2D *rs*-TMOs, all other 2D TMOs have a significantly higher energy than the corresponding 3D structures. This implies that these relatively unstable 2D TMOs will tend to form a bulk-like "nano island" on the substrate instead of a 2D slab. It would be informative to compare the energy of the 2D TMOs also with the surface energies of the bulk TMOs[185].

Table 5.4: Relative stability (meV/f.u.) of different magnetic orderings of the bulk *wz*-MO TMOs. The most stable magnetic phase for each compound is marked in **boldface**. NM indicates that the initial magnetic state is relaxed to non-magnetic.

TM	AFM1	AFM2a	AFM2b	AFM3	AFM4	FM	NM
Sc	NM	NM	3.070	NM	NM	0.397	**0.000**
Ti	NM	NM	NM	NM	NM	NM	**0.000**
V	NM	0.015	0.010	0.016	0.014	**0.000**	0.015
Cr	**0.000**	0.027	0.305	0.019	0.004	0.438	0.104
Mn	**0.000**	0.058	0.119	0.002	0.042	0.337	0.853

5.3.2 Electronic and magnetic properties of 2D TMOs

The band gaps and magnetic properties for the various 2D TMO phases are given in Table 5.6. The band structures are shown in Figure 5.6. By the comparison made in Table 5.6, we can see that HSE in most cases gives a better description of the strongly correlated *d* electrons than PBE as seen by an enlarged band gap. In particular, for *h*-CrO, *h*-Cr_2O_3, *c*-TiO_2, *c*-

Table 5.5: Relative stability of the 2D TMOs with respect to their 3D counterparts.

TM	*h*-MO[a]	*rs*-MO	M_2O_3	MO_2
Sc	0.475	0.433	0.856	—
Ti	0.508	-1.601	0.602	0.934
V	0.410	0.220	0.471	0.695
Cr	0.271	-0.023	0.593	0.574
Mn	0.290	-0.256	0.443	0.652

[a] $\Delta E = E(h\text{-MO}) - E(wz\text{-MO})$

VO_2, and *c*-MnO_2, PBE underestimated their band gap, such that they become conducting materials in the PBE scheme. However, HSE opened up the band gap and predicted these materials as semiconductors or half-metals. In the case of *rs*-MnO, PBE predicted it to be a metal, whereas HSE calculated it to be a semimetal with a tiny overlap of the VBM and the CBM.

Besides the comparison of PBE and HSE, we also found a rich variety of electronic properties among these 2D TMO phases. As indicated by the HSE calculations, we found not only semiconductors and metals among these 2D materials, but in particular, we also found that *rs*-MO is a semi-metal, and *c*-ScO_2, *c*-CrO_2 and *c*-MnO_2 are half-metals. One thing worth noting is that the semi-metallic *rs*-MnO is more stable than the *rs* bulk MnO, implying that this 2D material could possibly be synthesized and have a extraordinary electronic property. The half-metals can either be half-metallic ferromagnets (*c*-ScO_2), or half-metallic antiferromagnets (*c*-CrO_2 and *c*-MnO_2), holding great potential in spintronics applications. To understand the half-metallic property in more detail, the spin-polarization analysis of the ratio of spin-up and spin-down density of states at the Fermi level is performed. This analysis serves as a criterion to determine the extent of spin polarization, hence the degree of half-metalicity[226–228], of a certain material. The spin polarization is defined as

$$P = \frac{D^{\uparrow}(E_F) - D^{\downarrow}(E_F)}{D^{\uparrow}(E_F) + D^{\downarrow}(E_F)}. \tag{5.3}$$

In Eq. 5.3, $D(E_F)$ is the magnitude of density of states at the Fermi level for spin-up and spin-down states. $P = \pm 1$ indicates that the system is half-metallic. Whereas $P = 0$ shows that the system has an equal amount of spin-up and spin-down states at the Fermi level. Indeed, DOS analysis shows that for *c*-ScO_2, *c*-CrO_2, and *c*-MnO_2, their spin polarization is equal to the ideal value of 1.

Lastly, the Dirac-cone-like shape of dispersion curves was found in *h*-

Table 5.6: Electronic and magnetic properties of 2D TMOs. Electronic ground state (EGS) and magnetic ground state (MGS). SC: semiconductor, SM: semimetal, HM: half-metal, M: metal

	Method	EGS	MGS	Band gap		Mag. moment		Bader charge	
				↑	↓	TM	O	TM	O
a. *h*-MO									
ScO	DFT	SC	AFM	0.360	0.360	±0.23	0.00	1.32	-1.32
	HSE	SC	AFM	1.047	1.047	±0.21	±0.02	1.41	-1.41
TiO	DFT	SC	NM	0.223	—	—	—	1.19	-1.19
	HSE	SC	NM	0.283	—	—	—	1.27	-1.27
VO	DFT	SC	FM	0.514	5.160	2.80	0.20	1.24	-1.24
	HSE	SC	FM	0.552	6.773	2.86	0.14	1.29	-1.29
CrO	DFT	M	AFM	—	—	±3.31	±0.04	1.24	-1.24
	HSE	SC	AFM	2.110	2.110	±3.61	±0.10	1.30	-1.30
MnO	DFT	SC	AFM	0.632	0.632	±4.37	±0.10	1.28	-1.28
	HSE	SC	AFM	2.110	2.110	±4.61	±0.08	1.42	-1.42
b. *rs*-MO									
ScO	DFT	M	NM	—	—	—	—	1.51	-1.51
	HSE	M	NM	—	—	—	—	1.62	-1.62
TiO	DFT	M	AFM1	—	—	±1.03	0.00	1.39	-1.39
	HSE	M	AFM1	—	—	±1.22	0.00	1.50	-1.50
CrO	DFT	SC	AFM1	0.361	0.361	±3.46	0.00	1.40	-1.40
	HSE	SC	AFM1	3.119	3.119	±3.66	0.00	1.46	-1.46
VO	DFT	M	AFM1	—	—	±2.33	0.00	1.36	-1.36
	HSE	M	AFM1	—	—	±2.61	0.00	1.45	-1.45
MnO	DFT	M	AFM1	—	—	±4.20	0.00	1.31	-1.31
	HSE	SM	AFM1	-0.038	-0.038	±4.64	0.00	1.44	-1.44
c. *h*-M_2O_3									
Sc_2O_3	DFT	SC	NM	2.889	—	—	—	1.88	-1.25
	HSE	SC	NM	4.350	—	—	—	1.99	-1.33
Ti_2O_3	DFT	SC	AFM	0.926	0.926	±0.89	0.00	1.69	-1.13
	HSE	SC	AFM	3.230	3.230	±0.95	0.00	1.81	-1.21
V_2O_3	DFT	M	FM	—	—	2.00	0.00	1.56	-1.04
	HSE	M	FM	—	—	2.10	-0.06	1.65	-1.10
Cr_2O_3	DFT	HM	FM	—	3.936	2.96	0.02	1.51	-1.01
	HSE	SC	FM	0.878	5.732	2.93	0.05	1.65	-1.10
Mn_2O_3	DFT	SC	AFM	0.616	0.934	4.15; -2.24	0.03	3.45	-0.97
	HSE	SC	AFM	3.024	3.771	4.55; -2.69	0.05	3.54	-1.02

Table 5.6: Continued.

	Method	EGS	MGS	Band gap ↑	Band gap ↓	Mag. moment TM	Mag. moment O	Bader charge TM	Bader charge O
				d. *c*-MO_2					
ScO_2	DFT	HM	FM	3.255	—	-0.05	0.53	1.98	-0.99
	HSE	HM	FM	5.207	—	-0.09	0.54	2.08	-1.04
TiO_2	DFT	SM	NM	-0.002	—	—	—	2.09	-1.04
	HSE	SC	NM	0.126	—	—	—	2.28	-1.14
VO_2	DFT	HM	FM	-0.360[a]	0.814	0.18	-0.09	1.86	-0.93
	HSE	SC	FM	0.654	1.928	1.12	-0.06	2.06	-1.03
CrO_2	DFT	HM	FM	—	0.464	2.22	-0.11	1.75	-0.88
	HSE	HM	FM	—	2.911	2.54	-0.27	1.93	-0.97
MnO_2	DFT	M	AFM1	—	—	±2.58	0.03	1.68	-0.84
	HSE	HM	AFM1	4.069	—	±3.48	0.50	1.93	-0.96

[a] SM

TiO and h-V_2O_3. Especially, h-V_2O_3 is a ferromagnetic material. The combination of magnetism and the massless behavior of the fermions make h-V_2O_3 a promising candidate for spintronics and electronic applications.

5.4 Transition metal vacancies in 2D TMOs

Besides the detailed study of the perfect 3D and 2D TMO compounds in the foregoing sections, we also explored the properties of point defects in 2D TMOs. Due to the vast variety of the 2D TMOs selected in this study and the huge amount of computation needed for symmetry-breaking magnetic configurations, here we limit ourselves to the transition metal monovacancies in the most stable 2D TMOs, which are the h-M_2O_3 systems. We chose the transition metal monovacancies because the missing of the transition metals may potentially have great impact on the overall magnetism of the whole system. In the following paragraphs, the formation energy, the local structural relaxation, and the magnetic properties of these transition metal vacancies will be discussed.

The TM vacancies were created in 4×4 supercells of h-M_2O_3 slabs, which are longer than 25 Å along both the x and y directions and includes in total 80 atoms ($M_{32}O_{48}$). This cell size was tested for convergence of the vacancy formation energy within 1 meV/atom. Because of limitations in the computational power, only the Γ point was included in the k-point sampling. The magnitude of the initial magnetic moments were set to 4 μ_B and 0 μ_B for TMs and oxygen atoms, respectively. The orientation of these magnetic moments were set according to the ground state magnetic configuration of the host perfect h-M_2O_3 systems. The atomic coordinates

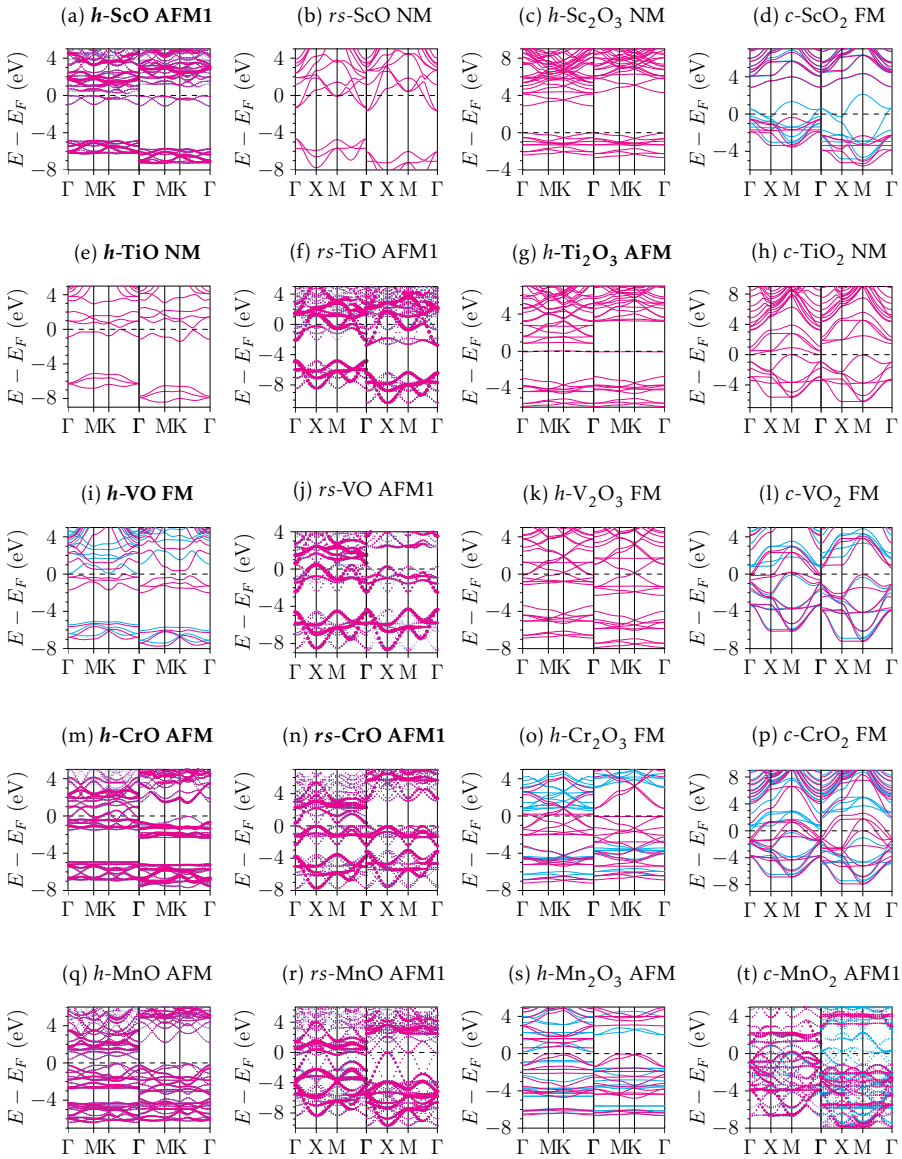

Figure 5.6: Band structures (BSs) of each ML TMO in their ground state geometry and magnetic configurations. **Bold captions** indicate buckled structure. The spin-up states are denoted in magenta, and spin-down states in cyan. Bands calculated using supercells were unfolded.

Figure 5.7: Orbital-resolved band structure of 2D *rs*-MnO. The Fermi level set at zero energy.

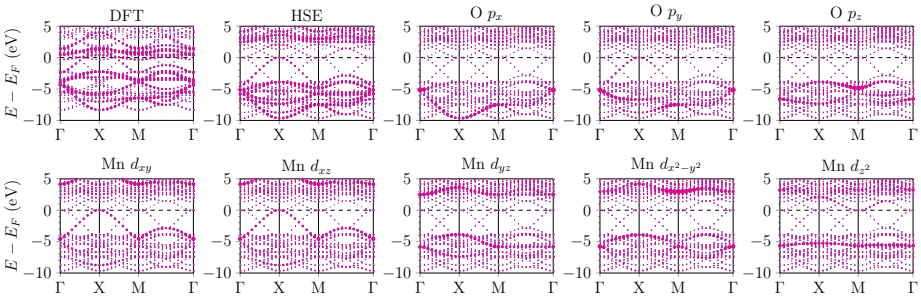

Figure 5.8: Orbital-resolved DOS of both 2D and 3D *rs*-MnO. The Fermid level was set at of energy. The colors pink and blue indicating the spin-up and spin-down states of the 2D phase. The orange and green colors indicate the spin-up and spin-down states of the 3D phase.

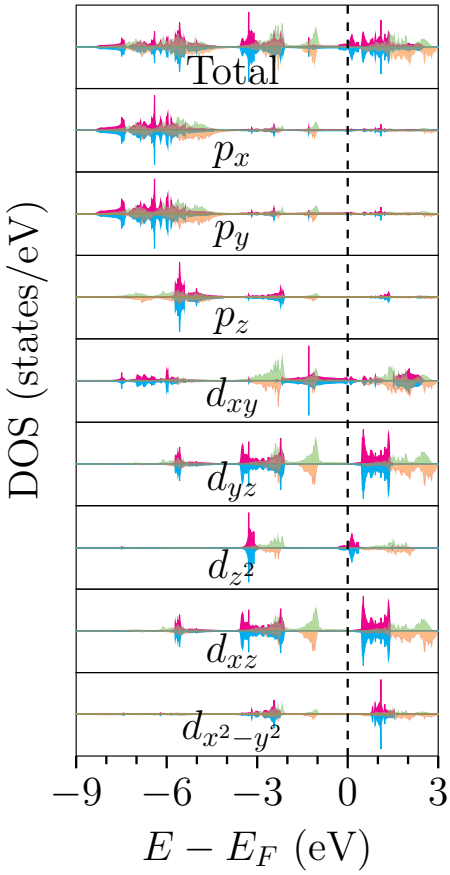

Table 5.8: Formation energy (eV) of the transition metal monovacancies (V_{TM}) in h-M_2O_3.

V_{TM}	O-rich	O-poor
V_{Sc}	5.711	12.496
V_{Ti}	-1.879	3.907
V_V	-2.316	2.237
V_{Cr}	-2.146	1.339
V_{Mn}	-0.734	2.300

as well as the magnetic moments were fully relaxed at the fixed lattice constants which were obtained beforehand by relaxing the unit cells using the PBE functional. The vacancy formation energy is defined as

$$E_f(V_M) = E(\mathrm{M_{31}O_{48}}) - E(\mathrm{M_{32}O_{48}}) + \mu_{TM}. \tag{5.4}$$

In Eq. 5.4, $E(\mathrm{M_{31}O_{48}})$ and $E(\mathrm{M_{32}O_{48}})$ are the energies of V_{TM}@h-M_2O_3 and perfect h-M_2O_3 systems, respectively. μ_{TM} is the chemical potential of the transition metal atoms and will vary depending on different chemical environments during the synthesis of h-M_2O_3. The boundaries of these chemical potentials should be determined according to the chemical reaction taking place in the synthesis. Typically, the oxygen pressure is an important parameter to control the product of the synthesis of transition metal oxides. Therefore we consider here two extreme synthesis conditions: the O-rich and the O-poor cases. We use the following reaction to describe the synthesis of h-M_2O_3:

$$2M_{(s,\,bulk)} + \frac{3}{2}\mathrm{O}_{2(g)} \rightarrow \mathrm{M_2O_{3(s,\,ML)}} \tag{5.5}$$

Based on Eq. 5.5 and the derivation procedure described in Chap. 2, we find that in the O-rich environment, μ_{TM} reaches its lower limit of $\frac{1}{2}E(\mathrm{M_2O_3}) - \frac{3}{4}E(O_{2(g)})$. In the O-poor (TM-rich) condition, $\mu(TM)$ reaches its maximum of $E(TM_{(bulk)})$. Here $E(O_{2(g)})$ is the total energy for the paramagnetic O_2 molecule, and $E(TM_{(bulk)})$ is the total energy per atom for the transition metals in their bulk phases. The calculated range of vacancy formation energy for V_{TM}'s are listed in Table 5.8.

The spin density plots, defined as the difference between the spin-up charge density and the spin-down charge density, are given in Figure 5.9.

$\mathbf{V_{Sc}}$@h-$\mathbf{Sc_2O_3}$

Although the formation energy of V_{Sc} is very high in comparison to the other systems listed in Table 5.8 (5.711 eV in the O-rich condition and

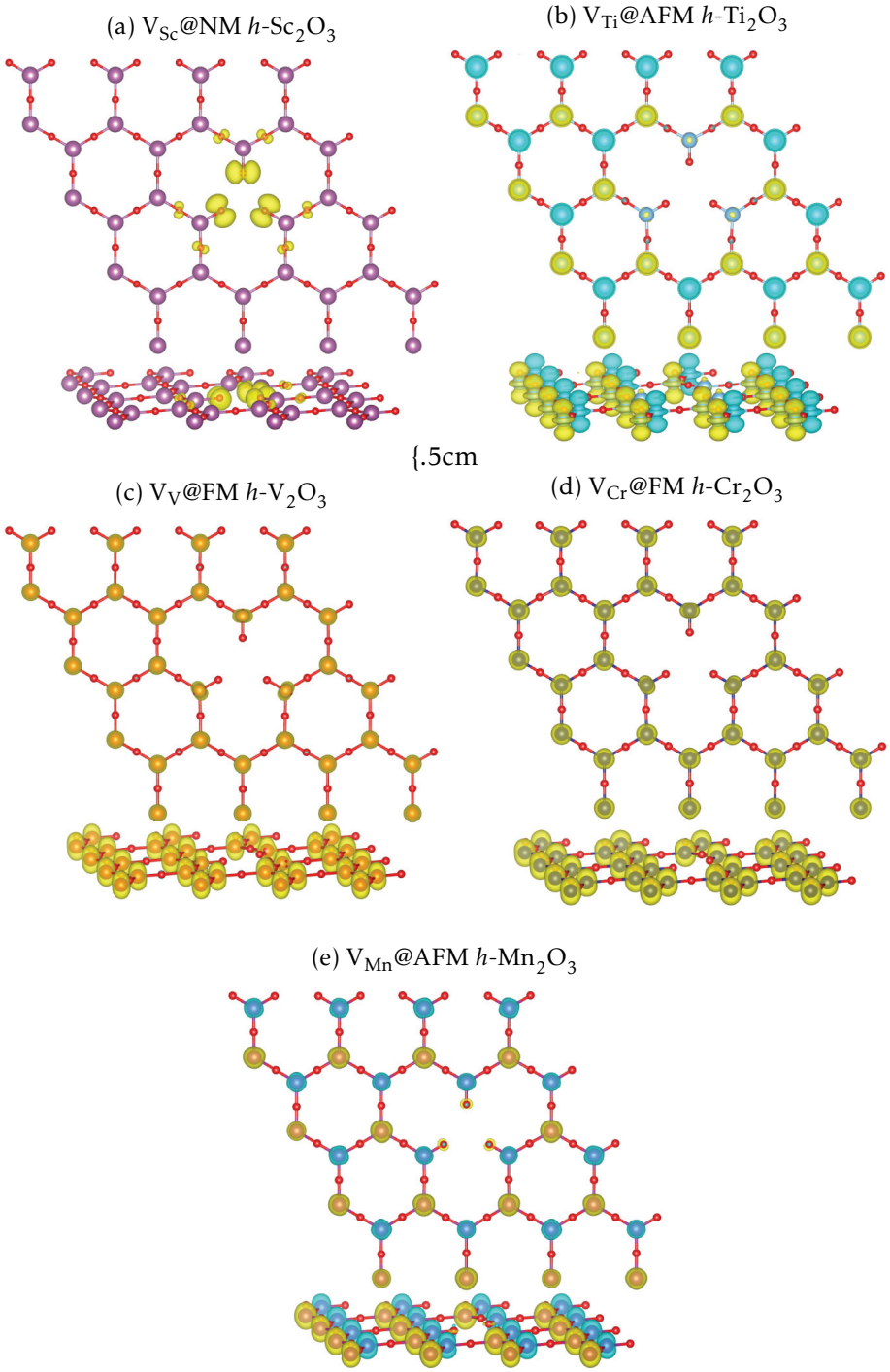

Figure 5.9: Spin density plots for the five V_{TM}@h-M_2O_3 systems. The isosurface level is 0.004 $e/Å^3$, 0.006 $e/Å^3$, 0.03 $e/Å^3$, 0.03 $e/Å^3$, and 0.03 $e/Å^3$, for panels (a) to (e), respectively. Spin-up density is colored in yellow, and spin-down density in blue.93

Table 5.9: Net magnetic moments (μ_B/supercell) of the h-M_2O_3 systems with or without V_{TM}.

	Perfect	With V_{TM}
h-Sc_2O_3	0.00 (NM)	3.00
h-Ti_2O_3	0.00 (AFM)	2.00
h-V_2O_3	64.00 (FM)	59.00
h-Cr_2O_3	96.00 (FM)	90.00
h-Mn_2O_3	0.00 (AFM)	8.44

12.496 eV in the O-poor condition), we nonetheless discuss its influence on the host 2D slab.

The bond length for the Sc-O bonds away from the vacancy site is 1.92 Å. But the nearest Sc-O bonds around the V_{Sc} site are slightly elongated to 1.94 Å, indicating that the NN S atoms of the vacancy site are drawn closer toward the vacancy center.

The host h-Sc_2O_3 system is originally NM. The DFT pseudopotentials (PPs) usually only consider the outer shell electrons which are chemically active and ignore the core electrons. Therefore, within the DFT PPs the electronic configuration of the Sc atom is $3s^2 3p^6 3d^1 4s^2$ – in total 11 electrons. When one Sc atom is removed from h-Sc_2O_3, band analysis shows that the system loses 4 spin-up electrons and 7 spin-down electrons. Thus the system has now 3 extra spin-up electrons, corresponding to a net magnetic moment of 3 μ_B for the whole system. for the whole system. The spin density plot of V_{Sc}@h-Sc_2O_3 in Fig. 5.9 (a) shows clearly that major part of this magnetic moment is equally distributed over the three NN oxygen atoms of the vacancy site. By using the Bader volume, the magnitude of the magnetic moment at each NN oxygen atom is calculated to be 0.95 μ_B, in good agreement with the expected 3 μ_B for the whole system. This net magnetic moment changes the total system from a non-magnetic material into a dilute magnet. DOS analysis reveals that these magnetic moments are composed of the p_x and p_y orbitals of the O atoms nearest-neighboring the vacancy. The local magnetic pattern around the vacancy site has the D_{3h} symmetry.

V_{Ti}@h-Sc_2O_3

The formation energy for V_{Ti} in h-Ti_2O_3 is -1.879 eV in the O-rich condition, and 3.907 eV in the O-poor condition. The negative formation energy implies that either the system will be stabilized upon the creation of the Ti vacancies, or the h-Ti_2O_3 tends to undergo a phase transition to a structure having higher oxygen ratio such as TiO_2.

Besides the slight bond length distortion, the presence of V_{Ti} causes the NN O atoms to be exposed to each others' charge density, leading to

a slight repulsion between the oxygen atoms and the result is a shorter Ti-O bonding of 1.63 Å (the bond length is on average 1.83 Å for h-Ti_2O_3) around the vacancy site.

The most stable magnetism for a defect-free h-Ti_2O_3 slab is AFM, where the magnetic moments are composed of the Ti d_{z^2} and d_{xz} orbitals. One Ti atom has 12 electrons in the DFT PP, and its electronic configuration is $3s^2 3p^6 3d^2 4s^2$. When one Ti vacancy is created, band analysis shows that there are two unpaired spin-up electrons corresponding to a net magnetic moment of 2.00 μ_B for the whole system. Figure 5.9 (b) shows that these two spin-up electrons are mostly distributed equally on the three next-nearest-neighboring (NNN) Ti atoms and compensate their spin-down magnetic moments. Magnetic moment calculation using Bader volumes shows that each of these spin-down magnetic moment is reduced from -0.89 μ_B to 0.09 μ_B. As the result, V_{Ti}@h-V_2O_3 is a dilute magnet.

$\mathbf{V_V}$@h-$\mathbf{V_2O_3}$

In the O-rich condition, the formation energy for V_V is -2.316 eV. This negative formation energy suggests that the V_V@h-V_2O_3 system has a lower energy and is more stable than perfect h-V_2O_3. It may also imply that when h-V_2O_3 is exposed to a rich source of oxygen, this abundant amount of oxygen molecules will stimulate h-V_2O_3 to loose the V atoms and undergo a transition toward another phase with higher O-stoichiometry, such as VO_2. In the O-poor condition, on the other hand, V_V defects have a formation energy of 2.237 eV. This may imply that when there is a deficiency of oxygen in its surrounding environment, h-V_2O_3 has no tendency to loose V atoms and will stay at its equilibrium stoichiometry. Thus it costs energy to remove a V atom from h-V_2O_3.

The NN oxygen atoms were pushed away from the vacancy site, leading to a shorter V-O bond length for the NN V-O pairs of around 1.60 Å compared to the bond length of 1.78 Å for V-O pairs far from the vacancy site.

The pristine h-V_2O_3 has a FM magnetic ground state. These magnetic moments are all composed of the d_{xz} and $d_{x^2-y^2}$ orbitals of the V atoms. With the 4x4 supercell $V_{32}O_{48}$, the net magnetic moment is 64 μ_B. The electronic configuration of one V atom in the DFT PP is $3s^2 3p^6 3d^3 4s^2$ – in total 13 electrons. When a V_V is created, h-V_2O_3 loses these 13 electrons (9 spin-up and 4 spin-down). Consequently the system has an excess of 5 spin-down electrons, leading to a net magnetic moment of 59 μ_B. Fig. 5.9 (c) indicates that although the original FM arrangement is not affected by V_V, the size of the magnetic moments on V atoms are reduced. In particular, the magnetic moments of the NN V atoms around the vacancy site drop from 2.00 μ_B to 1.38 μ_B. The polarization of these magnetic moments displays the D_{3h} symmetry as can also be seen in Fig. 5.9 (c).

V_{Cr}@h-Cr_2O_3

V_{Cr} has a formation energy of -2.146 eV in the O-rich condition, and 1.339 in the O-poor condition. The negative formation energy of V_{Cr} in the O-rich condition, like already discussed for other V_{TM}s, is an implication of either the structural stabilization of h-V_2O_3 by creating a V vacancy, or a driving force toward a high O-stoichiometry phase. The low formation energies of V_V in the O-poor condition suggests that V_{Cr} can exist in a appreciable concentration during synthesis.

Similar to V_V@h-V_2O_3, V_{Cr} also repels slightly the NN O atoms, resulting in a shorter bond length of the NN Cr-O pairs (1.59 Å) compared to the average Cr-O bond length of 1.77 Å.

The host h-Cr_2O_3 system has the FM arrangement as its magnetic ground state. The magnetic moments are spin-up and located on the Cr atoms with a magnitude of 2.96 μ_B, and they are composed of the Cr d_{xz} and $d_{x^2-y^2}$ orbitals. One Cr atom has the electronic configuration of $3s^2 3p^6 3d^5 4s^1$, thus in total 14 electrons. When losing one Cr atom, it loses these 14 electrons in which 10 are spin-up and 4 are spin-down. Therefore in the end the whole system loses 6 spin-up electrons, leading to a drop of the overall magnetic moment from 96 μ_B to 90 μ_B. Fig. 5.9 (d) shows that the vacancy does not influence the original FM ordering, but reduces the size of the magnetic moment on the NN Cr atoms from 2.96 μ_B to 2.11 μ_B. Also, the vacancy polarizes these magnetic moments into the D_{3h} symmetry.

V_{Mn}@h-Mn_2O_3

The formation energy for V_{Mn} in h-Mn_2O_3 is -0.734 eV and 2.300 eV in the O-rich condition and the O-poor condition, respectively. V_{Mn} causes a similar local geometry relaxation as V_{Ti}@h-Ti_2O_3 – the bond length of the NN Mn-O pairs is around 0.1 Å shorter than the average value.

The defect-free h-Mn_2O_3 phase is an AFM material at its ground state. In the DFT PP framwork, the 3s orbital of the Mn atom is not included, thus one Mn has 13 electrons with the configuration $3p^6 3d^5 4s^2$. When one V_{Mn} is created, h-Mn_2O_3 loses these 13 electrons (3.26 spin-up and 11.70 spin-down) and the net spin is 8.44 μ_B. Fig. 5.9 (e) shows that V_{Mn} does not alter the overall AFM pattern of the host h-Mn_2O_3. However, further analysis using Bader volume indicates that the presence of one V_{Mn} has increased the size of the spin-up magnetic moments from 3.00 μ_B of the perfect h-Mn_2O_3 system to 3.31 μ_B, and lowers the size of the spin-down magnetic moments from 3.00 μ_B to 2.61 μ_B. The vacancy also induces a tiny amount of magnetic moment ($\sim$ 0.04 μ_B) at the NN O atoms. The magnetic moments around the vacancy site are also slightly polarized to become D_{3h} symmetric.

To summarize, the transition metal vacancies in h-M_2O_3, except V_{Sc}, have a reasonably low formation energy ranging from 3.9 eV to 1.3 eV in the O-poor condition. This suggests the presence of these vacancies during synthesis under low oxygen pressure. In the O-rich condition, in which the material is exposed in an environment with high oxygen pressure during synthesis, the transition metal vacancies (except V_{Sc}) could stabilize the host material as indicated by the negative vacancy formation energy. Alternatively, the high oxygen pressure may result in a (partial) phase transformation to MO_2. The high formation energy of V_{Sc} suggests that these defects are unlikely to be formed.

All these vacancies, having a point defect nature, cause only a slight local relaxation of the geometry of the host material. If the corresponding perfect system is magnetic (AFM or FM), V_{TM} will cause NN O atoms to repel each other, leading to a shortening of the bond length of the NN M-O pairs. The hexagons in the h-M_2O_3 network are also slightly distorted by one to two degrees.

For h-Sc_2O_3, for which the perfect host material is NM, the presence of a V_{Sc} induces a magnetic moment of 3 μ_B localized at the NN O atoms of the vacancy site, turning the material to a dilute magnet. For the other four magnetic (AFM or FM) host materials, the transition metal vacancy will reduce the magnetic moment of the NN transition metals, and polarize these moments into the D_{3h} symmetry.

5.5 Conclusion and outlook

In conclusion, we have carried out a systematic first-principles study of 2D TMOs. The energetics, structural properties, electronic and magnetic properties of four atomically-thin 2D TMO phases with all possible collinear magnetic arrangements were calculated and analyzed. The relative stability of the 2D TMOs were also compared to their 3D counterparts. In addition to the perfect 2D TMOs, the transition metal monovacancies in the h-M_2O_3 phase were also calculated.

(i) *Energetics and structural stability*

We have found that all these 2D phases have negative formation energies with respect to the elemental transition metal bulk phases and the paramagnetic oxygen gas, indicating the static stability and likelihood of these 2D phases to be synthesized experimentally. Although the h-M_2O_3 phase has the lowest formation energy, the concave-hull plot shows that all the 2D TMO phases are stable at their respective stoichiometry.For all TMOs except MnO, the *rs*-MO phase is more stable than the h-MO phase, and the possible reason is the stronger ionicity of the M-O bonding in the *rs*-MO systems as supported by the larger Bader charge on the TM atoms in *rs*-MO. h-ScO, h-TiO, h-VO, *rs*-CrO, and h-Ti_2O_3 were found to be more

stable in the buckled structure with a vertical separation between the TM-sublayer and the O-sublayer that can be as large as 0.7 Å. Comparing to the 3D bulk phases, all the 3D TMO phases are significantly higher in energy except the *rs*-MO phase, implying that these 2D phases may crystallize into a 3D nanoisland instead of a 2D nanosheet during synthesis. The study of the energetics among the 2D TMO phases and with respect to the 3D bulk TMO phases highlighted the stability of the 2D *rs*-MO phase which, together with their structural flexibility and unique electronic and magnetic properties, holds a great potential for low-dimensional materials science and technology.

(ii) *Electronic and magnetic properties*
By using the HSE hybrid functional, a rich variety of electronic and magnetic properties of these 2D TMOs were discovered in this study. In particular, *rs*-MO is predicted to be a semi-metal with the AFM1 magnetic configuration; *c*-ScO_2 and *c*-CrO_2 are found to be FM half-metals, while *h*-MnO_2 is an AFM half-metal. Also, Dirac-cone-like bands were found for *h*-TiO and *h*-V_2O_3. All these remarkable properties indicate that 2D TMOs are bright candidates for electronic, magnetic, and spintronics applications.

It is also worth noting that the hybrid functional gives a scenario of the electronic properties of 2D TMOs which is significantly different from the DFT method. In general, HSE successfully opens a band gap for materials which are predicted as metals by traditional DFT. This shows the necessity of using more advanced electronic structure methods to treat these strongly correlated systems.

(iii) *Transition metal monovacancies (V_{TM}'s)*
The calculation of vacancy formation energy indicates that except V_{Sc} , all the V_{TM}'s have a reasonably low formation energy ranging from 3.9 eV to 1.3 eV in the O-poor condition. In the O-rich condition, all the V_{TM}'s except V_{Sc} even possess a negative formation energy, indicating that the whole system will be stabilized by loosing a transition metal atom. Depending on the original magnetic configuration of the host *h*-M_2O_3, V_{TM}'s will reduce the magnetic moment on the NN transition metal atoms and polarize the local symmetry of the magnetic moments into D_{3h}.

The current study presents the possibility of creating these novel 2D TMO phases and highlighted their remarkable electronic and magnetic properties. For a future work, a detailed study of the substrate effect is crucial toward the understanding of a more realistic growth process of these 2D TMOs. Furthermore, a comprehensive study of point defects in which oxygen monovacancies, interstitials, antisites, and dopants, and even the mutual interaction of these different kinds of defects, is very important for successful defect engineering in 2D TMOs.

5.6 Acknowledgements

This project is a collaboration with Chang-Ming Fang and Rik Koster, and it is financially supported by the Dutch science foundation NWO via a VIDI grant (grant number 723.012.006). W.F. Li gratefully acknowledges Jyh-Pin Chou for his detailed discussions on VASP settings, and Somil Gupta for his suggestion of the formula used to evaluate the stability of 2D TMOs with respect to their 3D counterparts. W.F. Li gratefully acknowledges Jyh-Pin Chou for his detailed discussions on VASP settings, and Somil Gupta for his suggestion of the formula used to evaluate the stability of 2D TMOs with respect to their 3D counterparts.

Summary

Along with the rapid advancement of materials science and technology at the nanometer scale, more and more hitherto unknown physical phenomena of nanomaterials are emerging and await full exploration. Density functional theory (DFT), as a powerful theoretical tool and the workhorse of electronic structure calculations for periodic systems, has been proven to be able to, and is more and more widely applied to explore, explain, and even predict the physics of novel nanomaterials. Meanwhile, as already destined by the second law of thermodynamics, point defects are omnipresent in nanocrystals. These point defects not only break the translational symmetry of the lattice, but also play a crucial role in determining the physical properties and overall performance of the host material. This thesis is devoted to exploring the role of various kinds of point defects in nanomaterials, both 2D and 3D, by DFT. The exploration started with point defects in 3D lead chalcogenides (PbX, X=S, Se, Te), passed through the spin-orbit (SO) splitting of defect states in WS_2 monolayers (MLs), which belong to the family of 2D transition metal dichalcogenides (TMDs), and arrived at the prediction of novel 2D ML structures of transition metal oxides (TMOs, with TM=Sc, Ti, V, Cr, Mn).

In Chapter 3, through the application of DFT, the geometry, energetics, and electronic characteristic of point defects inside PbX semiconductors as studied systematically are described by means of DFT. The type of point defects include monovacancies, interstitials, Schottky defects (cation and anion vacancy pairs), and Frenkel (cation or anion vacancy + interstitial). The monovacancies and Schottky defects are more favorable as indicated by the lower defect formation energy. For photoluminescence applications, the lead monovacancy (V_{Pb}) was predicted to be a shallow acceptor state, and will likely participate in radiative recombination. In contrast, the sulfur monovacancy (V_S) is a deep donor state which will trap the conducting holes in *p*-type PbX, thereby also reducing the photoluminescence yield. Concerning off-stoichiometry, although the formation energy of V_{Pb} is smaller than V_X for all PbX systems, which implies that an excess of anions is more easily accommodated than an excess of cations, the defect energies for both defect types are still quite high, so that off-stoichiometry

is unfavorable. Phase separation may be hampered by a nucleation barrier for the formation of pure Pb and X phases. For the case of nanocrystals, part of the off-stoichiometry can be accommodated at the surface, also depending on the type of ligands used. Considering all the defect formation energies, Schottky defects are significantly lower in formation energy than the cation and anion monovacancies. Therefore, it becomes clear that the Schottky defects may play a much more important role in the cation exchange process of the PbSe-CdSe heteronanocrystals (HNCs) than currently presumed. Because of huge displacements of nearest-neighboring (NN) atoms around interstitial-type defects, anion and cation interstitial defects and Frenkel defects are less favored. The result of local relaxations showed that the expansion or contraction of the NNs of a defect site is a net result of the electrostatic interaction among the atoms in that local environment. Bader charge analysis revealed that the degree of charge transfer decreases with O → S → Se → Te, in accordance with the trend of their electronegativity. Charge density difference plots indicated that charge density is locally polarized around the defect site, and electride type behavior with trapped charge is found at the anion vacancy site. The work in Chapter 3 presents a rich variety of physical properties which are introduced by defects in the PbX semiconductor family, with direct implications for the synthesis and performance of PbX-containing HNCs. For a future work, this study could be extended to charged defects, and to the calculation of energy barriers for migration of vacancy-type defects.

In Chapter 4, the energy splitting of the defect states due to spin-orbit coupling (SOC) in 2D WS_2 MLs is described as quantitatively characterized using DFT and the hybrid functional formulated by Heyd, Scuseria and Ernzerhof (HSE). It was found that among all the point defects, the sulfur monovacancy (V_S) and the sulfur interstitial (S_i) possess the lowest formation energies. Besides the V_S, S_i, other two kinds of antisite defects (W_S and W_{S2}) were also chosen for the investigation of the SO band splitting of the defect states, as antisite defects were previously reported to possess a sizable magnetic moment. We have shown that the SO splitting depends on both the orbital constitution and the orientation of magnetization of the defect states. The states having the d_{xy} and $d_{x^2-y^2}$ character will undergo significant SO splitting when the magnetization is oriented along the m_z magnetization axis. The largest SO splitting occurs in the case of W_S antisite, and this strong SO splitting of 296 meV (356 meV by HSE) is comparable to the native WS_2. For S_i no SO splitting was found as the defect state is composed solely by the d_{z^2} and p_z orbitals. Besides the SO splitting, we also confirmed that both the W_S and W_{S2} antisite defects possess a local magnetic moment of 2 μ_B around the antisite W atom due to the two unpaired spin-up electrons occupying the d_{xy} and $d_{x^2-y^2}$ defect states. The antisite W atom together with its first- and second-nearest

neighboring W atoms thus form the so-called *superatom*.

In Chapter 5, DFT together with HSE is used to study 2D transition metal (TM) materials. Here the topic of investigation are the 2D transition metal oxides (TMOs), with the TMs being the early 3*d* transition metals: Sc, Ti, V, Cr, Mn. By varying the valence state of the TM atoms, we have rationally designed four different 2D ML structures with single-atom thickness for the five TMOs. These structures are hexagonal MO (*h*-MO, with M being the transition metal), rock salt MO (*rs*-MO), hexagonal M_2O_3 (*h*-M_2O_3), and cubic MO_2 (*c*-MO_2). The ground state energy, geometry and magnetic ordering of each 2D TMO were determined. The relative stability among all the 2D TMOs was assessed in terms of formation energy per atom. It was found that the hexagonal M_2O_3 phase is the most stable phase among all the 2D TMO phases with respect to the elemental TM bulk phase and the paramagnetic oxygen molecule. Three out of the five *h*-MO phases prefer a buckled structure. We also evaluated the relative stability of each 2D TMO with respect to their 3D counterparts having the same stoichiometry. This comparison showed that three out of five *rs*-MOs are more stable than their bulk counterparts, thereby strongly suggesting that during the deposition growth, the material would more likely grow into a planar 2D thin film instead of a 3D nano-island on the substrate. We have also pointed out that upon choosing a proper substrate, it is likely possible to experimentally synthesize these 2D TMOs. The calculations showed that these 2D TMOs have a wide range of electronic and magnetic properties. This includes semimetals, half-metals, and semiconductors with different magnetic arrangements such as non-magnetic, ferromagnetic, and antiferromagnetic. This spectacular variety of magnetic and electronic properties indicates that these novel 2D TMOs hold a great potential for future applications in electronic- and spin-related fields. Furthermore, we also investigated the transition metal monovacancies (V_{TM}'s) in the *h*-M_2O_3 phase which possesses the lowest formation energy among all the 2D TMO phases. Except for V_{Sc}@*h*-Sc_2O_3, all other V_{TM}'s have a reasonably low formation energy under the O-poor condition, and will even stabilize the whole system under the O-rich condition. These vacancies, except V_{Sc}, will also reduce the local magnetic moment at the nearest-neighboring transition metal atoms.

In summary, in this thesis a large number of defects is studied in a variety of compounds that are of utmost importance to nanoscience; the lead chalcogenides PbS, PbSe, and PbTe that are frequently used in quantum dots, 2D monolayers of tungsten disulfide WS_2 which belong to the class of stackable van der Waals solids, and finally atomically flat 2D monolayers of the early transition metal oxides (TMOs, with TM=Sc, Ti, V, Cr, Mn) which exhibit hitherto unknown magnetism and conductivity. All of these investigations show how strongly the materials properties are affected by

the presence of defects, giving rise to e.g. additional electronic states in the band gap of semiconductors, defect-induced magnetism, and strong spin-orbit coupling effects, which are not or to a much lesser extent present in defect-free nanomaterials. Whereas defects in popular bulk materials are at present reasonably well documented, defects in low-dimensional materials are still a very open field of investigation, and the results described in this thesis show how interesting and promising the physics of defects can and will be for the future development of nanoscience.

Samenvatting

Met de stormachtige vooruitgang in de wetenschap en de technologie van materialen met nano-afmetingen, komen steeds meer nieuwe fysische verschijnelen aan het licht die vedere verkenning behoeven. Dichtheidsfunctionaaltheorie (DFT), een krachtig theoretisch gereedschap dat als werkpaard dient voor elektronische struktuurberekeningen van periodieke systemen, is een bewezen methode en wordt in toenemende mate toegepast om de natuurkundige eigenschappen van nieuwe nanomaterialen bloot te leggen, te begrijpen, en zelfs te voorspellen. Tegelijkertijd komen, voortvloeiend uit de tweede wet van thermodynamica, puntdefecten veelvuldig voor in nanokristallen. Deze puntdefecten breken niet alleen de translatiesymmetrie, maar bepalen ook de fysische eigenschapen en de technologische prestaties van het gastheermaterial. Dit proefschrift is gewijd aan het verkennen van de rol van verschillende soorten puntdefecten in nanomaterialen, zowel tweedimensionaal (2D) en driedimensionaal (3D), gebruik makend van DFT. Deze verkenning begon bij de puntdefecten in 3D loodchalcogeniden (PbX, X=S, Se, Te), werd vervolgd met de spin-orbit (SO) splitsing van de defecttoestanden in WS_2 monolagen (ML), behorend tot de familie van 2D overgangsmetaaldichalcogeniden (TMDs), en eindigde met het voorspellen van nieuwe 2D monolaag (ML) structuren voor overgangsmetaaloxiden (TMOs, met TM=Sc, Ti, V, Cr, Mn).

In Hoofdstuk 3 wordt de systematische bestudering beschreven van de geometrie, energetica, en elektronische kenmerken van puntdefecten in PbX halfgeleiders met behulp van DFT. De soorten puntdefecten omvatten de monovacatures, interstitiëlen, Schottky defecten (paren van kation - anion vacatures), en Frenkel (kation of anion vacature plus interstitiëel). De monovacatures en Schottky defecten zijn energetisch voordeliger, hetgeen wat blijkt uit hun lagere vormingsenergie. Voor fotoluminescentietoepassingen wordt voorspeld dat de lood monovacature (V_{Pb}) een lage acceptor is, die waarschijnlijk radiatieve recombinatie mogelijk zal maken. De zwavel monovacature (V_S) genereert daarentegen een diepe donor toestand die de geleidingsgaten zal vangen in p-type PbX, waardoor ook de fotoluminescentieopbrengst zal verminderen. Wat afwijkende stoichiome-

trie betreft, alhoewel de vormingsenergie van V_{Pb} kleiner is dan die van V_X voor alle PbX systemen, impliceren resultaten van de berekeningen dat een overschot aan anionen gemakkelijker kan worden ingebed dan een overmaat aan kationen. De defect-energieën van beide defectsoorten zijn echter nogal hoog, wat afwijkende stoichiometrie ongunstig maakt. Mogelijk wordt fasescheiding belemmerd door een nucleatiebarrière voor de vorming van zuivere Pb en X fasen. In het geval van een nanokristal kan een deel van de afwijkende stoichiometrie worden geaccommodeerd aan het oppervlak. Dit hangt ook af van het type gebruikte liganden. Alle defect-vormingsenergieën overziend, hebben Schottky defecten een aanzienlijk lagere vormingsenergie dan de kation en anion monovacatures. Daarom is het duidelijk dat de Schottky defecten een veel belangrijkere rol kunnen spelen in het kationenuitwisselingsproces van PbSe-CdSe heteronanokristallen (HNCs) dan tot dusver wordt verondersteld. Vanwege de enorme verplaatsingen van dichtstbijzijnde-naburige (NN) atomen rond interstitiëel-type defecten, zijn anion en kation interstitiëlen en Frenkel defecten minder gunstig. Het resultaat van lokale relaxatie toont aan dat de uitbreiding of inkrimping van de NNs van een defect positie het netto resultaat is van de elektrostatische interactie tussen de atomen in de lokale omgeving. Uit Bader-lading analyse is gebleken dat de mate van ladingsoverdracht afneemt in overeenstemming met de trend van de elektronegativiteit. Tweedimensionale plots van verschillen in ladingsdichtheid geven aan dat de ladingsdichtheid rond de defectpositie lokaal is gepolariseerd, en dat er electride-achtig gedrag is met gevangen lading die aanwezig is op de positieve anionvacature. Het werk dat wordt besproken in Hoofdstuk 3 representeert een rijke verscheidenheid aan fysische eigenschappen die geïntroduceerd worden door defecten in de PbX halfgeleiderfamilie, met directe implicaties voor de synthese en de fysische eigenschappen van PbX-bevattende HNCs. In toekomstig werk kan de huidige studie uitgebreid worden naar geladen defecten, en de berekening van energiebarrières voor de migratie van vacature-type defecten.

In Hoofdstuk 4 wordt de energiesplitsing van defecttoestanden als gevolg van spin-orbit koppeling (SOC) in 2D wolfraamdisulfide (WS_2) monolagen (MLs) kwantitatief gekarakteriseerd met behulp van DFT en de hybride functionaal geformuleerd door Heyd, Scuseria en Ernzerhof (HSE). Van alle puntdefecten hebben de zwavel monovacature (V_S) en de zwavelinterstitiëel (I_S) de laagste vormingsenergieën. Naast V_S en S_i; werden twee andere soorten anti-positie defecten (W_S en W_{S2}) ook geselecteerd voor onderzoek naar de SO bandsplitsing van de defecttoestanden, omdat eerder in de literatuur is gerapporteerd dat deze anti-positie defecten een aanzienlijk magnetisch moment kunnen hebben. We hebben aangetoond dat de SO splitsing afhankelijk is van zowel de orbitale samenstelling als van de richting van de magnetisatie van de defecttoes-

tanden. De toestanden die een d_{xy} en $d_{x^2y^2}$ karakter hebben zullen een significante SO splitsing ondergaan als de magnetisatie is georiënteerd langs de m_z magnetisatie-as. De grootste SO splitsing treedt op bij het Ws anti-positie defect, en deze sterke SO splitsing van 296 meV (356 meV door HSE) is vergelijkbaar met die in defect-vrije WS_2. Voor S_i werd geen splitsing gevonden omdat deze defecttoestand uitsluitend is samengesteld uit d_{z^2} en p^z orbitalen. Afgezien van de SO splitsing, hebben de berekeningen ook bevestigd dat zowel de W_S als de W_{S2} anti-positie defecten een lokaal magnetisch moment hebben van 2 μ_B gelokaliseerd op het anti-positie W atoom, door twee ongepaarde spin-up elektronen in de d_{xy} en $d_{x^2-y^2}$ defecttoestanden. Daarmee vormt het anti-positie W atoom samen met de eerste en tweede dichtstbijzijnde naburige W atomen een zogenaamd 'superatoom'.

In Hoofdstuk 5 wordt beschreven hoe DFT en HSE werden gebruikt om materialen met daarin overgangsmetalen (TM) te bestuderen. In het bijzonder zijn de 2D overgangsmetaaloxiden (TMOs) onderwerp van studie, waarbij de TM atomen de vroege 3d overgangsmetalen zijn: Sc, Ti, V, Cr, Cr en Mn. Op basis van de verscheidene valenties die de TM atomen kunnen hebben, is logischerwijs gekomen tot het construeren van vier plausibele configuraties voor de 2D atomair dunne kristalstruktuur van de vijf TMO fasen. Deze structuren zijn: hexagonaal MO (*h*-MO, waarbij M staat voor het overgangsmetaalelement), keukenzout MO (*rs*-MO), hexagonaal M_2O_3 (h-M_2O_3), en kubisch MO_2 (c-MO_2). De energie van de grondtoestand, de geometrische struktuur en de magnetische ordening van elke 2D TMO fase werden bepaald. De relatieve stabiliteit van alle 2D TMOs werd geëvalueerd in termen van de vormingsenergie per atoom. Het bleek dat de hexagonale M_2O_3 fase de meest stabiele fase is onder alle 2D TMO fasen ten opzichte van de elementaire TM bulkfase en het paramagnetische zuurstofmolecuul. Voor drie van de vijf *h*-MO fasen is een geribbelde struktuur voordeliger. We hebben ook de relatieve stabiliteit van elke 2D TMO geëvalueerd ten opzichte van hun 3D tegenhangers met dezelfde stoichiometrie. Deze vergelijking heeft aangetoond dat drie van de vijf *rs*-MO fasen stabieler zijn dan hun bulk tegenhanger, hetgeen sterk suggereert dat gedurende groei door middel van depositie, het materiaal waarschijnlijk tot een vlakke 2D dunne film groeit in plaats van tot een 3D nano-eiland op het substraat. We hebben er ook op gewezen dat door het kiezen van een geschikt substraat, het zeer waarschijnlijk mogelijk is om deze 2D TMOs experimenteel te synthetiseren. De berekeningen laten verder zien dat deze 2D TMOs een breed scala aan electronische en magnetische eigenschappen hebben. Deze fasen gedragen zich als semimetalen, half-metalen, en als halfgeleiders met verschillende magnetische orderingen waaronder niet-magnetische, ferromagnetische, en antiferromagnetische. Deze spectaculaire verscheidenheid van magnetische

en elektronische eigenschappen geeft aan dat deze nieuwe 2D TMOs een groot potentieel hebben voor toekomstige toepassingen in elektronische en spintronica-gerelateerde gebieden. Verder zijn ook vacatures van overgansmetaalatomen (V_{TM}) onderzocht in de *h*-M_2O_3 fase, die de laagste formatie-energie hebben van alle 2D TMO fases. Afgezien van V_{Sc}@*h*-Sc_2O_3, hebben alle V_{TM}'s een vrij lage formatie-energie bij lage zuurstof druk, en zullen zelfs het materiaal als geheel stabilizeren bij lage zuurstof druk. Deze vacatures, behalve V_{Sc}, zullen ook het lokale magnetisch moment bij de dichst-naburige overgangsmetaalatomen verminderen.

Samengevat, een groot aantal defecten waren bestudeerd in een verscheidenheid van verbiendingen die van het grootste belang zijn voor de nanowetenschappen; de loodchalcogenides PbS, PbSe, en PbTe die vaak gebruikt worden in quantum dots, 2D monolagen van wolfraamdisulfide WS_2 die tot de klaase van stapelbare van der Waals vaste stof behoren, en eindelijk de atomair vlakke 2D monolagen van de oxiden van de vroege overgangsmetalen (TMOs, met TM=Sc, Ti, V, Cr, Mn) die tot dusverre onbekend magnetisme en geleidbarrheid vertonen. Al deze onderzoeken laten zien hoe sterk de materieaaleigenschappen worden beïnvloed door de aanwezigheid van defecten, die leiden tot bij voorbeeld extra elektronische staten in de band gap van halfgeleiders, defect-geïnduceerde magnetisme, en sterk spin-orbit koppeling effecten die zijn niet of in een veel mindere mate aanwezig in foutloze nanomaterialen. Hoewel de defecten in populaire bulkmaterialen zijn op dit moment al redelijk goed gedocumenteerd, defecten in laag-dimensionale materialen zijn nog steeds een heel open gebied van onderzoek, en de resultaten beschreven in dit proefschrift tonen aan hoe interessant en veelbelovend de natuurkunde van defecten kan en zal zijn voor de toekomstige ontwikkeling van nanowetenschappen.

Appendices

Appendix A

Supplemental Information of Chapter 3

A.1 Introduction

In this Appendix, we include the charge density difference of Schottky pair defects, and the detailed results of electronic structure calculations for V_{Pb}, V_X, the Schottky dimer and the Schottky pair.

A.2 Charge density difference of Schottky pair defects

The charge density difference of the Schottky pair is shown in Fig. A.1. Due to the distant separation of the two vacancies, V_{Pb} and V_X in the Schottky pair configuration can be regarded as isolated vacancies and do not interact much with each other. Thus the pattern is very similar to those of the single V_{Pb} and V_X defects. But in the case of the Schottky pair, the charge polarization around V_X is stronger than around the V_X monovacancy, (Fig. 4 (i)–(l) in the main text).

A.3 Electronic structure

We first discuss the electronic structure of perfect PbX systems before introducing the defect states. Since the electronic structures of PbS, PbSe and PbTe are similar (see for instance, the band structures of PbX calculated in Ref. 97), we use PbS as an example to describe the characteristics of the electronic structures of perfect PbX crystals. The band structure, total density of states (TDOS), and projected density of states of the Pb atom

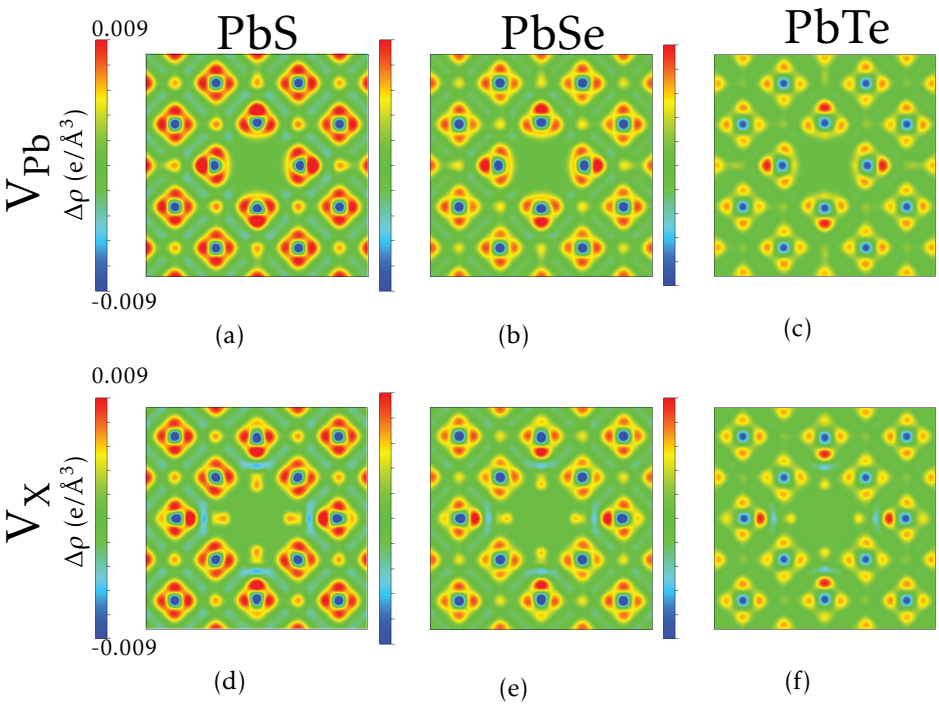

Figure A.1: Charge density difference of PbX containing a Schottky pair. Color red denotes charge accumulation, and color blue for charge depletion. The cross-section is the (100) plane for each system.

and the S atom of primitive PbS are presented in Fig. A.2. For a clearer description of the position of the bands, the Fermi level is set as zero energy. The band structure and DOSs can be categorized into three parts: semicore, valence, and conduction bands. In the semicore region, we have the S 3*s* state at -12 eV to -13.5 eV. In the valence window, we first have the Pb 6*s* state located at -9 eV to -6 eV. From -5 eV to VBM, the S 3*p* states overlap with mainly the Pb 6*p* states and the 6*s* state. It is noteworthy that the Pb 6*s* state is split into two peaks, one located at the bottom of the valence region, and one at the top, with an energy gap of around 3 eV. This is attributed to the interaction between the Pb 6*s* state and S 3*p* states, and corresponds respectively to the bonding and anti-bonding orbitals of these two states. The conduction bands are mainly composed of the Pb 6*p* states, with a slight overlap with the S 3*p* states. Therefore, it is expected that the defect states appearing in the band structures are related to the defect-induced perturbation of the Pb *s* and *p* states and the S *p* states.

The electronic structures studied are the V_{Pb}, V_O, Schottky dimer and Schottky pair defects. The considered band structures of PbX are along the

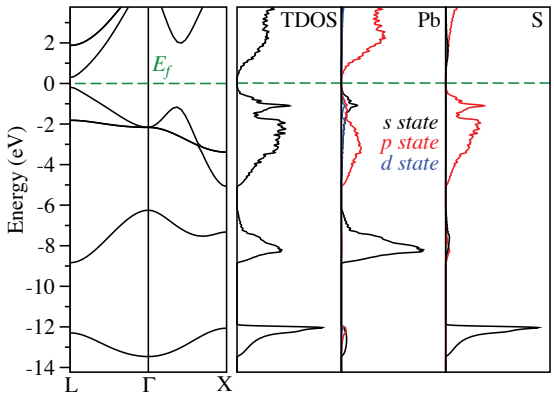

Figure A.2: Band structure, total DOS (TDOS), and projected DOS of Pb atom and S atom of the PbS primitive cell. Fermi level is shifted to energy origin and is indicated as the dark green dashed line.

L→ Γ →X direction in the Brillouin zone. The DOS plots show the band gap region. Band structures are displayed in Fig. A.3 to Fig. A.6, and DOSs in Fig. A.7 and Fig. A.8. The DOS of defective systems are more smeared comparing to the ones of perfect systems. This is because the presence of defects leads to additional dispersion. One remarkable observation is that only the V_X states cause a significant change in the electronic structure of PbX systems; V_{Pb} hardly modifies the original band structures. This finding echoes Slater's statement which said that in alkali halides the valence band and conduction band are dominated by the anion *p* states and *s* states, respectively[229,230]. In other words, the chemical properties of alkali halide systems is determined by the anions. When comparing with Fig. A.2, it is clear that at the top of valence band and at the bottom of conduction band, there are significant contributions from the Pb *p* and *s* states, and Slater's finding still applies to the partially-ionic PbX systems as the S *p* states also participate largely in the VBM region and partly in the conduction band.

In order to visualize more clearly the electron distribution of the defect states, the partial charge density corresponding to the defect states were also calculated and are plotted in Fig. A.9 for V_{Pb} and V_X, and in Fig. A.10 for the Schottky dimer and Schottky pair configurations.

Concerning the band structure of the PbX systems, we need to note two facts: 1) the symmetry of the system is broken because due to the presence

of defects, thus the dispersion curves are changed. 2) In our calculations, the concentration of defects is around 0.5%, which is still considerably higher than the real concentration in experimental conditions. As a result, the defect states are rather dispersive. Because of these two concerns, we consider mainly the band structure at the L point.

V_{Pb}

By combining Fig. A.3 and A.7, one can see the electronic structure change of PbX upon the presence of V_{Pb}. The presence of the defect causes a downward shift to the Fermi levels such that the Fermi levels pass through the VBM. The location of the V_{Pb} defect state at the L point is beyond the Fermi level. Based on the projected wave function analysis, we found that the V_{Pb} defect states at the L point have zero occupancy, thus they are p-type defect states consisting of two holes. The wave function analysis also shows that this defect state is composed of three degenerate states, and each of these states have some Pb s character, and p character from the X atoms. Furthermore, the three X p states interacting with the Pb s state have the same magnitude, reflecting the spherical symmetry of the Pb 5s state which interacts with the p_x,p_y and p_z orbitals of X atoms to the same extent. The partial charge density of V_{Pb} is shown in Fig. A.9, and the s-p interaction is also confirmed as the NN X p charge density and the NNN Pb s charge density are both polarized towards each other. However, the results of Ref. 86 and 88 for V_{Pb} in PbTe only attribute the V_{Pb} state to the 5p orbitals of the NN Te atoms.

V_X

In Figures A.4 and A.8, one can see the electronic structure change of PbX due to the presence of V_X. Contrary to the V_{Pb} states, V_X will cause Fermi levels to undergo an upward shift. For PbS and PbSe, the Fermi level penetrates the VBM, while for PbTe, the Fermi level is shifted to above the VBM. The wave function analysis shows that the occupancy of the V_X defect state is a singlet doubly occupied state, with two electrons coming from NN Pb p orbitals, as shown in Fig. A.9. This makes the V_X n-type. Our results are in good agreement with the results of Ref. 86 and[88].

Schottky dimer and Schottky pair

Schottky dimer and Schottky pair systems give rise to both V_{Pb} and V_X defect states. In these two cases, the Fermi level is almost fixed at the original position because of the presence of V_{Pb} and V_X. This is Fermi level pinning, where the two electrons at the V_X state and the two holes at V_{Pb} are present in combination. As a result, the Fermi level is pinned at

the original place because of the unchanged net carrier concentration. The wave function analysis confirms the argument that in the Schottky defects, the two electrons originally occupying the V_X state are now transferred to the V_{Pb} state.

It is noteworthy that with decreasing inter-vacancy distance, the position of the V_X state shifts closer towards the CBM. That is, if we define $\Delta E = E(CBM) - E(V_X)$, then $\Delta E(V_X) > \Delta E(\text{Schottky pair}) > \Delta E(\text{Schottky dimer})$.

We present the partial charge density for the V_{Pb} and V_X states in Schottky configurations in Fig. A.10. The partial charge densities for V_{Pb} and V_X in the Schottky pair are identical to their counterparts in perfect PbX systems. This implies that there is not a significant interaction between the two vacancy sites. However, the picture of the Schottky dimer is more complex because of the interaction between the next-neighbor V_{Pb} and V_X vacancies. For V_{Pb} in the Schottky dimer, the charge density located on the NN X atoms is polarized towards the V_X site (which also confirms that now the V_X site is electron deficient). At the V_X site, the charge density from the V_{Pb} site is lacking. And the charge density at the NN Pb atoms of V_X is slightly polarized toward the V_{Pb} site.

For all the four aforementioned defect configurations, the degree of charge redistribution is inversely proportional to the size of X anions; the larger the X anion, the less its electronegativity, thus less the charge redistributes. This finding echoes the discussion we gave in the main text.

A.4 Derivation of the free energy

The number of configurations at thermal equilibrium Ω is defined as

$$\Omega = \frac{n!}{n_d!(n-n_d)!}, \tag{A.1}$$

where n is the the total number of atoms and, n_d is the number of defects. The entropy of the system is given by

$$S = k_B \ln \Omega, \tag{A.2}$$

After substituting Eq. A.1 into Eq. A.2, and defining $x_d = \frac{n_d}{n}$ as the equilibrium defect concentration, we obtain the expression of entropy S in terms of x_d

$$S = -k_B n(x_d \ln x_d + (1-x_d)\ln 1 - x_d), \tag{A.3}$$

The free energy is defined as

$$F = U - TS, \tag{A.4}$$

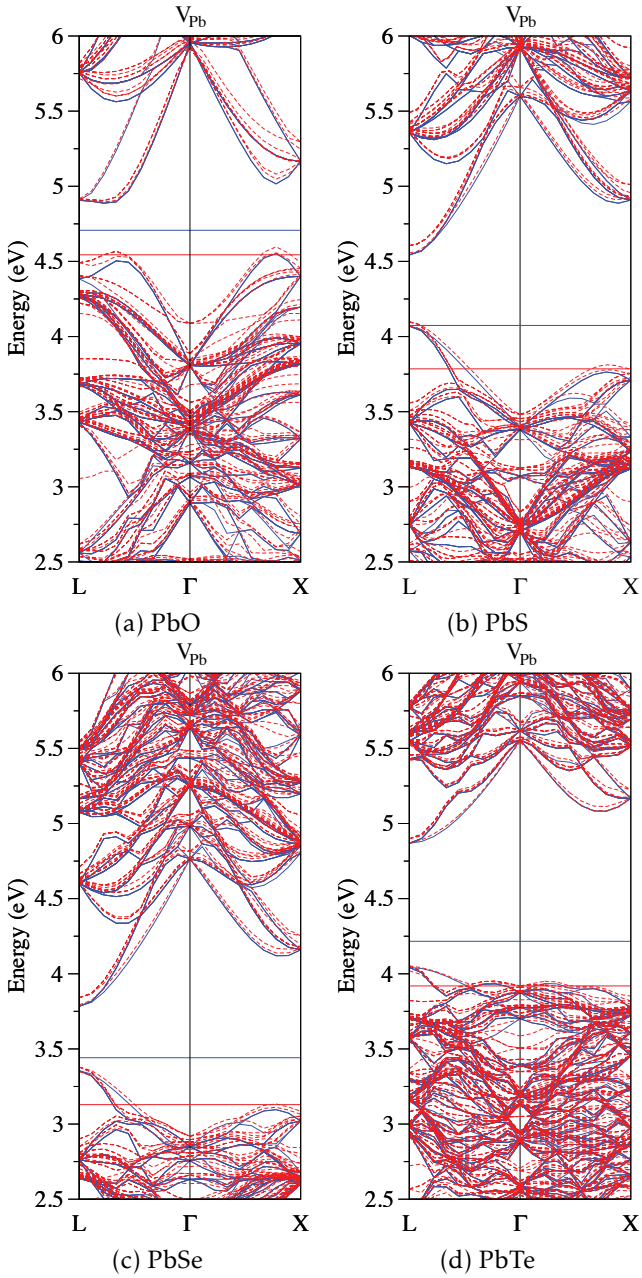

Figure A.3: Band structure of PbX supercells containing a V_{Pb}, as shown in red dotted lines. Band structure of perfect PbTe is shown in dotted blue lines. The solid red and solid blue lines are Fermi levels of the defective and perfect supercells, respectively.

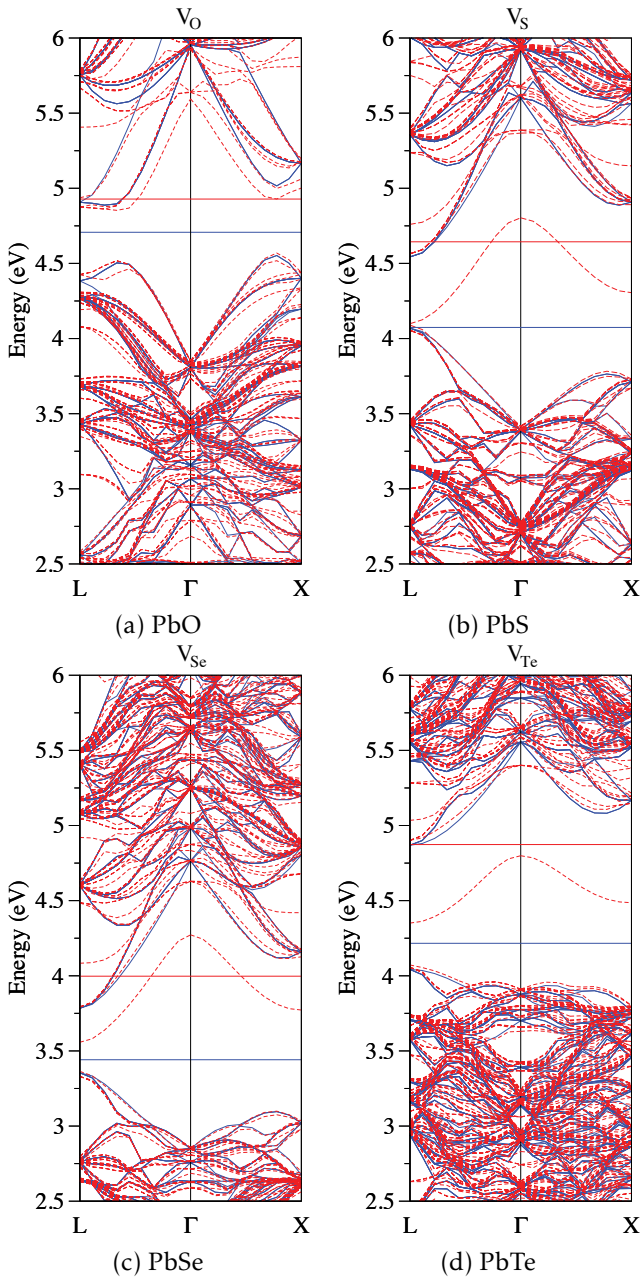

Figure A.4: Band structure of PbX supercells containing a V_X, as shown in red dotted lines. Band structure of perfect PbTe is shown in dotted blue lines. The solid red and solid blue lines are Fermi levels of the defective and perfect supercells, respectively.

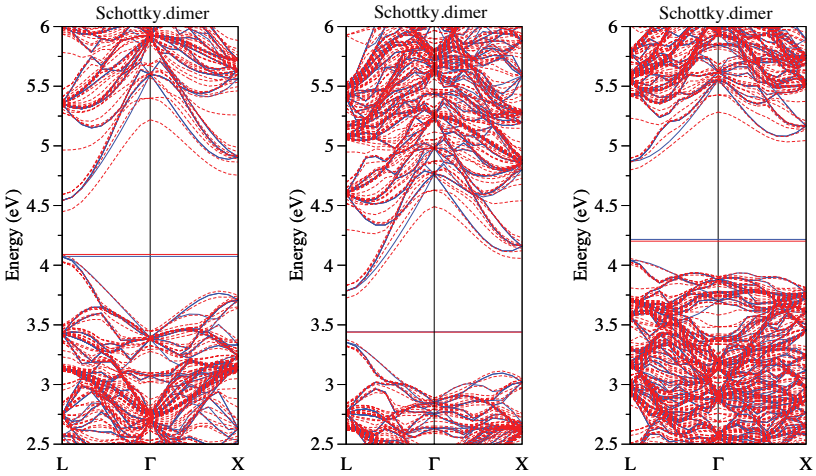

(a) PbS (b) PbSe (c) PbTe

Figure A.5: Band structure of PbX supercells containing a Schottky dimer, as shown in red dotted lines. Band structure of perfect PbTe is shown in dotted blue lines. The solid red and solid blue lines are Fermi levels of the defective and perfect supercells, respectively.

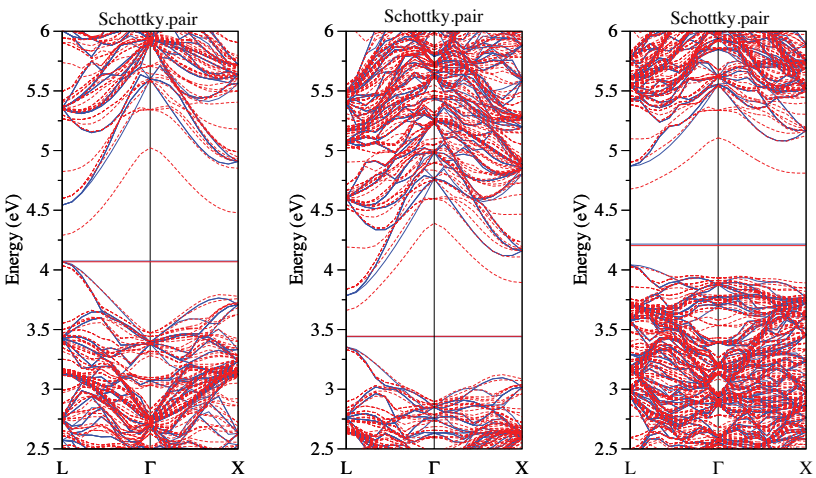

(a) PbS (b) PbSe (c) PbTe

Figure A.6: Band structure of PbX supercells containing a Schottky pair, as shown in red dotted lines. Band structure of perfect PbTe is shown in dotted blue lines. The solid red and solid blue lines are Fermi levels of the defective and perfect supercells, respectively.

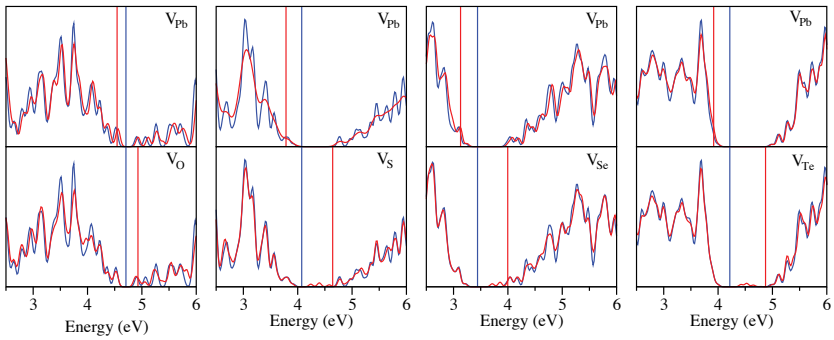

(a) PbO (b) PbS (c) PbSe (d) PbTe

Figure A.7: Density of states (DOS) of PbX supercells containing a Pb vacancy or a X vacancy. The red dotted curve and blue dotted curve are DOS of defective supercells and perfect supercells, respectively.

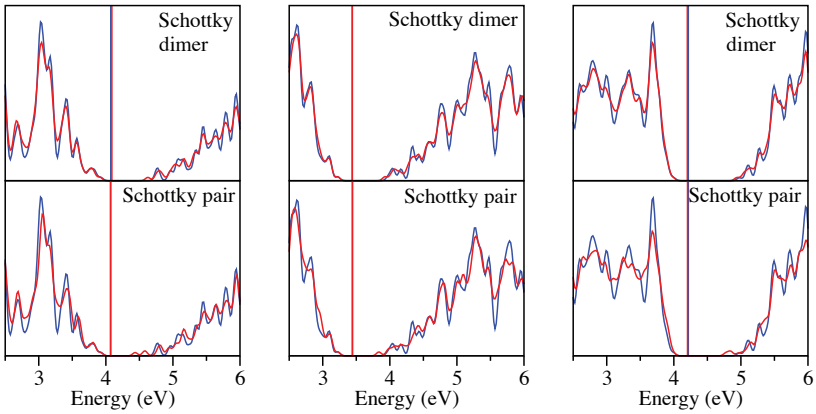

(a) PbS (b) PbSe (c) PbTe

Figure A.8: Density of states (DOS) of PbX supercells containing a Schottky dimer or a Schottky pair. The red dotted curve and blue dotted curve are DOS of defective supercells and perfect supercells, respectively.

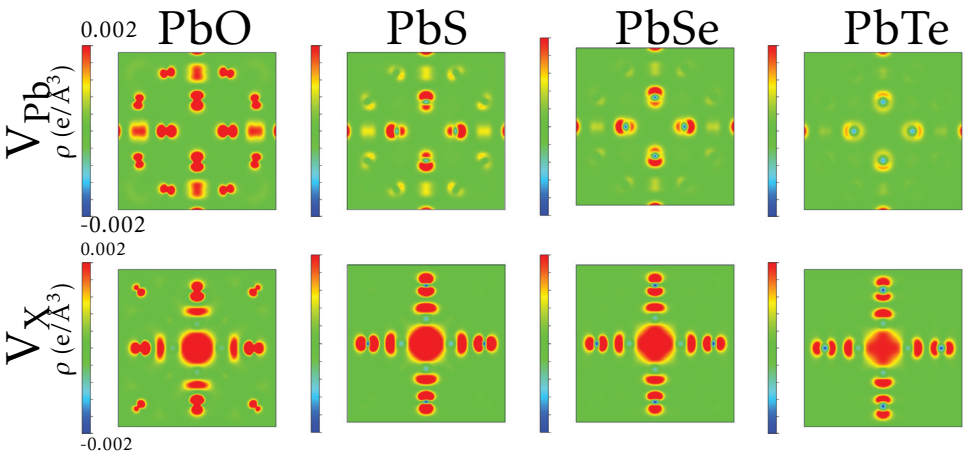

Figure A.9: Partial charge density of the defect states at L point of V_{Pb} and V_X of PbX. Color red denotes charge accumulation, and color blue for charge depletion. The cross-section is the (100) plane for V_{Pb}, and (001) for V_X. The band of the defect state was specifically selected

where U is the enthalpy, and T is temperature in K. At pressure of zero Pa, U is equal to the sum of the formation energy of every defect, $n_d E_d$. Thus, Eq. A.4 can be rewritten as

$$F = n_d E_d + n k_B T [X_d \ln X_d + (1 - X_d) \ln (1 - X_d)]. \tag{A.5}$$

Finally, the free energy per atom f is

$$f = \frac{F}{n} = x_d E_d + k_B T (x_d \ln x_d + (1 - x_d) \ln(1 - x_d)). \tag{A.6}$$

Hence, by determining the x_d for which f is at the minimum, the equilibrium defect concentrations at different temperatures can be found.

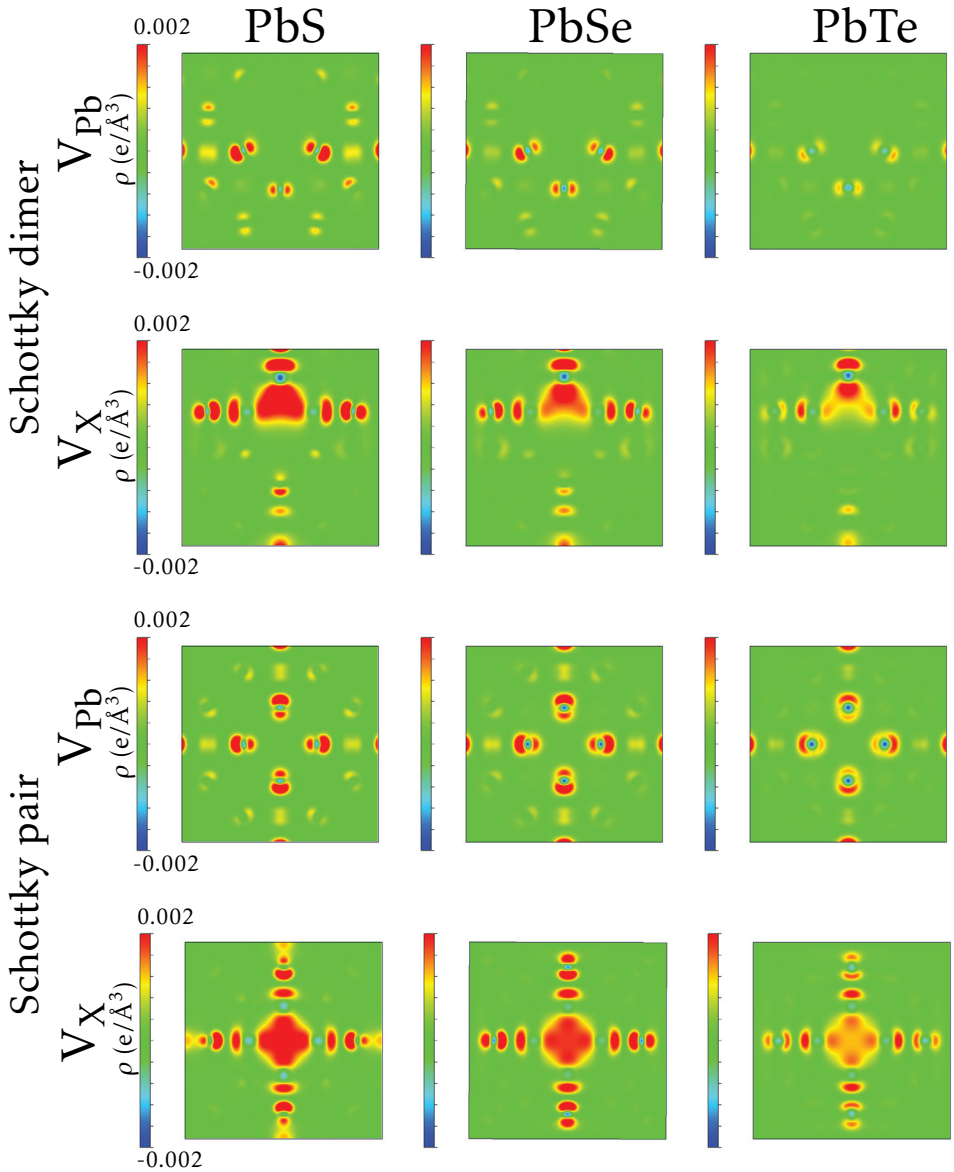

Figure A.10: Partial charge density of the V_{Pb} and V_X defect states at L point for Schottky dimer and Schottky pair defects in the PbX systems. Color red denotes charge accumulation, and color blue for charge depletion. The cross-section is (100) for all the systems.

Appendix B

Supplemental Information of Chapter 4

B.1 vdW and SOC

These series of calculations were originally meant to include the bulk WS_2 as well, for which the van der Waals (vdW) force should be considered to address the inter-layer interaction. For this, we compared several vdW correction schemes available in VASP, and found that the vdW density functional[231] optB88-vdW[164] gave us the most accurate inter-layer separation of 12.546 Åcompared to experiment (12.323 Å). Therefore we decided to use the optB88-vdW.

As there is an incompatibility between the optB88-vdW functional and the non-collinear calculations in VASP, we had to include the vdW correction and the SOC effect in different steps. We fist performed the geometry relaxation, and then calculate the total energy with only the vdW correction being included. In the end, we turned off the vdW correction and calculated the electronic properties of the relaxed structure with only the SOC effect included. We used this separation scheme because we tested and found that vdW only affects the geometry but not the electronic properties of the mateiral, while SOC only affects the electronic properties but not the geometry.

B.2 Density of States

Fig. B.1 presents the total DOS of all the ML WS_S slabs in order to show the SO splitting of the defect states.

Fig. B.2 compares the DOS of the NSP and SP W_S-WS_2 and W_{S2}-WS_{S2} as well as the projected DOS (PDOS) of each orbital. The purpose of this

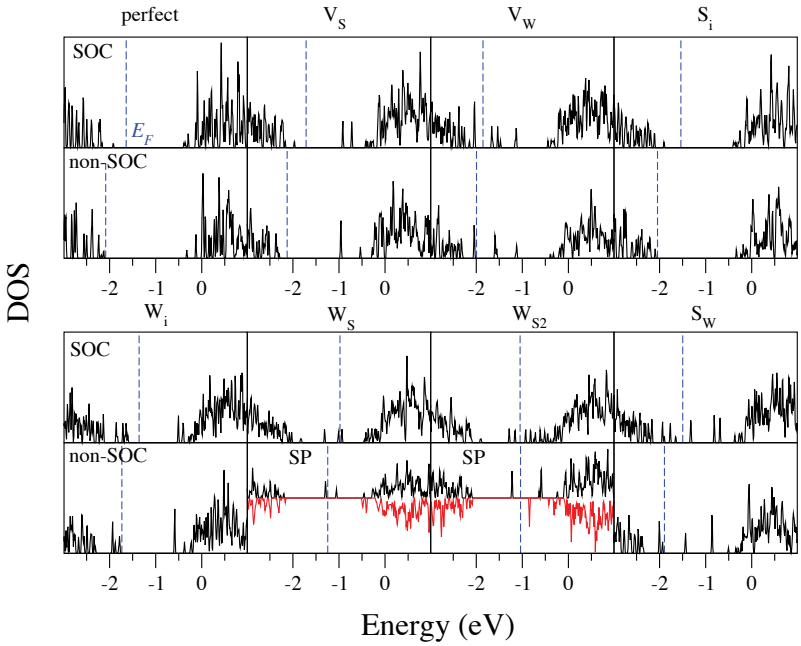

Figure B.1: Total DOS of all the ML WS_2 slabs considered in this study. Only the W_S and W_{S2} antisite defects are shown to be spin-polarized, thus they have both spin-up (black) and spin-down (red) DOS. Fermi level is indicated as the dashed blue lines.

Figure is to allow us to trace back the origin of the magnetic moment existing in SP W_S-WS_2 and W_{S2}-WS_{S2}. In each plot, the total density of states (TDOS) is shown on top, followed by the DOS projected onto the S *p* orbitals and the five W *d* orbitals. The contribution of the *d* orbitals of the antisite W atom is also plotted and compared to all other W atoms. Fig. B.2 (a) and (c) show that the defect state under the Fermi level is mainly composed of the d_{xy} and $d_{x^2-y^2}$ orbitals of the defect W atom. Fig. B.2 (b) and (d) further prove that this defect state is spin-polarized (spin-up) and therefore it bears the magnetic moment.

B.3 Orbital decomposed charge densities of the band structures of perfect bulk and ML WS_2 unitcells

Fig. B.4 and B.5 provide the orbital decomposed charge densities of the band structures of perfect bulk and ML WS_2 unitcells. These Figures are to illustrate the crystal field splitting of the bands.

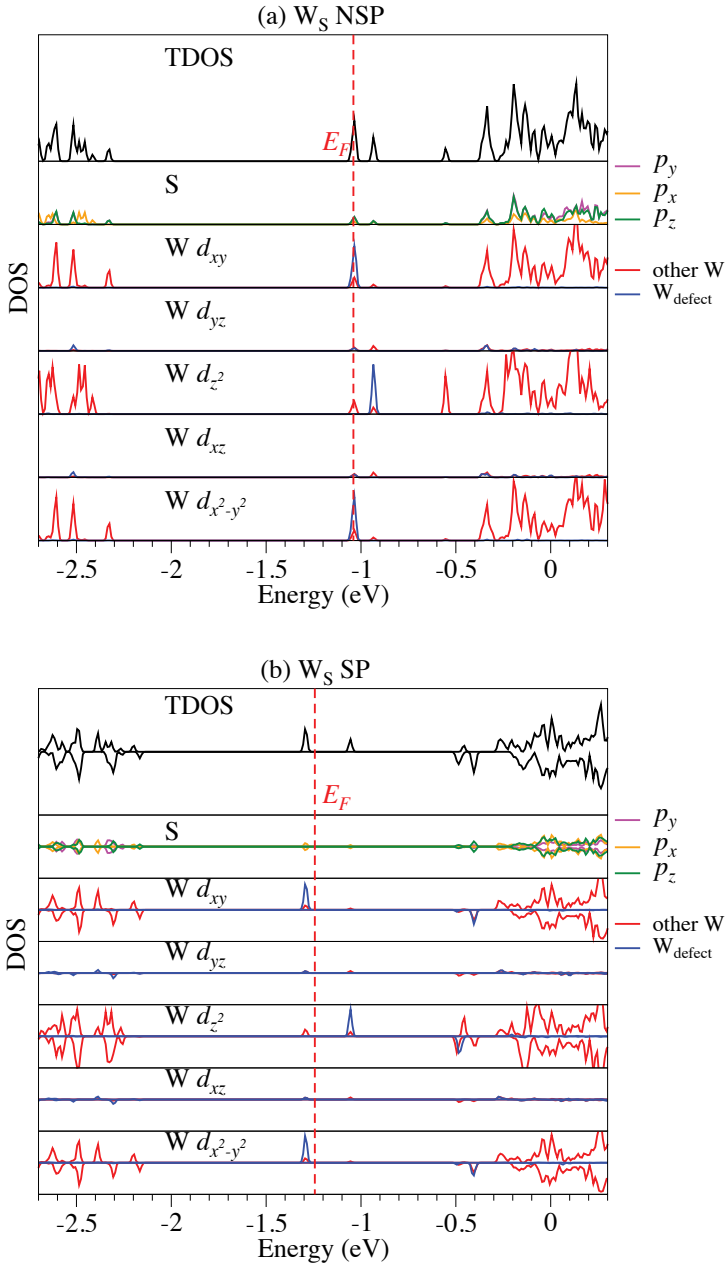

Figure B.2: TDOS and PDOS plots for both the non-spin-polarized (NSP) and spin-polarized (SP) W_S and W_{S2} antisites. PDOSs are enlarged 10 times to make them visually comparable to TDOSs.

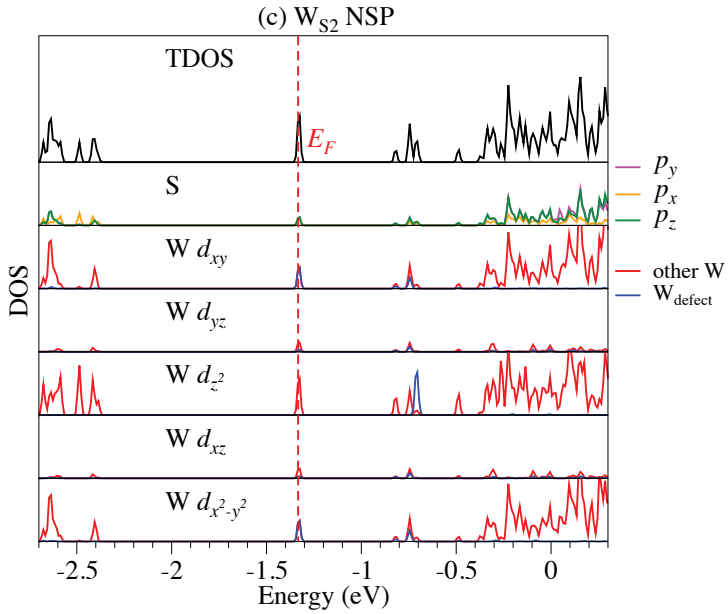

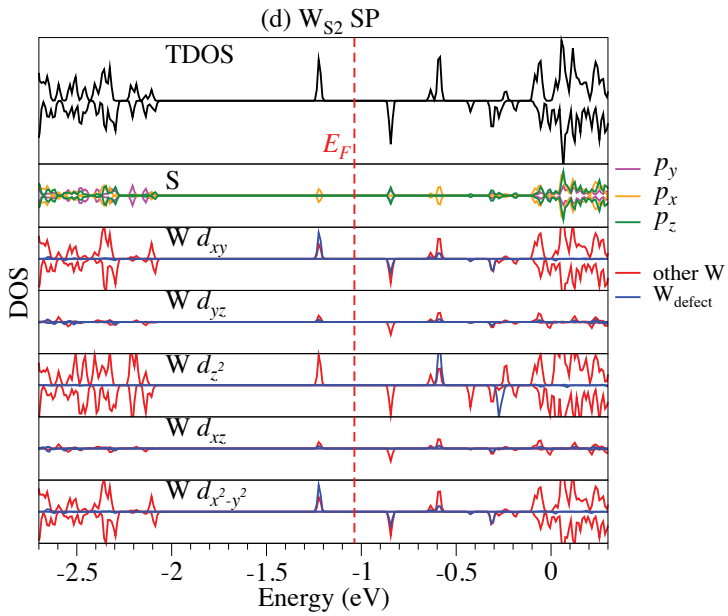

Figure B.3: Continued.

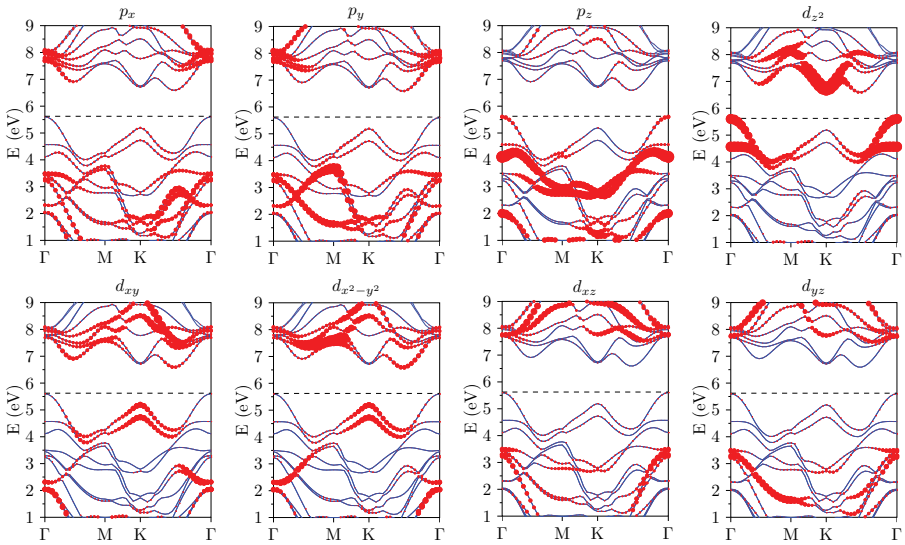

Figure B.4: Orbital decomposed BSs of bulk WS_2 unitcell.

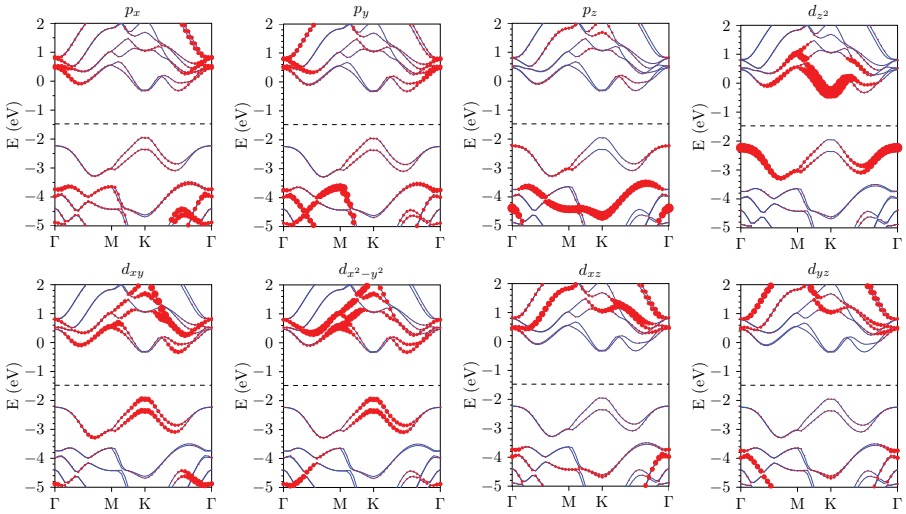

Figure B.5: Orbital decomposed BSs of ML WS_2 unitcell. The W *d* orbitals are split due to the crystal field effect.

B.4 Orbital decomposed band structures of perfect and defective ML WS_2 supercells

This series of figures show that the defect states are composed of either the d_{z^2} orbital or $d_{xy} + d_{x^2-y^2}$.

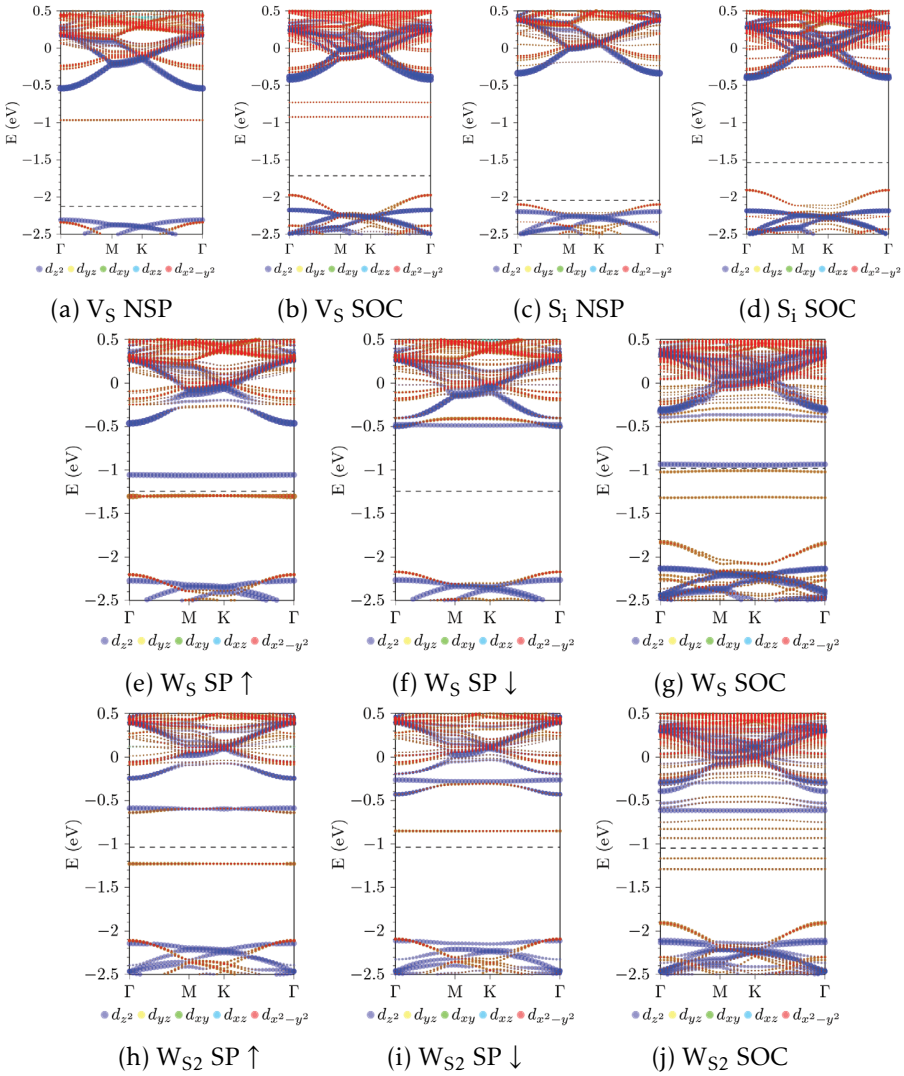

(a) V_S NSP (b) V_S SOC (c) S_i NSP (d) S_i SOC

(e) W_S SP ↑ (f) W_S SP ↓ (g) W_S SOC

(h) W_{S2} SP ↑ (i) W_{S2} SP ↓ (j) W_{S2} SOC

Figure B.6: The band structures of all the ML WS_2 slabs considered in this study. The bands are decomposed in terms of the five d orbitals of the W atoms. The brownish color indicates the mixture of the d_{xy} (green) and $d_{x^2-y^2}$ (red) orbitals.

Appendix C

Supplemental Information of Chapter 5

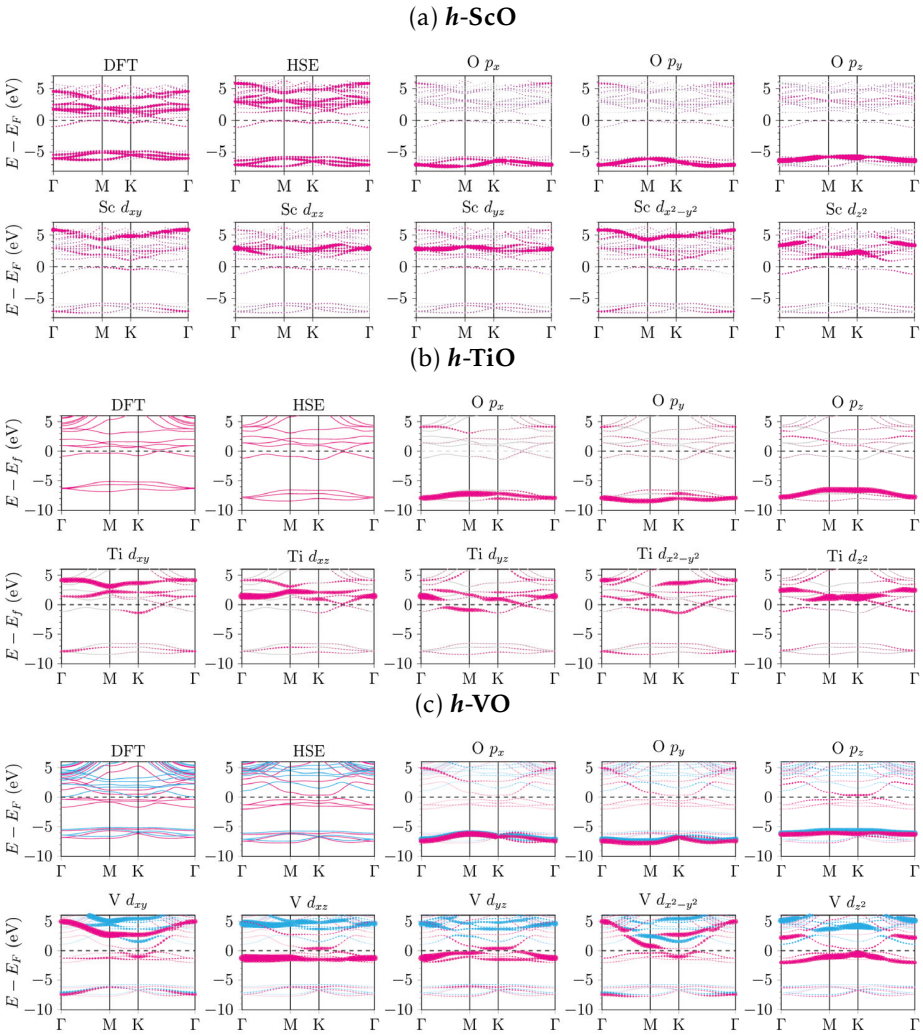

Figure C.1: The HSE orbital resolved band structures at the magnetic ground state of every 2D TMO chosen in this study. For spin-polarized band structures, spin-up bands are colored in pink, and spin-down bands in cyan. The purple color appears because of the overlap of spin-up and spin-down bands. The DFT total band structures are also included for comparison.

(d) ***h*-CrO**

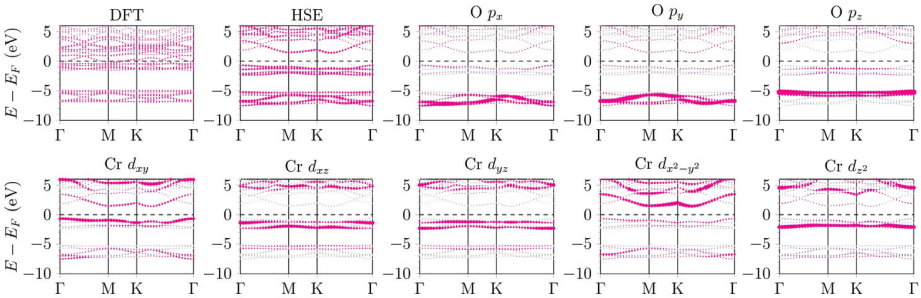

(e) ***h*-MnO**

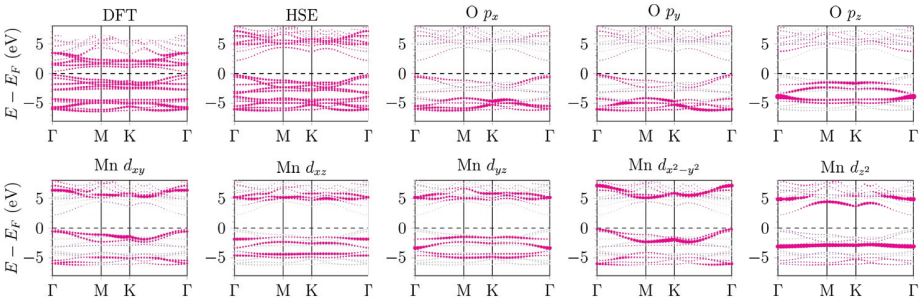

(f) ***rs*-ScO**

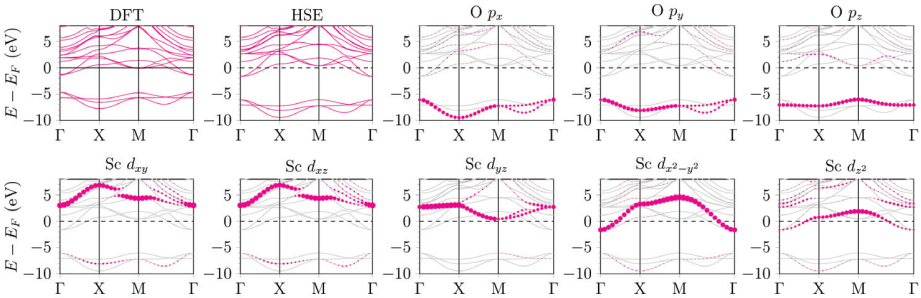

(g) ***rs*-TiO**

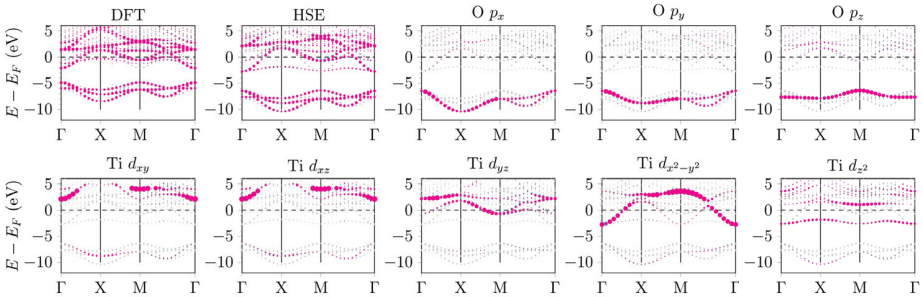

(h) ***rs*-VO**

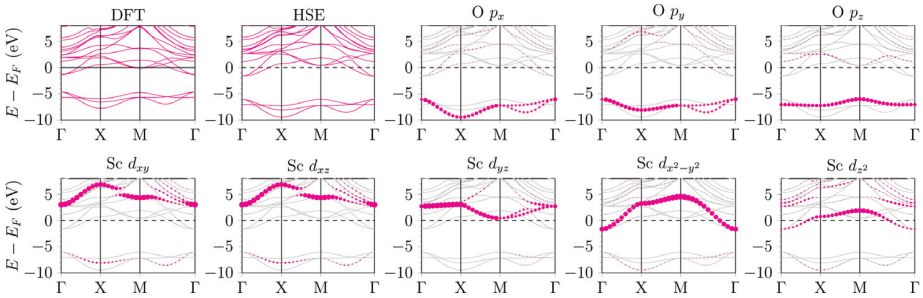

(i) ***rs*-CrO**

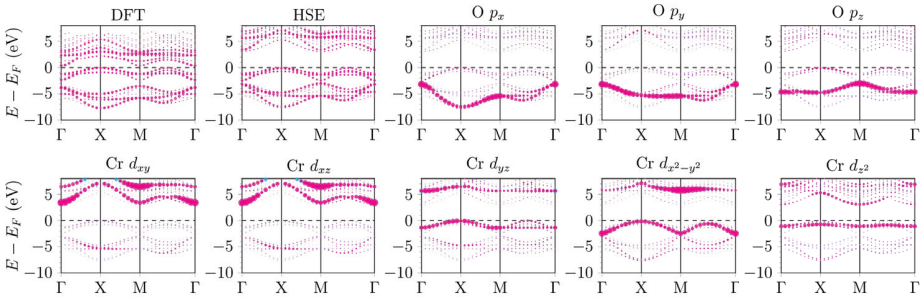

(j) ***rs*-MnO**

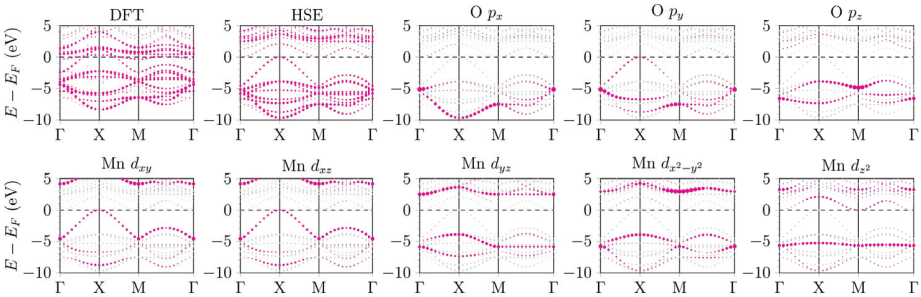

(k) ***h*-Sc_2O_3**

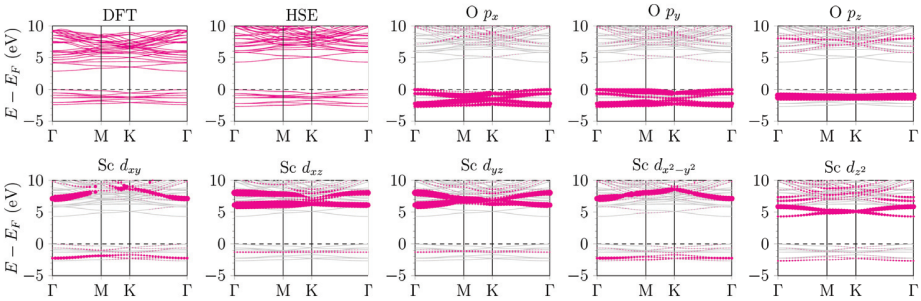

(l) ***h*-Ti_2O_3**

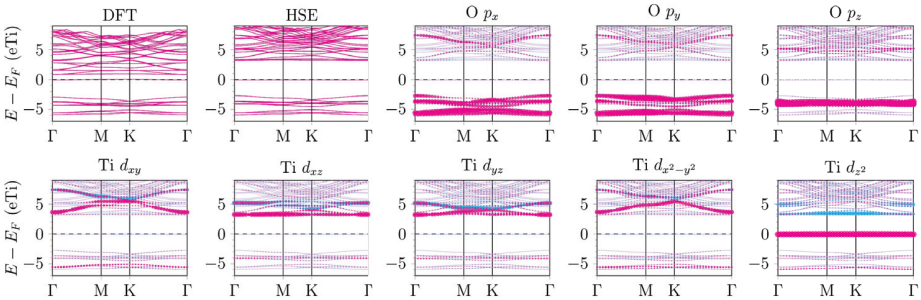

(m) ***h*-V_2O_3**

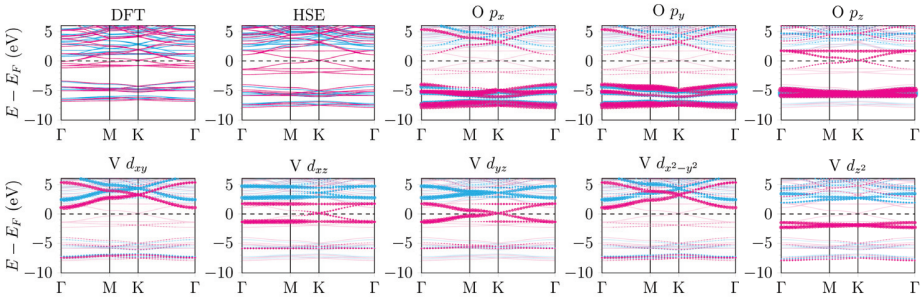

(n) ***h*-Cr_2O_3**

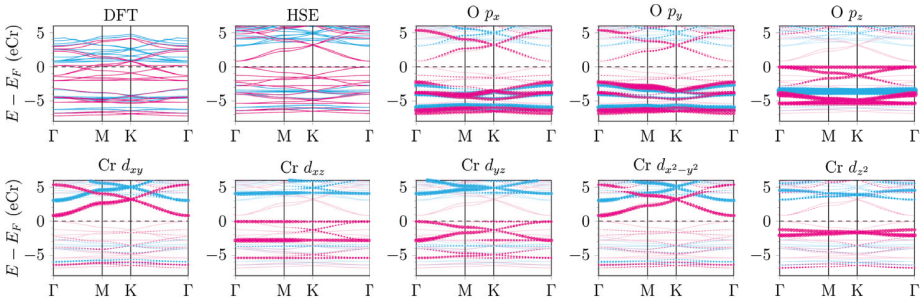

(o) ***h*-Mn_2O_3**

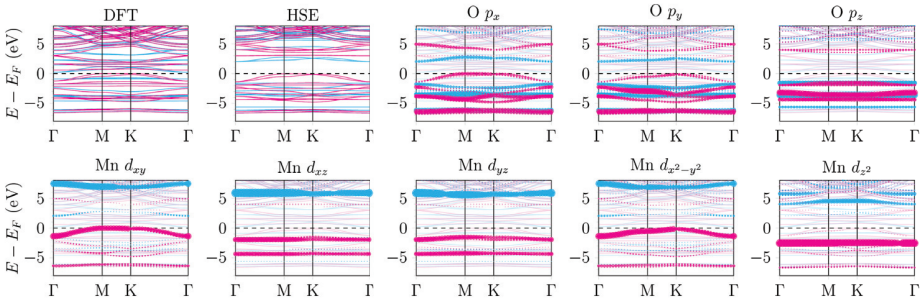

(p) ***c*-ScO$_2$**

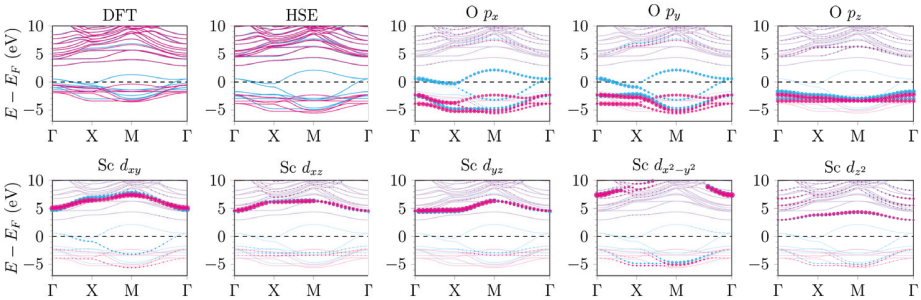

(q) ***c*-TiO$_2$**

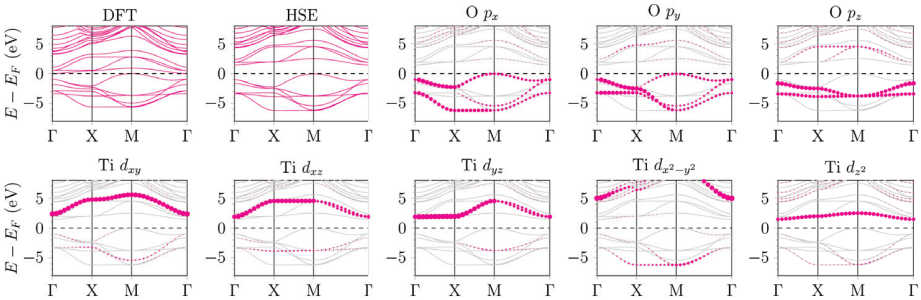

(r) ***c*-VO$_2$**

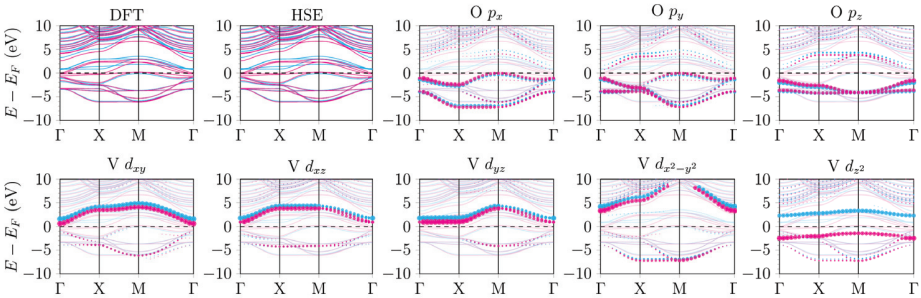

(s) ***c*-CrO$_2$**

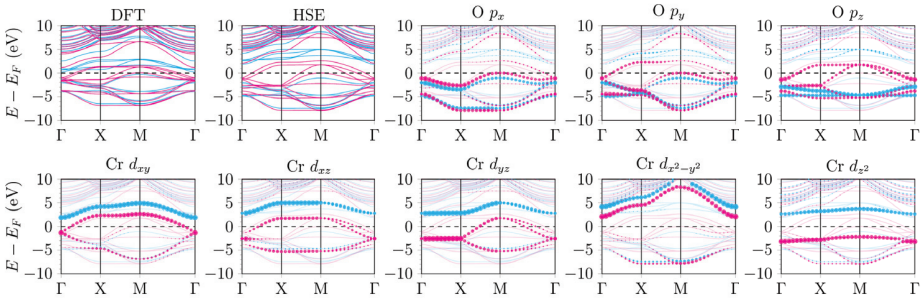

(t) ***c*-MnO$_2$**

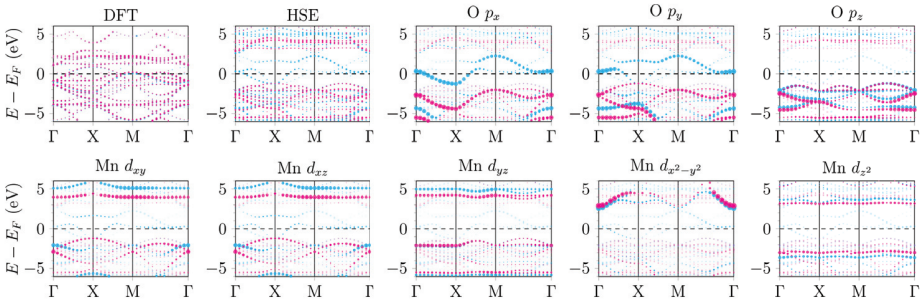

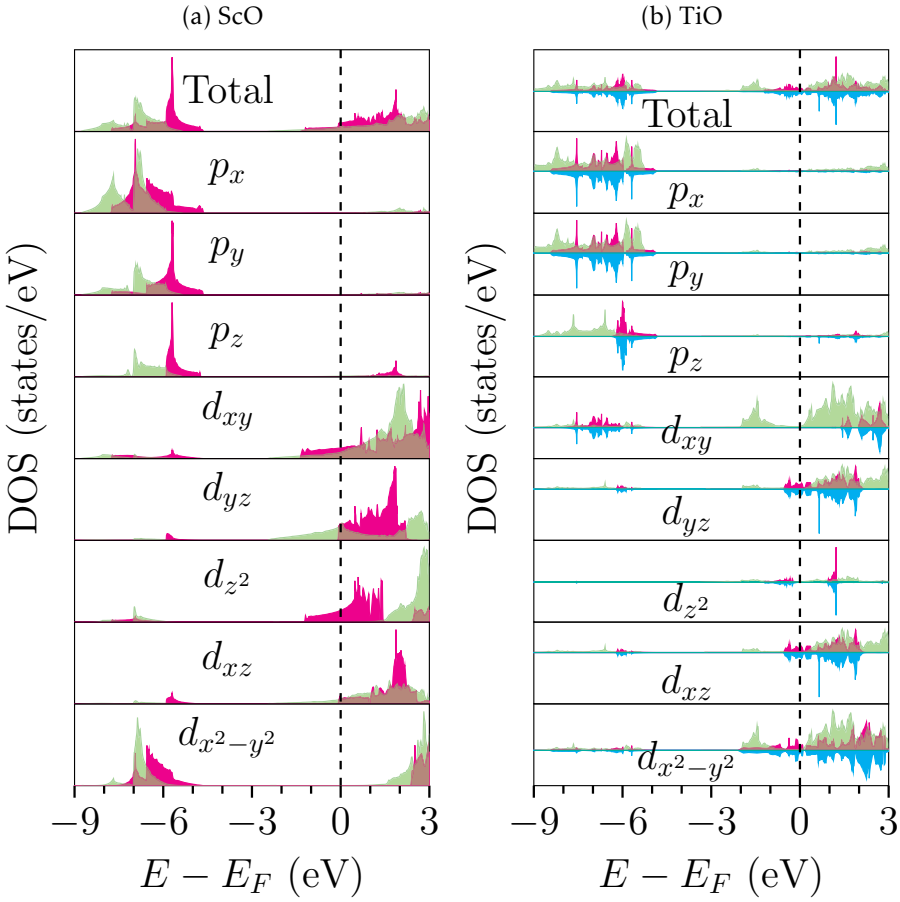

Figure C.2: GGA-PBE DOS plots of both 2D (magenta: GGA-PBE, spin-up; cyan: GGA-PBE spin-down) and the corresponding bulk (green: spin-up; orange:spin down) *rs*-TMOs. All the DOS plots are per forming unit. Fermi level is subtracted to be the zero point of energy.

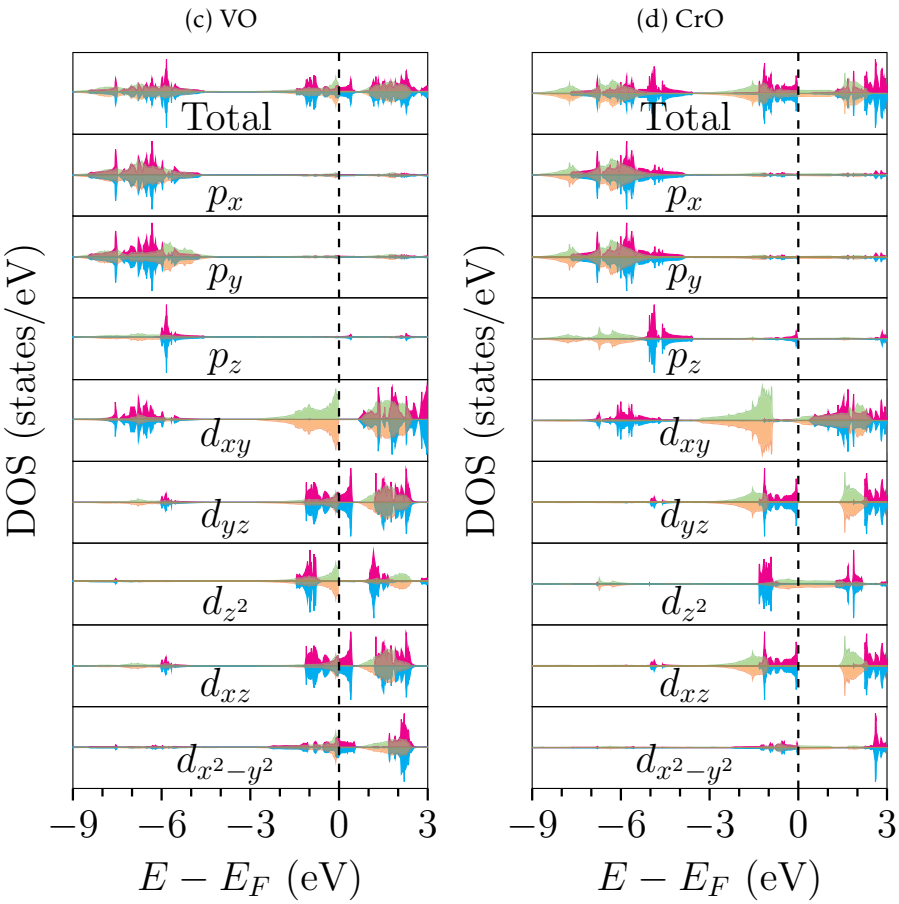
(c) VO
(d) CrO
Total
p_x
p_y
p_z
d_{xy}
d_{yz}
d_{z^2}
d_{xz}
$d_{x^2-y^2}$
DOS (states/eV)
−9
−6
−3
0
3
$E - E_F$ (eV)

(e) MnO

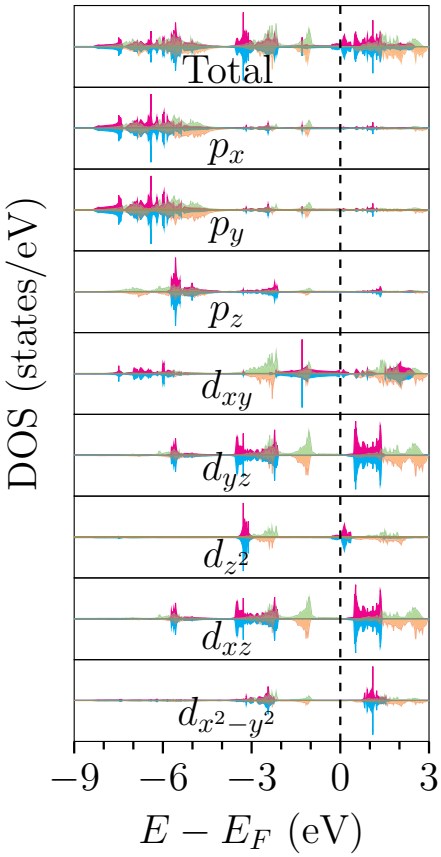

References

1. Momma, K. & Izum, F. VESTA3 for three-dimensional visualization of crystal, volumetric and morphology data. *J. Appl. Cryst.* **44,** 1272 (2011).
2. Kittel, C. *Introduction to Solid State Physics, 8th Edition* (John Wiley Sons, Inc., 2005).
3. Cai, W. & Nix, W. D. *Imperfections in Crystalline Solids* (Cambridge University Press, University Printing House, Cambridge CB2 8BS, United Kingdom, 2016).
4. De Walle, C. G. V. & Janotti, A. Advances in electronic structure methods for defects and impurities in solids. *Phys. Status Solidi B* **248,** 19 (2011).
5. Groeneveld, E., Witteman, L., Lefferts, M., Ke, X., Bals, S., Van Tendeloo, G. & de Mello Donega, C. Tailoring ZnSe–CdSe Colloidal Quantum Dots via Cation Exchange: From Core/Shell to Alloy Nanocrystals. *ACS Nano* **7,** 7913 (2013).
6. Queisser, H. J. & Haller, E. E. Defects in Semiconductors: Some Fatal, Some Vital. *Science* **281,** 945 (1998).
7. Yalcin, A. O., Fan, Z., Goris, B., Li, W.-F., Koster, R. S., Fang, C.-M., van Blaaderen, A., Casavola, M., Tichelaar, F. D., Bals, S., Tendeloo, G. V., Vlugt, T. J. H., Vanmaekelbergh, D., Zandbergen, H. W. & van Huis, M. A. Atomic resolution monitoring of cation Exchange in CdSe-PbSe heteronanocrystals during epitaxial solid-solid-vapor growth. *Nano Lett.* **14,** 3661 (2014).
8. Fan, Z., Lin, L.-C., Buijs, W., Vlugt, T. J. H. & van Huis, M. A. Atomistic Understanding of Cation Exchange in PbS Nanocrystals Using Simulations with Pseudoligands. *Nature Communications* **7,** 11503 (2016).
9. Hong, J., Hu, Z., Probert, M., Li, K., Lv, D., Yang, X., Gu, L., Mao, N., Feng, Q., Xie, L., Zhang, J., Wu, D., Zhang, Z., Jin, C., Ji, W., Zhang, X., Yuan, J. & Zhang, Z. Exploring atomic defects in molybdenum disulphide monolayers. *Nat. Commun.* **6,** 6293 (2015).

10. Li, W.-F., Fang, C.-M. & van Huis, M. A. Strong spin-orbit splitting and magnetism of point defect states in monolayer WS_2. *Phys. Rev. B* **94,** 195425 (2016).

11. Seebauer, E. G. & Noh, K. W. Trends in semiconductor defect engineering at the nanoscale. *Mater. Sci. Eng. R* **70,** 151 (2010).

12. Lin, Z., Carvalho, B. R., Kahn, E., Lv, R., Rao, R., Terrones, H., Pimenta, M. A. & Terrones, M. Trends in semiconductor defect engineering at the nanoscale. *2D Mater.* **3,** 022002 (2016).

13. Kelly, A. & Knowles, K. M. *Crystallography and Crystal Defects, 2nd Edition* (John Wiley Sons, Ltd., The Atrium, Southern Gate, Chichester, West Sussex, PO19 8SQ, United Kingdom, 2012).

14. Freysoldt, C., Grabowski, B., Hickel, T. & Neugebauer, J. First-principles calculations for point defects in solids. *Rev. Mod. Phys.* **86,** 253 (2014).

15. Evarestov, R. A. *Quantum Chemistry of Solids - The LCAO First Principles Treatment of Crystals* (Springer, 2008).

16. *Advanced Calculations for Defects in Materials* (eds Alkauskas, A., Deák, P., Neugebauer, J., Pasquarello, A. & de Walle, C. G. V.) (Wiley-VCH Verlag GmbH Co. KGaA, Boschstr 12, 69469 Weinheim, Germany, 2011).

17. Castleton, C. W. M., Höglund, A. & Mirbt, S. Advances in electronic structure methods for defects and impurities in solids. *Modelling Simul. Mater. Sci. Eng.* **17,** 084003 (2009).

18. Lee, H., Leventis, H. C., Moon, S.-J., Chen, P., Ito, S., Haque, S. A., Torres, T., Nuesch, F., Geiger, T., Zakeeruddin, S. M., Gratzel, M. & Nazeeruddin, M. K. PbS and CdS Quantum Dot-Sensitized Solid-State Solar cells: "Old Concepts, New Results". *Adv. Funct. Mater.* **19,** 2735 (2009).

19. Casavola, M., van Huis, M. A., Bals, S., Lambert, K., Hens, Z. & Vanmaekelbergh, D. Anisotropic Cation Exchange in PbSe/CdSe Core/Shell Nanocrystals of Different Geometry. *Chem. Mater.* **24,** 294–302 (2012).

20. Groiss, H., Kaufmann, E., Springholz, G., Schwarzl, T., Hesser, G., Schäffler, F., Heiss, W., Koike, K., Itakura, T., Yano, M. & Wojtowicz, T. Size control and midinfrared emission of epitaxial PbTe/CdTe quantum dot precipitates grown by molecular beam epitaxy. *Appl. Phys. Lett.* **91,** 222106 (2007).

21. Son, D. H., Hughes, S. M., Yin, Y. & Alivisatos, A. P. Cation Exchange Reactions in Ionic Nanocrystals. *Science* **306,** 1009 (2004).

22. Jain, P. K., Amirav, L., Aloni, S. & Alivisatos, A. P. Nanoheterostructure Cation Exchange: Anionic Framework Conservation. *J. Am. Chem. Soc.* **132,** 9997 (2010).

23. Li, H., Zanella, M., Genovese, A., Povia, M., Falqui, A., Giannini, C. & Manna, L. Sequential Cation Exchange in Nanocrystals: Preservation of Crystal Phase and Formation of Metastable Phases. *Nano Lett.* **11,** 4964 (2011).

24. Miszta, K., Dorfs, D., Genovese, A., Kim, M. R. & Manna, L. Cation exchange reactions in colloidal branched nanocrystals. *ACS NANO* **5,** 7176 (2011).

25. Bals, S., Casavola, M., van Huis, M. A., Aert, S. V., Batenburg, K. J., Tendeloo, G. V. & Vanmaekelbergh, D. Three-Dimensional Atomic Imaging of Colloidal CoreÀShell Nanocrystals. *Nano Lett.* **11,** 3420 (2011).

26. Sheng, Y., Wei, J., Liu, B. & Peng, L. A facile route to synthesize CdZnSe core–shell-like alloyed quantum dots via cation exchange reaction in aqueous system. *Mater. Rea. Bull.* **57,** 67 (2014).

27. Ataca, C., Şahin, H. & Ciraci, S. Stable, Single-Layer MX 2 Transition-Metal Oxides and Dichalcogenides in a Honeycomb-Like Structure. *J. Phys. Chem. C* **116,** 8983 (2012).

28. Mak, K. F., Lee, C., Hone, J., Shan, J. & Heinz, T. F. Atomically Thin MoS_2: A New Direct-Gap Semiconductor. *Phys. Rev. Lett.* **105,** 136805 (2010).

29. Kuc, A., Zibouche, N. & Heine, T. Influence of quantum confinement on the elctronic structure of the transition metal sulfide TS_2. *Phys. Rev. B* **83,** 245213 (2011).

30. Wang, Q. H., Kalantar-Zadeh, K., Kis, A., Coleman, J. N. & Strano, M. S. Electronics and optoelectronics of two-dimensional transition metal dichalcogenides. *Nat. Nanotechnol.* **7,** 699 (2012).

31. Roldan, R., Silva-Guillén, J. A., López-Sancho, P., Guinea, F., Cappelluti, E. & Ordejón, P. Electronic properties of single-layer and multilayer transition metal dichalcogenides MX_2 (M = Mo, W and X = S, Se). *Ann. Phys. (Berlin)* **526,** 347 (2014).

32. Heine, T. Transition Metal Chalcogenides: Ultrathin Inorganic Materials with Tunable Electronic Properties. *Acc. Chem. Res.* **48,** 65 (2015).

33. Ganatra, R. & Zhang, Q. Few-layer MoS_2: A Promising Layered Semiconductor. *ACS NANO* **8,** 4074 (2014).

34. Bahlawane, N. & Lenoble, D. Vanadium Oxide Compounds: Structure, Properties, and Growth from the Gas Phase. *Chem. Vap. Deposition* **20,** 299 (2014).

35. Schwingenschlögl, U. & Eyert, V. The Vanadium Magneéli phases V_nO_2n-1. *Ann. Phys. (Leipzig)* **13,** 475 (2004).

36. Kitchaev, D. A., Peng, H., Liu, Y., Sun, J., Perdew, J. P. & Ceder, G. Energetics of MnO_2 polymorphs in density functional theory. *Phys. Rev. B* **93,** 045132 (2016).

37. Komsa, H.-P., Kotakoski, J., Kurasch, S., Lehtinen, O., Kaiser, U. & Krasheninnikov, A. V. Two-Dimensional Transition Metal Dichalcogenides under Electron Irradiation: Defect Production and Doping. *Phys. Rev. Lett.* **109,** 035503 (2012).

38. Qiu, H., Xu, T., Wang, Z., Ren, W., Nan, H., Ni, Z., Chen, Q., Yuan, S., Miao, F., Song, F., Long, G., Shi, Y., Sun, L., Wang, J. & Wang, X. Hopping transport through defect-induced localized states in molybdenum disulphide. *Nat. Commun.* **4,** 2642 (2013).

39. Ataca, C. & Ciraci, S. Functionalization of Single-Layer MoS_2 Honeycomb Structure. *J. Phys. Chem. C* **115,** 13303 (2011).

40. Thomas, L. H. The calculation of atomic fields. *Proc. Cambridge Philos. Soc* **23,** 542 (1927).

41. Fermi, E. Un Metodo Statistico per la Determinazione di alcune Prioprietá dell'Atomo. *Rend. Accad. Nat. Lincei* **6,** 602 (1927).

42. Hohenburg, P. & Kohn, W. Inhomogeneous electron gas. *Phys. Rev.* **136,** B864 (1964).

43. Kohn, W. & Sham, L. J. Self-Consistent Equations Including Exchange and Correlation Effects. *Phys. Rev.* **140,** A1133 (1965).

44. Kohn, W. Nobel Lecture: Electronic structure of matter—wave functions and density functionals. *Rev. Mod. Phys.* **71,** 1253 (1999).

45. Capelle, K. *A Bird's-Eye View of Density-Functional Theory* <https://arxiv.org/pdf/cond-mat/0211443.pdf> (2002).

46. Lejaeghere, K., Bihlmayer, G., Björkman, T., Blaha, P., Blügel, S., Blum, V., Caliste, D., Castelli, I. E., Clark, S. J., Dal Corso, A., de Gironcoli, S., Deutsch, T., Dewhurst, J. K., Di Marco, I., Draxl, C., Dułak, M., Eriksson, O., Flores-Livas, J. A., Garrity, K. F., Genovese, L., Giannozzi, P., Giantomassi, M., Goedecker, S., Gonze, X., Grånäs, O., Gross, E. K. U., Gulans, A., Gygi, F., Hamann, D. R., Hasnip, P. J., Holzwarth, N. A. W., Iuşan, D., Jochym, D. B., Jollet, F., Jones, D., Kresse, G., Koepernik, K., Küçükbenli, E., Kvashnin, Y. O., Locht, I. L. M., Lubeck, S., Marsman, M., Marzari, N., Nitzsche, U.,

Nordström, L., Ozaki, T., Paulatto, L., Pickard, C. J., Poelmans, W., Probert, M. I. J., Refson, K., Richter, M., Rignanese, G.-M., Saha, S., Scheffler, M., Schlipf, M., Schwarz, K., Sharma, S., Tavazza, F., Thunström, P., Tkatchenko, A., Torrent, M., Vanderbilt, D., van Setten, M. J., Van Speybroeck, V., Wills, J. M., Yates, J. R., Zhang, G.-X. & Cottenier, S. Reproducibility in density functional theory calculations of solids. *Science* **351** (2016).

47. *Electronic structure: basic theory and practical methods* (ed Martin, R. M.) (Cambridge University Press, University Printing House, Cambridge CB2 8BS, United Kingdom, 2004).
48. Fuchs, M. *Comparison of exchange-correlation functionals: from LDA to GGA and beyond* A hands-On computer course. 2005.
49. Perdew, J., Burke, K. & Ernzerhof, M. Generalized gradient approximation made simple. *Phys. Rev. Lett.* **77,** 3865 (1996).
50. Perdew, J., Burke, K. & Ernzerhof, M. Generalized gradient approximation made simple. *Phys. Rev. Lett.* **78,** 1396 (1997).
51. Imada, M., Fujimori, A. & Tokura, Y. Metal-insulator transitions. *Rev. Mod. Phys.* **70,** 1039 (1998).
52. Heyd, J., Scuseria, G. E. & Ernzerhof, M. Hybrid functionals based on a screened Coulomb potential. *J. Chem. Phys* **118,** 8207 (2003).
53. Krukau, A. V., Vydrov, O. A., Izmaylov, A. F. & Scuseria, G. E. Influence of the exchange screening parameter on the performance of screened hybrid functionals. *J. Chem. Phys.* **125,** 224106 (2006).
54. Hakala, M. *Atomicand electronic transport on surfaces and interfaces* PhD thesis (Aalto University, Helsinki, 2013).
55. Bloch, F. Über die Quantenmechanik der Elektronen in Kristallgittern. *Z. Physik* **52,** 555 (1929).
56. Blöchl, P. Projector augmented-wave method. *Phys. Rev. B* **50,** 17953 (1994).
57. Kresse, G. & Joubert, D. From ultrasoft pseudopotentials to the projector augmented-wave method. *Phys. Rev. B* **59,** 1758 (1999).
58. Payne, M., Teter, M. P., Allan, D. C., Arias, T. A. & Joannopoulos, J. D. Iterative minimization techniques for *ab initio* total-energy calculations: molecular dynamics and conjugate gradient. *Rev. Mod. Phys.* **64,** 1045 (1992).
59. Kresse, G. & Hafner, J. *Ab initio* molecular-dynamics simulation of the liquid-metal–amorphous-semiconductor transition in germanium. *Phys. Rev. B* **49,** 14251 (1994).

60. Kresse, G. & Furthmüller, J. Efficiency of ab-initio total energy calculations for metals and semiconductors using a plane-wave basis set. *Comput. Mat. Sci.* **6,** 15 (1996).

61. Kresse, G. & Furthmüller, J. Efficient iterative schemes for *ab initio* total-energy calculations using a plane-wave basis set. *Phys. Rev. B* **54,** 11169 (1996).

62. De Walle, C. G. V. & Neugebauer, J. First-principles calculations for defects and impurities: Applications to III-nitrides. *J. Appl. Phys.* **95,** 3581 (2004).

63. Christoph Freysoldt, J. N. & de Walle, C. G. V. Fully ab initio finite-size corrections for charged-defect supercell calculations. *Phys. Rev. Lett.* **102,** 016402 (2009).

64. Komsa, H.-P. & Pasquarello, A. Finite-size supercell correction for charged defects at surfaces and interfaces. *Phys. Rev. Lett.* **110,** 095505 (2013).

65. Komsa, H.-P., Berseneva, N., Krasheninnikov, A. V. & Nieminen, R. M. Charged point defects in the flatland: accurate formation energy calculations in two-dimensional materials. *Phys. Rev. X* **4,** 031044 (2014).

66. Oba, F., Choi, M., Togo, A. & Tanaka, I. Point defects in ZnO: an approach from first principles. *Sci. Technol. Adv. Mater.* **12,** 034302 (2011).

67. Dalven, R. *Solid State Physics* (Academic, New York, 1973).

68. Dughaish, Z. Lead telluride as a thermoelectric material for thermoelectric power generation. *Physica B* **322,** 205 (2002).

69. Chaudhuri, T. K. A solar thermophotovoltaic converter using Pbs photovoltaic cells. *Int. J. Eng. Res.* **16,** 481 (1992).

70. Preier, H. Recent Advances in Lead-Chalcogenide Diode Lasers. *Appl. Phys.* **20,** 189 (1979).

71. Chatterjee, S. & Pal, U. Low-cost solar selective absorbers from Indian galena. *Opt. Eng. (Bellingham)* **32,** 2923 (1993).

72. Gfroerer, T. H. *Photoluminescence in Analysis of Surfaces and Interfaces. In Encyclopedia of Analytical Chemistry* (John Wiley & Sons Ltd., Chichester, 2000).

73. De Mello Donegá, C. Synthesis and properties of colloidal heteronanocrystals. *Chem. Soc. Rev.* **40,** 1512 (2011).

74. Moreels, I., Lambert, K., Muynck, D. D., Vanhaecke, F., Poelman, D., Martins, J. C., Allan, G. & Hens, Z. Composition and Size-Dependent Extinction Coefficient of Colloidal PbSe Quantum Dots. *Chem. Mater.* **19,** 6101 (2007).

75. Moreels, I., Martins, B. F. J. C. & Hens, Z. Surface Chemistry of Colloidal PbSe Nanocrystals. *J. Am. Chem. Soc.* **130,** 15081 (2008).

76. Ott, F. D., Spiegel, L. L., Norris, D. J. & Erwin, S. C. Microscopic Theory of Cation Exchange in CdSe Nanocrystals. *Phys. Rev. Lett.* **113,** 156803 (2014).

77. Miller, E., Komarek, K. & Cadoff, I. Interrelation of Electronic Properties and Defect Equilibria in PbTe. *J. Appl. Phys.* **32,** 2457 (1961).

78. Polity, A., Krause-Rehberg, R., Zlomanov, V., Stanov, V. & Chatchaturov, A. Study of vacancy defects in PbSe and $Pb_{1-x}Sn_xSe$ by positron annihilation. *J. Cryst. Growth* **131,** 271 (1993).

79. Khokhlov, D. *Lead Chalcogenides: Physics and Applications* (CRC Press, Washington, 2002).

80. Yoneda, S., Kato, M. & Ohsugi, I. J. Anomaly in the specific heat of lead tellurides. *J. Theo. Appl. Phys.* **7,** 11 (2013).

81. Zhang, B., Cai, C., Jin, S., Ye, Z., Wu, H. & Qi, Z. Resonant nature of intrinsic defect energy levels in PbTe revealed by infrared photoreflectance spectroscopy. *Appl. Phys. Lett.* **105,** 022109 (2014).

82. Koumoulis, D., Taylor, R. E., D. King, J. & Bouchard, L.-S. NMR study of native defects in PbSe. *Phys. Rev. B* **90,** 125201 (2014).

83. Parada, N. J. & George W. Pratt, J. New model for vacancy states in PbTe. *Phys. Rev. Lett.* **22,** 180 (1969).

84. Parada, N. J. Localized defects in PbTe. *Phys. Rev. B* **3,** 2042 (1971).

85. Lent, C. S., Bowen, M. A., Allgaier, R. S., Dow, J. D., Sankey, O. F. & Ho, E. S. Impurity levels in PbTe and $Pb_{1-x}Sn_xTe$. *Solid State Commun.* **61,** 83 (1987).

86. Ahmad, S., Mahanti, S., Hoang, K. & Kanatzidis, M. Ab initio studies of the electronic structure of defects in PbTe. *Phys. Rev. B* **74,** 155205 (2006).

87. Ding, Y., Wang, Y., Ni, J., Shi, L., Shi, S. & Tang, W. First principles study of structural, vibrational and electronic properties of graphene-like MX_2 (M=Mo, Nb, W, Ta; X=S, Se, Te) monolayers. *Physica B* **406,** 2254 (2011).

88. Hoang, K., Mahanti, S. & Jena, P. Theoretical study of deep-defect states in bulk PbTe and in thin films. *Phys. Rev. B* **76,** 115432 (2007).

89. Walsh, A. Defect Processes in a PbS Metal Organic Framework: A Quantum-Confined Hybrid Semiconductor. *J. Phys. Chem. Lett.* **1,** 1284 (2010).

90. Peng, H., Li, J., Li, S.-S. & Xia, J.-B. Possible origin of ferromagnetism in undoped anatase TiO_2. *Phys. Rev. B* **79,** 092411 (2009).

91. Berashevich, J., Semeniuk, O., Rubel, O., Rowlands, J. A. & Reznik, A. Lead monoxide α-PbO: electronic properties and point defect formation. *J. Phys.: Condens. Matter* **25,** 075803 (2013).

92. Wrasse, E. O., Bairerle, R. J., Fazzio, A. & Schmidt, T. M. First-principles study of group III impurity doped PbSe: Bulk and nanowire. *Phys. Rev. B* **87,** 085428 (2013).

93. Kim, D., Kim, D.-H., Lee, J.-H. & Grossman, J. C. Impact of Stoichiometry on the Electronic Structure of PbS Quantum Dots. *Phys. Rev. Lett.* **110,** 196802 (2013).

94. Wei, J.-W., Ma, Z.-W., Zeng, H., Wang, Z.-Y., Wei, Q. & Peng, P. Electronic and optical properties of vacancy-doped WS_2 monolayers. *AIP Advances* **2,** 042141 (2012).

95. Albanesi, E. A., Okoye, C. M. I., Rodriguez, C. O. & y Blanca, E. L. P. Electronic structure, structural properties, and dielectric functions of IV-VI semiconductors: PbSe and PbTe. *Phys. Rev. B* **61,** 16589 (2000).

96. Lach-hab, M., Papaconstantopoulos, D. A. & Mehl, M. J. Electronic structure calculations of lead chalcogenides PbS, PbSe, PbTe. *J. Phys. Chem. Solids* **63,** 833 (2002).

97. Kresse, G., Surnev, S., Ramsey, M. & Netzer, F. First-principles calculations for V_xV_y grown on Pd(1 1 1). *Surf. Sci.* **492,** 329 (2001).

98. Zhang, Y., Ke, X., Chen, C. & J. Yang, P. R. C. K. Thermodynamic properties of PbTe, PbSe, and PbS: First-principles study. *Phys. Rev. B* **80,** 024304 (2009).

99. He, J., Zhao, L.-D., Zheng, J.-C., Doak, J. W., Wu, H., Wang, H.-Q., Lee, Y., Wolverton, C., Kanatzidis, M. G. & Dravid, V. P. Role of Sodium Doping in Lead Chalcogenide Thermoelectrics. *J. Am. Chem. Soc.* **135,** 4624 (2013).

100. Skelton, J. M., Parker, S. C., Togo, A., Tanaka, I. & Walsh, A. Thermal physics of the lead chalcogenides PbS, PbSe, and PbTe from first principles. *Phys. Rev. B* **89,** 205203 (2014).

101. Walsh, A. & Watson, G. W. Preparation of PbS-type PbO nanocrystals in a room-temperature ionic liquid. *J. Solid State Chem.* **178,** 1422 (2005).

102. Madelung, O., Rössler, U. & Schulz, M. *Semiconductors: Group IV Elements, IV-IV and III-IV Compounds, Landolt-Börnstein, New Series, Group III, Vol. 41, Pt. A* (Springer-Verlag, Berlin, 2005).

103. Perdew, J. P. & Zunger, A. Self-interaction correction to density-functional approximations for many-electron systems. *Phys. Rev. B* **23,** 5048 (1981).

104. Skelton, J. M., Parker, S. C., Togo, A., Tanaka, I. & Walsh, A. Thermal physics of the lead chalcogenides PbS, PbSe, and PbTe from first principles. *Phys. Rev. B* **89,** 205203 (2014).

105. Constantin, L. A., Pitarke, J. M., Dobson, J. F., Garcia-Lekue, A. & Perdew, J. P. High-Level Correlated Approach to the Jellium Surface Energy, without Uniform-Gas Input. *Phys. Rev. Lett.* **100,** 036401 (2008).

106. Svane, A., Christensen, N. E., Cardona, M., Chantis, A. N., van Schilfgaarde, M. & Kotani, T. Quasiparticle self-consistent GW calculations for PbS, PbSe, and PbTe: Band structure and pressure coefficients. *Phys. Rev. B* **81,** 245120 (2010).

107. Strehlow, W. H. & Cook, E. L. Compilation of energy band gaps in elemental and binary compound semiconductors and insulators. *J. Phys. Chem. Ref. Data* **2,** 163 (1973).

108. Kullerrud, G. The lead-sulfur system. *Am. J. Sci., Schairer Vol.* **267-A,** 233 (1969).

109. Lin, J.-C., Sharma, R. & Chang, Y. The PbS (Lead-Sulfur) system. *Bull. Alloy Phase Diagrams* **7,** 374 (1986).

110. Lin, J.-C., Sharma, R. & Chang, Y. The Pb-Se (lead-selenium) system. *J. Phase Equilib.* **17,** 253 (1996).

111. Lin, J.-C., Hsieh, K.-C., Sharma, R. & Chang, Y. The Pb-Te (lead-tellurium) system. *Bull. Alloy Phase Diagrams* **10,** 340 (1989).

112. Fang, C.-M., van Huis, M. A., Jansen, J. & H. W. Z, b. Role of carbon and nitrogen in Fe_2C and Fe_2N from first-principles calculations. *Phys. Rev. B* **84,** 094102 (2011).

113. Fan, Z., Yalcin, A. O., Tichelaar, F. D., Zandbergen, H. W., Talgorn, E., Houtepen, A. J., Vlugt, T. J. H. & van Huis, M. A. From Sphere to Multipod: Thermally Induced Transitions of CdSe Nanocrystals Studied by Molecular Dynamics Simulations. *J. Am. Chem. Soc.* **135,** 5869 (2013).

114. Chai, L., Al-Sawai, W., Gao, Y., Houtepen, A. J., Mijnarends, P. E., Barbiellini, B., Schut, H., van Schaarenburg, L. C., van Huis, M. A., Ravelli, L., Egger, W., Kaprzyk, S., Bansil, A. & Eijt, S. W. H. Surfaces of colloidal PbSe nanocrystals probed by thin-film positron annihilation spectroscopy. *APL Materials* **11,** 02211 (2013).

115. Kutana, A. & Erwin, S. C. PbSe nanocrystals remain intrinsic after surface adsorption of hydrazine. *Phys. Rev. B* **83,** 235419 (2011).

116. Naeemullah, Murtaza, G., Khenata, R., Hassan, N., Naeem, S., Khalid, M. & Omran, S. B. Structural and optoelectronic properties of PbS_xSe_{1-x}, PbS_xTe_{1-x} and $PbSe_xTe_{1-x}$ via first-principles calculations. *Comp. Mater. Sci.* **83,** 496 (2014).

117. Shannon, R. Revised effective ionic radii and systematic studies of interatomic distances in halides and chalcogenides. *Acta Cryst.* **A32,** 751 (1976).

118. Li, Z., Yang, J., Hou, J. G. & Zhu, Q. Inorganic Electride: Theoretical Study on Structural and Electronic Properties. *J. Am. Chem. Soc.* **125,** 6050 (2003).

119. Furness, J. W., Verbeke, J., Tellgren, E. I., Stopkowicz, S., Ekström, U., Helgaker, T. & Teale, A. M. Current Density Functional Theory Using Meta-Generalized Gradient Exchange-Correlation Functionals. *J. Chem. Theory Comput.* **11,** 4169 (2015).

120. Kimoon. Dicalcium nitride as a two-dimensional electride with an anionic electron layer. *Nature* **494,** 336 (2013).

121. Dale, S. G., Otero-de-la-Roza, A. & Johnson, E. R. Density-functional description of electrides. *Phys. Chem. Chem. Phys.* **16,** 14584 (2014).

122. Smallenburg, F., Filion, L., Marechal, M. & Dijkstra, M. Vacancy-stabilized crystalline order in hard cubes. *P. Natl. Acad. Sci. USA* **109,** 17886 (2012).

123. Reshchikov, M. A. & Morkoç, H. Luminescence properties of defects in GaN. *J. Appl. Phys.* **97,** 061301 (2005).

124. Krause, M. M., Mooney, J. & Kambhampati, P. Chemical and Thermodynamic Control of the Surface of Semiconductor Nanocrystals for Designer White Light Emitters. *ACS Nano* **7,** 5922 (2013).

125. Voznyy, O., Thon, S. M., Ip, A. H. & Sargent, E. H. Dynamic Trap Formation and Elimination in Colloidal Quantum Dots. *J. Phys. Chem. Lett.* **4,** 987 (2013).

126. Chhowalla, M., Shin, H. S., Eda, G., Li, L.-J., Loh, K. P. & Zhang, H. The chemistry of two-dimensional layered transition metal dichalcogenide nanosheets. *Nat. Chem.* **5,** 263 (2013).

127. Schmidt, H., Giustiniano, F. & Eda, G. Electronic transport properties of transition metal dichalcogenide field-effect devices: surface and interface effect. *Chem. Soc. Rev.* **44,** 7715 (2015).

128. *Electrons and Phonons in Layered Crystal Structures* (eds Wieting, T. J. & Schlüter, M.) (Springer, Netherlands, 1979).

129. Coehoorn, R., Haas, C. & de Groot, R. A. Electronic structure of $MoSe_2$, MoS_2, and WSe_2. II. The nature of the optical band gaps. *Phys. Rev. B* **35,** 6203 (1987).

130. Zhu, L., Zhou, J., Guo, Z. & Sun, Z. MetalMetal Bonding Stabilized Ground State Structure of Early Transition Metal Monoxide TMMO (TM = Ti, Hf, V, Ta). *J. Phys. Chem. C* **120,** 10009 (2016).

131. Xiao, X., Song, H., Lin, S., Zhou, Y., Zhan, X., Hu, Z., Zhang, Q., Sun, J., Yang, B., Li, T., Jiao, L., Zhou, J., Tang, J. & Gogotsi, Y. Scalable salt-templated synthesis of two-dimensional transition metal oxides. *Nature Commun.* **7,** 11296 (2015).

132. Feng, W., Yao, Y., Zhu, W., Zhou, J., Yao, W. & Xiao, D. Intrinsic spin Hall effect in monolayers of group-VI dichalcogenides: A first-principles study. *Phys. Rev. B* **86,** 165108 (2012).

133. Kośmider, K., González, J. W. & Fernández-Rossier, J. Large spin splitting in the conduction band of transition metal dichalcogenide monolayers. *Phys. Rev. B* **88,** 245436 (2013).

134. Ataca, C., Şahin, H., Aktürk, E. & Ciraci, S. Mechanical and Electronic Properties of MoS_2 Nanoribbons and Their Defects. *J. Phys. Chem. C* **115,** 3934 (2011).

135. Ma, Y., Dai, Y., Guo, M., Niu, C., Lu, J. & Huang, B. Electronic and magnetic properties of perfect, vacancy-doped, and nonmetal adsorbed $MoSe_2$, $MoTe_2$ and WS_2 monolayers. *Phys. Chem. Chem. Phys.* **13,** 15546 (2011).

136. Koh, E. W. K., Chiu, C. H., Lim, Y. K., Zhang, Y.-W. & Pan, H. Hydrogen adsorption on and diffusion through MoS_2 monolayer: First-principles study. *Int. J. Hydrogen Energy* **37,** 14323 (2012).

137. Liu, D., Guo, Y., Fang, L. & Robertson, J. Sulfur vacancies in monolayer MoS 2 and its electrical contacts. *Appl. Phys. Lett.* **103,** 183113 (2013).

138. Carvalho, A. & Neto, A. H. C. Donor and acceptor levels in semiconducting transition-metal dichalcogenides. *Phys. Rev. B* **89,** 081406(R) (2014).

139. Chang, J., Larentis, S., Emanuel Tutuc, L. F. R. & Banerjee, S. K. Atomistic simulation of the electronic states of adatoms in monolayer MoS_2. *Appl. Phys. Lett.* **104,** 141603 (2014).

140. Yuan, S., Roldán, R., Katsnelson, M. I. & Guinea, F. Effect of point defects on the optical and transport properties of MoS2$and WS_2$. *Phys. Rev. B* **90,** 041402(R) (2014).

141. Rastogi, P., Kuma, S., Bhowmick, S., Agarwal, A. & Chauhan, Y. S. Doping Strategies for Monolayer MoS 2 via Surface Adsorption: A Systematic Study. *J. Phys. Chem. C* **118,** 30309 (2014).

142. Lu, S.-C. & Leburton, J.-P. Electronic structures of defects and magnetic impurities in MoS_2 monolayers. *Nanoscale Res. Lett.* **9,** 676 (2014).

143. Chow, P. K., Jacobs-Gedrim, R. B., Gao, J., Lu, T.-M., Yu, B., Terrones, H. & Koratkar, N. Defect-Induced Photoluminescence in Monolayer Semiconducting Transition Metal Dichalcogenides. *ACS Nano* **9,** 1520 (2015).

144. Liu, H., Han, N. & Zhao, J. Atomistic insight into the oxidation of monolayer transition metal dichalcogenides: from structures to electronic properties. *RSC Adv.* **5,** 17572 (2015).

145. Hu, Z. & Metiu, H. Choice of U for DFT+U Calculations for Titanium Oxides. *J. Phys. Chem. C* **115,** 5841 (2011).

146. Zhao, W., Ghorannevis, Z., Chu, L., Toh, M., Kloc, C., Tan, P.-H. & Eda, G. Evolution of Electronic Structure in Atomically Thin Sheets of WS_2 and WSe_2. *ACS NANO* **7,** 791 (2012).

147. Li, H., Liu, S., Huang, S., Yin, D., Li, C. & Wang, Z. Impurity-induced ferromagnetism and metallicity of WS_2 monolayer. *Ceram. Int.* **42,** 2364 (2015).

148. Liu, Z., Suenaga, K., Wang, Z., Shi, Z., Okunishi, E. & Iijima, S. Identification of active atomic defects in a monolayered tungsten disulphide nanoribbon. *Nat. Commun.* **2,** 213 (2011).

149. Komsa, H.-P., Kurasch, S., Kaiser, O. L. U. & Krasheninnikov, A. V. From point to extended defects in two-dimensional MoS_2 : Evolution of atomic structure under electron irradiation. *Phys. Rev. B* **88,** 035301 (2013).

150. Zhou, W., Zou, X., Najmaei, S., Liu, Z., Shi, Y., Kong, J., Lou, J., Ajayan, P. M., Yakobson, B. I. & Idrobo, J.-C. Intrinsic Structural Defects in Monolayer Molybdenum Disulfide. *Nano Lett.* **13,** 2615 (2013).

151. Noh, J.-Y., Kim, H. & Kim, Y.-S. Stability and electronic structures of native defects in single-layer MoS_2. *Phys. Rev. B* **89,** 205417 (2014).

152. Komsa, H.-P. & Krasheninnikov, A. V. Native defects in bulk and monolayer MoS_2 from first principles. *Phys. Rev. B* **91,** 125304 (2015).

153. Haldar, S., Vovusha, H., Yadav, M. K., Eriksson, O. & Sanyal, B. Systematic study of structural, electronic, and optical properties of atomic-scale defects in the two-dimensional transition metal dichalcogenides MX_2 (M = Mo, W; X = S, Se, Te). *Phys. Rev. B* **92,** 235408 (2015).

154. Nair, R., Tsai, I.-L., Sepioni, M., Lehtinen, O., Keinonen, J., Krasheninnikov, A., Neto, A. C., Katsnelson, M., Geim, A. & Grigorieva, I. Dual origin of defect magnetism in graphene and its reversible switching by molecular doping. *Nature Commun* **4,** 2010 (2013).

155. Han, W., Kawakami, R. K., Gmitra, M. & Fabian, J. Graphene spintronics. *Nature Nanotechnology* **9,** 794 (2014).

156. Hashmi, A. & Hong, J. Transition Metal Doped Phosphorene: First-Principles Study. *J. Phys. Chem. C* **119,** 9198 (2015).

157. Sun, M., Ren, Q., Zhao, Y., Wang, S., Yu, J. & Tang, W. Magnetism in transition metal-substituted germanane: A search for room temperature spintronic devices. *J. Appl. Phys.* **119,** 143904 (2016).

158. Vignale, G. & Rasolt, M. Density-Functional Theory in Strong Magnetic Fields. *Phys. Rev. Lett.* **59,** 2360 (1987).

159. Vignale, G. & Rasolt, M. Current- and spin-density-functional theory for inhomogeneous electronic systems in strong magnetic fields. *Phys. Rev. B* **37,** 10685 (1988).

160. Pohra, S. & Görling, A. Exact-Exchange Spin-Current Density-Functional Theory. *Phys. Rev. Lett.* **97,** 013005 (2006).

161. Hobbs, D., Kresse, G. & Hafner, J. Fully unconstrained noncollinear magnetism within the projector augmented-wave method. *Phys. Rev. B* **62,** 11556 (2010).

162. Steiner, S., Khmelevskyi, S., Marsmann, M. & Kresse, G. Transition Metal Doped Phosphorene: First-Principles Study. *Phys. Rev. B* **93,** 224425 (2016).

163. Latzke, D. W., Zhang, W., Suslu, A., Chang, T.-R., Lin, H., Jeng, H.-T., Tongay, S., Wu, J., Bansil, A. & Lanzara, A. Electronic structure, spin-orbit coupling, and interlayer interaction in bulk MoS_2 and WS_2. *Phys. Rev. B* **91,** 235202 (2015).

164. Klimeš, J., Bowler, D. R. & Michaelides, A. Chemical accuracy for the van der Waals density functional. *J. Phys.: Condens. Matter* **22,** 022201 (2010).

165. Frey, G. L., Tenne, R., Matthews, M. J., Dresselhaus, M. S. & Dresselhaus, G. Optical properties of MS_2 (M = Mo, W) inorganic fullerene-like and nanotube material optical absorption and resonance Raman measurements. *J. Mater. Res.* **13,** 2412 (1998).

166. De Walle, C. G. V. & Neugebauer, J. First-principles calculations for defects and impurities: Applications to III-nitrides. *J. Appl. Phys.* **95,** 3851 (2004).

167. Padilha, J. E., Peelaers, H., Janotti, A. & de Walle, C. G. V. Nature and evolution of the band-edge states in MoS_2 : From monolayer to bulk. *Phys. Rev. B* **90,** 205420 (2014).

168. Novoselov, S., K., Geim, A. K., Morozov, S. V., Jiang, D., Zhang, Y., Dubonos, S. V., Grigorieva, I. V. & Firsov, A. A. Electric Field Effect in Atomically Thin Carbon Films. *Science*, 666 (2004).

169. Butler, S. Z., Hollen, S. M., Cao, L., Cui, Y., Gupta, J. A., Gutierrez, H. R., Tony F. Heinz, S. S. H., Huang, J., Ismach, A. F., Johnston-Halperin, E., Kuno, M., Plashnitsa, V. V., Robinson, R. D., Ruoff, R. S., Salahuddin, S., Shan, J., Shi, L., Spencer, O. M. G., Terrones, M., Windl, W. & Goldberger, J. E. Progress, Challenges, and Opportunities in Two-Dimensional Materials Beyond Graphene. *ACS NANO* **7,** 2898 (2013).

170. Bhimanapati, G. R., Lin, Z., Meunier, V., Jung, Y., Cha, J., Das, S., Xiao, D., Son, Y., Strano, M. S., Cooper, V. R., Liang, L., Louie, S. G., Ringe, E., Zhou, W., Kim, S. S., Naik, R. R., Sumpter, B. G., Terrones, H., Xia, F., Wang, Y., Zhu, J., Akinwande, D., Alem, N., Schuller, J. A., Schaak, R. E., Terrones, M. & Robinson, J. A. Recent Advances in Two-Dimensional Materials beyond Graphene. *ACS NANO* **9,** 11509 (2015).

171. Mott, N. F. Metal-Insulator Transition. *Rev. Mod. Phys.* **40,** 677 (1968).

172. Xu, S., Shen, X., Hallman, K. A., F, R. & Haglund, J. Unified Band Theoretic Description of Electronic and Magnetic Properties of Vanadium Dioxide Phases. *arXiv* **1606,** 03162 (2016).

173. Park, J. H., Coy, J. M., Kasirga, T. S., Huang, C., Fei, Z., Hunter, S. & Cobden, D. H. Measurement of a solid-state triple point at the metal–insulator transition in VO_2. *Nature* **500,** 431 (2013).

174. Wegkamp, D., Herzog, M., Xian, L., Gatti, M., Cudazzo, P., McGahan, C. L., Marvel, R. E., Richard F. Haglund, J., Rubio, A., Wolf, M. & Stähler, J. Instantaneous Band Gap Collapse in Photoexcited Monoclinic VO_2 due to Photocarrier Doping. *Phys. Rev. Lett.* **113,** 216401 (2014).

175. Li, Y.-F., Zhu, S.-C. & Liu, Z.-P. Reaction Network of Layer-to-Tunnel Transition of MnO_2. *J. Am. Chem. Soc.* **138,** 5371 (2016).

176. Angelis, F. D., Valentin, C. D., Fantacci, S., Vittadini, A. & Selloni, A. Theoretical Studies on Anatase and Less Common TiO_2 Phases: Bulk, Surfaces, and Nanomaterials. *Chem. Rev.* **114,** 9708 (2014).

177. Makarevich, A. M., Sadykov, I. I., Sharovarov, D. I., Amelichev, V. A., Adamenkov, A. A., Tsymbarenko, D. M., Plokhih, A. V., Esaulkov, M. N., Solyankin, P. M. & Kau, A. R. Chemical synthesis of high quality epitaxial vanadium dioxide films with sharp electrical and optical switch properties. *J. Mater. Chem. C* **3,** 9097 (2015).

178. Surnev, S., Vitali, L., Ramsey, M. G., Netzer, F. P., Kresse, G. & Hafner, J. Growth and structure of ultrathin vanadium oxide layers on Pd(111). *Phys. Rev. B* **61,** 13945 (2000).

179. Surnev, S., Kresse, G., Ramsey, M. G. & Netzer, F. P. Novel Interface-Mediated Metastable Oxide Phases: Vanadium Oxides on Pd(111). *Phys. Rev. Lett.* **87,** 086102 (2001).

180. Ataca, C., Şahin, H. & Ciraci, S. Stable, Single-Layer MX_2 Transition-Metal Oxides and Dichalcogenides in a Honeycomb-Like Structure. *J. Phys. Chem. C* **116,** 8983 (2012).

181. Rasmussen, F. A. & Thygesen, K. S. Computational 2D Materials Database: Electronic Structure of Transition-Metal Dichalcogenides and Oxides. *J. Phys. Chem. C* **119,** 13169 (2015).

182. Omomo, Y., Sasaki, T., Wang, L. & Watanabe, M. Redoxable Nanosheet Crystallites of MnO_2 Derived via Delamination of a Layered Manganese Oxide. *J. Am. Chem. Soc.* **125,** 3568 (2003).

183. Kan, M., Zhou, J., qnd Y. Kawazoe, Q. S. & Jena, P. The Intrinsic Ferromagnetism in a MnO_2 Monolayer. *J. Phys. Chem. Lett.* **4,** 3382 (2013).

184. Nam, K. M., Kim, Y.-I., Jo, Y., Lee, S. M., Kim, B. G., Choi, R., Choi, S.-I., Song, H. & Park, J. T. New Crystal Structure: Synthesis and Characterization of Hexagonal Wurtzite MnO. *J. Am. Chem. Soc.* **134,** 8392 (2012).

185. Kan, E., Li, M., Hu, S., Xiao, C., Xiang, H. & Deng, K. Two-Dimensional Hexagonal Transition-Metal Oxide for Spintronics. *J. Phys. Chem. Lett.* **4,** 1120 (2013).

186. Wang, J. & Zhang, Y. Topologic connection between 2-D layered structures and 3-D diamond structures for conventional semiconductors. *Sci. Rep.* **6,** 24660 (2016).

187. Mackrodt, W. C., Middlemiss, D. S. & Owens, T. G. Hybrid density functional theory study of vanadium monoxide. *Phys. Rev. B* **69,** 115119 (2004).

188. Franchini, C., Podloucky, R., Paier, J., Marsman, M. & Kresse, G. Ground-state properties of multivalent manganese oxides: Density functional and hybrid density functional calculations. *Phys. Rev. B* **75,** 195128 (2007).

189. Schrön, A., Rödl, C. & Bechstedt, F. Energetic stability and magnetic properties of MnO in the rocksalt, wurtzite, and zinc-blende structures: Influence of exchange and correlation. *Phys. Rev. B* **82,** 165109 (2010).

190. Guo, Y., Clark, S. J. & Robertson, J. Electronic and magnetic properties of Ti_2O_3, Cr_2O_3, and Fe_2O_3 calculated by the screened exchange hybrid density functional. *J. Phys.: Condens. Matter* **24,** 325504 (2012).

191. Karlický, F., Zbořil, R. & Otyepka, M. Band gaps and structural properties of graphene halides and their derivates: A hybrid functional study with localized orbital basis sets. *J. Chem. Phys.* **137,** 034709 (2012).

192. Komsa, H.-P. & Krasheninnikov, A. V. Native defects in bulk and monolayer MoS_2 from first principles. *Phys. Rev. B* **91,** 125304 (2015).

193. Fang, C.-M., van Huis, M., Sluiter, M. & Zandbergen, H. Stability, structure and electronic properties of γ-$Fe_{23}C_6$ from first-principles theory. *Acta Materialia* **58,** 2968 (2010).

194. Boukhvalov, D. Stable antiferromagnetic graphone. *Physica E* **43,** 199 (2010).

195. Lany, S. Semiconductor thermochemistry in density functional calculations. *Phys. Rev. B* **78,** 245207 (2008).

196. Wang, J., Meng, J., Li, Q. & Yang, J. Single-layer cadmium chalcogenides: promising visible-light driven photocatalysts for water splitting. *Phys. Chem. Chem. Phys.* **18,** 17029 (2016).

197. Shang, S.-L., Lindwall, G., Wang, Y., Redwing, J. M., Anderson, T. & Liu, Z.-K. Lateral Versus Vertical Growth of Two-Dimensional Layered Transition-Metal Dichalcogenides: Thermodynamic Insight into MoS_2. *Nano Lett.* **16,** 5742 (2016).

198. Fu, B., Ge, Y., Su, W., Guo, W. & Liu, C.-C. A new kind of 2D topological insulators BiCN with a giant gap and its substrate effects. *Sci. Rep.* **6,** 30003 (2016).

199. Surnev, S., Kresse, G., Ramsey, M. G. & Netzer, F. P. Novel Interface-Mediated Metastable Oxide Phases: Vanadium Oxides on Pd(111). *Phys. Rev. Lett.* **87,** 086102 (2001).

200. Surnev, S., Vitali, L., Ramsey, M. G., Netzer, F. P., Kresse, G. & Hafner, J. Growth and structure of ultrathin vanadium oxide layers on Pd(111). *Phys. Rev. B* **61,** 13945 (2000).

201. Bersuker, I. B. Pseudo-Jahn-Teller Effect — A Two-State Paradigm in Formation, Deformation, and Transformation of Molecular Systems and Solids. *Chem. Rev.* **113,** 1351 (2013).

202. Jose, D. & Datta, A. Understanding of the Buckling Distortions in Silicene. *J. Phys. Chem. C* **116,** 24639 (2012).

203. Nijamudheen, A., Bhattacharjee, R., Choudhury, S. & Datta, A. Electronic and Chemical Properties of Germanene: The Crucial Role of Buckling. *J. Phys. Chem. C* **119,** 3802 (2015).

204. Wang, Y. & Ding, Y. Unexpected buckled structures and tunable electronic properties in arsenic nanosheets: insights from first-principles calculations. *J. Phys.: Condens. Matter* **27,** 225304 (2015).

205. Amano, S., Bogdanovski, D., Yamane, H., Terauchi, M. & Dronskowski, R. ϵ-TiO, a Novel Stable Polymorph of Titanium Monoxide. *Angew. Chem. Int. Ed.* **55,** 1652 (2016).

206. Rivadulla, F., Fernández-Rossier, J., García-Hernández, M., López-Quintela, M. A., Rivas, J. & 5, J. B. G. VO: A strongly correlated metal close to a Mott-Hubbard transition. *Phys. Rev. B* **76,** 205110 (2007).

207. Lim, J. S., Saldana-Greco, D. & Rappe, A. M. Improved pseudopotential transferability for magnetic and electronic properties of binary manganese oxides from DFT+U+J calculations. *Phys. Rev. B* **94,** 165151 (2016).

208. Gopal, P., Spaldin, N. A. & Waghmare, U. V. First-principles study of wurtzite-structure MnO. *Phys. Rev. B* **70,** 205104 (2004).

209. Jacobs, R. M., Booske, J. H. & Morgan, D. Intrinsic defects and conduction characteristics of Sc_2O_3 in thermionic cathode systems. *Phys. Rev. B* **86,** 054106 (2012).

210. Guo, Y., Clark, S. J. & Robertson, J. Calculation of metallic and insulating phases of V_2O_3 by hybrid density functionals. *J. Chem. Phys.* **140,** 054702 (2014).

211. Gerosa, M., Bottani, C. E., Caramella, L., Onida, G., Valentin, C. D. & Pacchioni, G. Electronic structure and phase stability of oxide semiconductors: Performance of dielectric-dependent hybrid functional DFT, benchmarked against GW band structure calculations and experiments. *Phys. Rev. B* **91,** 155201 (2015).

212. Singh, V. & Pulikkotil, J. Electronic phase transition and transport properties of Ti_2O_3. *J. Alloys Compd.* **658,** 430 (2016).

213. Grieger, D. & Fabrizio, M. Low-temperature magnetic ordering and structural distortions in vanadium sesquioxide V_2O_3. *Phys. Rev. B* **92,** 075121 (2015).

214. Leonov, I., Anisimov, V. I. & Vollhardt, D. Metal-insulator transition and lattice instability of paramagnetic V_2O_3. *Phys. Rev. B* **91,** 195115 (2015).

215. Shi, S., Wysocki, A. L. & Belashchenko, K. D. Magnetism of chromia from first-principles calculations. *Phys. Rev. B* **79,** 104404 (2009).

216. Stashans, A. & Jácome, S. Local structure, magnetic and electronic properties of N-doped α-Cr_2O_3 from the first-principles. *Comput. Mater. Sci.* **81,** 353 (2014).

217. Cockayne, E., Levin, I., Wu, H. & Llobet, A. Magnetic structure of bixbyite α-Mn_2O_3: A combined DFT+U and neutron diffraction study. *Phys. Rev. B* **87,** 184413 (2013).

218. Luo, Y., Benali, A., Shulenburger, L., Krogel, J. T. & Kent, O. H. P. R. C. Phase Stability of TiO_2 Polymorphs from Diffusion Quantum Monte Carlo. *arXiv* **1607,** 07361v2 (2016).

219. Schwarz, K. CrO_2 predicted as a half-metallic ferromagnet. *J. Phys. F: Met. Phys.* **16,** L211 (1986).

220. Solovyev, I. V., Kashin, I. V. & Mazurenko, V. V. Mechanisms and origins of half-metallic ferromagnetism in CrO_2. *Phys. Rev. B* **92,** 144407 (2015).

221. Shaked, H., J. Faber, J. & Hitterman, R. L. Low-temperature magnetic structure of Mno: A high-resolution neutron-diffraction study. *Phys. Rev. B* **38,** 11901 (1988).

222. Goodwin, A. L., Tucker, M. G., Dove, M. T. & Keen, D. A. Magnetic Structure of MnO at 10 K from Total Neutron Scattering Data. *Phys. Rev. Lett.* **96,** 047209 (2006).

223. Zheng, H. & Wagner, L. K. Computation of the Correlated Metal-Insulator Transition in Vanadium Dioxide from First Principles. *Phys. Rev. Lett.* **114,** 176401 (2015).

224. Eyert, V. VO_2: A Novel View from Band Theory. *Phys. Rev. B* **107,** 016401 (2011).

225. Revard, B. C., Tipton, W. W., Yesypenko, A. & Hennig, R. G. Grand-canonical evolutionary algorithm for the prediction of two-dimensional materials. *Phys. Rev. B* **93,** 054117 (2016).

226. De Groot, R. A., Mueller, F. M., van Engen, P. G. & Buschow, K. H. J. New Class of Materials: Half-Metallic Ferromagnets. *Phys. Rev. Lett.* **50,** 2024 (1983).

227. Fang, C. M., de Wijs, G. A. & de Groot, R. A. Spin-polarization in half-metals. *J. Appl. Phys.* **91,** 8340 (2002).

228. Katsnelson, M. I., Irkhin, V. Y., Chioncel, L. & de Groot, R. A. Half-metallic ferromagnets: From band structure to many-body effects. *Rev. Mod. Phys.* **80,** 315 (2008).

229. Slater, J. C. & Shockley, W. Optical Absorption by the Alkali Halides. *Phys. Rev.* **50,** 705 (1936).

230. De Boer, P. K. & de Groot, R. A. The origin of the conduction band in table salt. *Am. J. Phys.* **67,** 443 (1999).

231. Dion, M., Rydberg, H., Schröder, E., Langreth, D. C. & Lundqvist, B. I. Van der Waals Density Functional for General Geometries. *Phys. Rev. Lett.* **92,** 246401 (2004).

Acknowledgements

I am happy that this thesis can be consummated with my acknowledgements. I am also happy that I could still have some time, after an intense period of writing this thesis, sitting before my laptop and lingering on how much I have been helped by so many people in the last four years. The more I look back, the more I realize that my PhD study is not only an exploration of 2D and 3D nanomaterials using DFT, but even more it is a unforgettable life journey on which I am not alone.

First of all, thank you very much, Marijn! Thank you for bringing me to the group four years ago and your support all the way till now. On research, I appreciate that you have deep knowledge as well as rich experience on both the experimental and the theoretical aspects of nanomaterials science. Therefore you can always give me valuable insights of my simulation results from an experimental perspective, thereby helping me to obtain a whole scenario of my research. I also appreciate that you gave me much freedom for my research, such that I can happily spend my time exploring interesting topics and try to carry them out independently. Meanwhile, you are always willing to discuss with me and guide my direction with timely suggestions. Furthermore, I am grateful that you are willing to spend much time on reviewing and correcting my manuscripts. In particular, thank you very much for helping me translate my Summary into Dutch! You are always gentle in your supervision, and do not begrudge to give applause when you feel to. From this I am very much encouraged.

I would also like to thank my promotors: Marjolein and Alfons. Thank you for your valuable remarks given during the group work discussions, and also reviewing my manuscripts and this thesis.

Thank you Changming. I have been greatly benefited not only by your profound knowledge of DFT and materials science, but also by your encouragements and help beyond science. Thank you for being always open and willing to discuss with me, no matter my question is related to practical computational settings, or to detailed analysis of materials properties. Also, thank you for being candid in correcting my ideas and pointing out the insufficiencies of my manuscripts. From you I learned the preciousness of being truthful to people and to research.

My thanks go to other SCM staff members: Arnout, Renë, Laura, Patrick and Krassimir. Thank you for giving me your precious comments and suggestions during the work discussions. I am honored to work in such a group with an excellent academic performance.

Of course, thank you, all the other SCM members! Although seemingly my DFT study does not overlap very well with all the topics that you are doing, I truly enjoyed the time I had with all of you during the Debye spring schools and the DO! Days, work discussions, wonderful lab outings, and all the daily short conversations. I enjoyed working in this stimulating and pleasant environment. Thank you, Simone (Dussi), Ajoy, Ravi Wiebke, Carmine, Guido, Frankje, Xiaodan, Massimiliano, Tonnishtha, Robin (van Damme), Giulia, Dnyaneshwar, Robin (Geitenbeek), Fabian, Douglas, Stijn, Jessi, Naveed, Chris, Rama, Da, Berend, Pepijn, Henriëtte, Vats, Federico, Anna, Siddharth, Harini, Vassilis, Sina, Nick, Thomas, Wessel, Ernest, Tom, Peter, Michiel, Relinde, Chris, and Judith. Also, I would like to thank the former SCM members who I met in the past: Teun, Bo, Bart, Marlous, Jissy, Joost, Anjan, Nina, Simone (Belli), Thijs, John, Tian-Song, Bas, Marjolein (van der Linden), Rao, Weikai, and Bing.

Special thanks go to my fellow DFT peers and office mates. Dank je wel, Rik! Het was heel leuk om je als mijn collega te hebben tijdens deze vier jaar. Ik waardeer dat je verwlkomt al mijn problemen aangaande mijn berekeningen, en je bent altijd gewillig om deze allerlei soorten problemen op te losen. Ik heb ook zo veel genoten van onze 'Nederlands-tutoring pauzes'. Ik kan zeggen dat mijn Nederlands is daardoor echt verbeterd worden. Thank you Somil! You always bring joy to the office and make everybody happy. Also thank you for the many inspiring discussions we had on both the computational setups and on our research projects. Together with Rik, our trip to San-Sebastian for the Psi-K conference was really enjoyable. Thank you Yang, I enjoyed very much sitting next to you as you are always pleasant and willing to give me useful advices on different things. I also enjoyed the French sweets you brought many times from France. Thank you Xiaobin, for your poem on Bryan's card and your water boiler. The three of you have made OL173 a very joyful and lively place for work, even for writing my thesis!

劉洋，曉濱，呈輝，子俊，禹廷，薇薇和文津，謝謝你們和我一起度過許多個輕鬆愉快的午餐時光(雖然我後來就沒有辦法和你們一起吃了)。

至品，謝謝你總是很樂意又不厭其煩地和我討論關於我對VASP的設定或是背後物理原理的疑惑。這對我的研究有極大的幫助。

廖老師，MY Liao，謝謝你！謝謝你在我們大學時充滿熱情地和我們相處，不只教化學，更是教對人生的態度。從你身上我看到對追求科學的熱情；你鼓勵我們出國，也是我人生的一大啓蒙。

Thank you Henryk. Your indescribably in-depth knowledge of quantum chemistry as well as other subjects in physics laid a good founda-

tion for me to continue my research here in the Netherlands in solid-state physics. I always remember you said that all the seemingly unrelated fields in natural science will eventually merge together if we continue to learn more in each field; just like a group of expanding circles will eventually be merged together and become one large circle. This has become my attitude of learning new things and become a great help in my PhD study.

Dank jullie wel, onze aardige buren op de straat, voor zo'n aangename en vriendelijke omgeving waarin wij kunnen leven.

I am so thankful that I am surrounded by you – dear brothers and sisters in the Lord in the Netherlands. I can testify from my heart that because of you, my life in the Netherlands has become so meaningful and far more profound than it would have been if I did not meet you. I am sorry that I could not mention all the precious experiences we have had in such a short paragraph. But I appreciate that we really take care of one another in the love and the life of the Lord. I could not have made it this far without you. Especially, I would like to thank all the saints who are now meeting, or used to meet, in Utrecht. Thank you for the intimate fellowship we have had in the past years and all your support and prayer for me and for my family. So, thank you very much, Ray and Leone, Bert and Margreet, Paul and Haimy, Evert and Yvonne, Stefan and Fengju, David and Prisca, Pieter and Lisanne, Johan and Christina, Weiyu, Keen, Lai, Andi, Patrick and Yahui, Tessa, Christina (Gu), Paul (Ding), JJ, Jia Xin, Jane, Han, Yuan, William, Rujung, Amy and Roy, and Matthew (although we haven't met each other in person, I enjoyed having morning revival with you via WhatsApp!). In het bijzonder, dank jullie wel, broeders in Utrecht! Ik ben echt bemoedigd om samen met jullie de Heer te genieten en Hem te kunnen dienen.

Bovedien, van harte bedankt, dierbare heiligen in Spakenburg, voor jullie zoete voorziening in het Lichaam door deze jaren heen.

I also would like to say thank you to the dear brothers and sisters I met during the student meeting on Thursdays in Utrecht: Thijs, Anne-Marijn, Wouter, Harriët, Bridget, Qingkang, JJ, Paul, Christina Gu, Jane, and Betzy. Every time after I met with you I was refreshed. It was so enjoyable to sing, to pray-read, and to share our enjoyments with one another.

Dank jullie wel, Bert, Margreet, Layla, Fay, en Anne-lynn. Voor Tina en ik, onze leven in Nederland was vier jaar geleden begonnen met jullie warme gastvrijheid in Lunetten. (Sorry hoor, ik had zo veel broden gegeten! :P) Wij hebben zo veel zoete samenkomsten gehad bij jullie thuis. Deze ervaring is gewoon onvergetelijk. Mag de Heer jullie blijven zegenen!

I would like to also to thank the saints back in Taiwan. James and Beryl, thank you very much for your fellowship, suggestions, prayers, and practical supports during my applications for a PhD vacancy in the Netherlands. Furthermore, thank you for introducing us into the church life here in the

Netherlands. Your appreciation and loving care for all the saints are a good pattern to me.

親愛的林仲石弟兄和美雀姊，謝謝你們早從我還在訓練時就開始服事我和鈺婷，又使我們能認識那時正在荷蘭的鄭世進弟兄夫婦，開啓我們來歐洲的交通。謝謝你們！

親愛的在桃園，新竹，和埔里的弟兄姊妹，謝謝你們在我成長各個階段的服事和成全，使我今天即便在荷蘭，也能夠過召會生活。你們在主裡的擺上是我最好的榜樣。

謝謝在歐洲各地的同伴，雖然交通的機會有限，但是仍然很得你們的加強和激勵。願我們靠著恩典在歐洲一直與主一同行動。

親愛的岳父岳母, 我實在非常謝謝你們的照顧！常常海運台灣的食材或是日用品給我們，給我們最周全的補給。尤其是兩次孩子的出生，都勞煩媽媽放下店裡繁忙的事務，來這裡幫鈺婷坐月子及照顧寶寶，分擔家務，讓我們吃到好吃營養的食物，也讓我能把心力放在研究上，謝謝你們的幫忙！願神祝福你們！也謝謝鈺圃，大姊和大姊夫。每次回台灣看到你們都覺得好親切。

親愛的姊姊、姊夫、心純和心樂！謝謝你們常常去看望爸爸媽媽，甚至是婆婆。每次回台灣，也謝謝你們來找我們。和你們相處在一起，眞的很有泡溫泉的效果–溫暖；身心完全放鬆，備感顧惜。願主祝福你們這一家！親愛的爸爸媽媽，雖然你們遠在台灣，但你們的禱告扶持實在是我最大的力量。不只是讓我有動力完成研究，更使我被保守在主的行動中。親愛的婆婆，謝謝妳一路將我帶大。我不會忘記妳每次見到朋友就自豪地說：我這個孫子出生第八天就到妳家了。謝謝妳提早退休來照顧我。現在我也很高興可以把我的論文當作禮物送給妳。願主祝福您！

謝謝我在台灣的其他家人，謝謝你們的禱告和各種方式的支持！

親愛的曉恩，感謝主將妳帶給我們。不知道我用中文寫對妳的感謝和珍賞，會不會激發妳學中文的動力？感謝主，眞是藉由妳使我們曉得神的恩典。我絕對不會忘記妳禱告說要我晚上出門要小心，不要遇到壞人、熊、或是野狼；也禱告願主耶穌祝福我論文早點寫完，早點睡覺，就不用當貓頭鷹了。妳也常常關心我身上的小傷口，或是如果我感冒了，也會祝我快點好起來。謝謝妳的貼心。每次跟妳一起玩，也都讓我覺得很療癒。我把論文封面的底色用成淡粉紅色的，想說妳會很喜歡，果不其然！所以我很高興可以把我的論文當成是一本送給妳的書；這讓我覺得寫論文有了更多意義。

親愛的倍恩，謝謝主耶穌在最好的時間點把你帶給我們。你是神賜給我們加倍的恩典，提醒我無論在什麼環境，都要加倍享受神的恩典。願主祝福你和姊姊，在恩典中長大，成爲主合用的器皿。

親愛的鈺婷，對妳的感激實在是難以描述。感謝主將妳擺在我身邊。謝謝妳對小孩還有這個家全心全意，無怨無悔的付出，是讓我最穩定和安心的後盾。有時候就算我們在生活的逆境中，也從來不曾聽妳埋怨過要回台灣。謝謝妳一路的扶持和陪伴。願我們一直作最親密的活力伴。

Murphy (文凡), April 2017 in Utrecht

List of Publications

This thesis is based on the following publications:

1. Yalcin, A. O., Fan, Z., Goris, B., **Li, W.-F.**, Koster, R. S., Fang, C.-M., van Blaaderen, A., Casavola, M., Tichelaar, F. D., Bals, S., Tendeloo, G. V., Vlugt, T. J. H., Vanmaekelbergh, D., Zandbergen, H. W. & van Huis, M. A. Atomic resolution monitoring of cation exchange in CdSe-PbSe heteronanocrystals during epitaxial solid-solid-vapor growth. *Nano Lett.* **14,** 3661 (2014).
2. **Li, W.-F.**, Fang, C.-M., Dijkstra, M. & van Huis, M. A. The role of point defects in PbS, PbSe and PbTe: a *first principles* study. *J. Phys.: Condens. Matter* **27,** 355801 (2015).
3. **Li, W.-F.**, Fang, C.-M. & van Huis, M. A. Strong spin-orbit splitting and magnetism of point defect states in monolayer WS_2. *Phys. Rev. B* **94,** 195425 (2016).
4. **Li, W.-F.**, Fang, C.-M., Koster, R. S., Dijkstra, M. & van Huis, M. A. An *ab-initio* prediction of novel transition metal oxide monolayers. *In preparation* (2017).

Other publications to which the author contributed:

1. Fang, C.-M., **Li, W.-F.**, Koster, R. S., Klimeš, J., van Blaaderen, A. & van Huis, M. A. The accurate calculation of the band gap of liquid water by means of *GW* corrections applied to plane-wave density functional theory molecular dynamics simulations. *Phys. Chem. Chem. Phys.* **17,** 365 (2015).
2. Fang, C.-M., Koster, R. S., **Li, W.-F.** & van Huis, M. A. Predicted stability, structures, and magnetism of 3d transition metal nitrides: the M_4N phases. *RSC Adv.* **4,** 7885 (2014).

3. **Li, W.-F.**, Andrzejak, M. & Witek, H. A. Evolution of physical properties of conjugated system. *Phys. Status Solidi B* **249,** 306 (2012).
4. Chou, C.-P., **Li, W.-F.**, Andrzejak, M. & Witek, H. A. in *Spectroscopy, Dynamics And Molecular Theory Of Carbon Plasmas And Vapors* (ed Irle, S.) 375–415 (World Scientific Press, Singapore, 2011).
5. **Li, W.-F.**, Irle, S. & Witek, H. A. Convergence in the evolution of nanodiamond raman spectra with particle size: A theoretical investigation. *ACS NANO* **4,** 4475 (2010).
6. Chang, B.-C., **Lee, W.-F.**, Li, F.-Y. & Liao, M.-Y. The development and application of nuclear quadrupole resonance: Chemical analysis of targeted drugs. *Chemistry (The Chinese Chem. Soc., Taipei)* **63,** 177 (2005).

About the author

Wun-Fan Li was born on January 11th, 1985 in Taoyuan City, Taiwan. After graduating from National Taoyuan Senior High School in 2003, he started his bachelor in the Department of Applied Chemistry at National Chi Nan University in Nantou County, Taiwan. His bachelor research project was on the theoretical calculations of nuclear magnetic resonance (NMR) signals for drug detection under the supervision of Prof. Ming-Yuan Liao. In 2007, he graduated *cum laude* and began his master study at National Chiao Tung University in Hsin-Chu City, Taiwan under the supervision of Prof. Henryk Witek. During his master study, he also visited the Quantum Chemistry group of Prof. Stephan Irle in Nagoya University, Japan for two months, focusing on the simulation of vibrational spectra of carbon nanostructures. His master thesis was entitled "Geometric, Electronic, and Vibrational Properties of Conductive Polymers and Carbon Nanostructures Studied Using the SCC-DFTB Method". He obtained his master degree in 2009, and then served as an orderly in the Medical Affairs Bureau, Ministry of National Defense, Taiwan, for one year to fulfill his obligatory military service. From 2010 to 2012, he joined the Full-Time Training in Taipei, a two-year program of Bible truth and church service training. After graduating from the Training in June of 2012, he resumed his academic career with being a research assistant of Prof. Henryk Witek for six months, focusing on optimizing the density-functional based tight-binding method (DFTB) calculation of vibrational properties of materials. Since March 2013, he conducted his PhD research with Dr. Marijn A. van Huis, in the Soft Condensed Matter group of the Debye Institute for Nanomaterials Science at Utrecht University, the Netherlands. His research in Utrecht has been focused on theoretical modeling of defects in 2D and 3D nanomaterials using density functional theory (DFT).